Goethe-Universität Frankfurt am Main

Fachbereich 13 Physik
Institut für Theoretische Physik
Max-von-Laue Straße 1

MASTER THESIS

Inhomogeneous phases in the $2+1$-dimensional Gross-Neveu model via mean-field lattice field theory

Marc Stefan Winstel

Frankfurt am Main
Submitted on 30-09-2020
Updated on 30-12-2020 with minor linguistic corrections

1st Examiner
Prof. Dr. Marc Wagner
Institut für Theoretische Physik
Goethe Universität Frankfurt am Main

2nd Examiner
Dr. Michael Buballa
Institut für Kernphysik
Technische Universität Darmstadt

Thesis Details

Thesis Title: Inhomogeneous phases in the $2+1$-dimensional Gross-Neveu model via mean-field lattice field theory

Master student: Marc Stefan Winstel

Email: winstel@itp.uni-frankfurt.de

Supervisor: Prof. Dr. Marc Wagner, Goethe Universität Frankfurt am Main

First examiner: Prof. Dr. Marc Wagner, Goethe Universität Frankfurt am Main

Second examiner: Dr. Michael Buballa, Technische Universität Darmstadt

Selbstständigkeitserklärung

Hiermit erkläre ich, dass ich die Arbeit selbstständig und ohne Benutzung anderer als der angegebenen Quellen und Hilfsmittel verfasst habe. Alle Stellen der Arbeit, die wörtlich oder sinngemäß aus Veröffentlichungen oder aus anderen fremden Texten entnommen wurden, sind von mir als solche kenntlich gemacht worden. Ferner erkläre ich, dass die Arbeit nicht - auch nicht auszugsweise - für eine andere Prüfung verwendet wurde.

Frankfurt, den 30.09.2020

Marc Stefan Winstel

Abstract

The focus of this thesis is the investigation of $2+1$-dimensional Gross-Neveu model in the limit of infinite fermion flavors (the large-N_f limit) via mean-field lattice field theory. The phase diagram of this theory, which serves as a model for spontaneous chiral symmetry breaking, is herein studied in the μ-T plane. Of special interest is the existence of an inhomogeneous phase, where the chiral condensate depends on the spatial coordinates. Within this thesis, lattice techniques are applied to investigate the phase diagrams of QCD-inspired models with particular emphasis on the search for inhomogeneous phases. An inhomogeneous phase is obtained at finite lattice spacing. The phase, however, has a strong dependence on the lattice spacing and the used discretization. In the continuum limit the inhomogeneous phase vanishes. Indications for a degenerate ground state at $T \rightarrow 0$, where inhomogeneous modulations of the chiral condensate are energetically equivalent to spatially constant ones, are found at low and intermediate chemical potentials. An extension of the $2+1$-dimensional Gross-Neveu model via introduction of an additional chemical potential μ_I, which couples to a fermionic, isospin-like degree of freedom, is proposed. A shrinking of the inhomogeneous phase, which is present at finite lattice spacing for vanishing μ_I, is observed when increasing this additional chemical potential. It vanishes completely when μ_I exceeds a certain threshold.

Contents

III Results 27

Appendix 60

Part I

Preliminaries

1 Introduction

Elementary particle interactions are governed by three fundamental forces, namely the strong, weak and the electromagnetic force. Their description is unified by the Standard Model of particle physics. The Standard Model has been constructed in the framework of Quantum Field Theory (QFT) by postulating invariance of physical laws under certain transformations, which are mainly inspired by symmetries observed in nature. Hence, these transformations are called symmetry transformations. In contrast to the theory some symmetry might be broken in the observed ground state. This phenomenon, where the Lagrangian of a theory retains a certain symmetry while the ground state breaks it, is called spontaneous symmetry breaking.

1.1 Strongly-interacting matter

The main interest in this thesis is the phenomenology of the strong interaction. Mathematically it is described by the fundamental theory of Quantum Chromodynamics (QCD). Its building blocks are the fermionic quark fields and the gluon fields, which are introduced as gauge bosons to the SU(3) gauge symmetry. The non-abelian gauge group of QCD leads to self-interactions of gluons, which causes the strong interaction to behave significantly different from abelian gauge theories, such as Quantum Electrodynamics. The most prominent features are confinement, i.e. the binding of quarks inside hadrons, and spontaneous chiral symmetry breaking, which is manifested in the generation of a chiral condensate $\langle\bar{\psi}\psi\rangle \neq 0$. Through the chiral condensate, particles acquire a dynamical mass and it is often used as an order parameter for chiral symmetry breaking in phase diagrams. Unfortunately, these interesting phenomena occur at low energies, where the coupling constant of QCD is large and a perturbative treatment is not possible. However, the asymptotic freedom of the theory, i.e. the weak coupling at large energy scales, allows one to understand QCD at very high temperatures T and chemical potentials μ. At large temperatures one finds a weakly-coupled quark-gluon plasma [1], where quarks and gluons are deconfined, while cold and dense matter is expected to form a color-superconductor (for a review see Ref. [2]). At intermediate T and μ, one expects some sort of phase transition from a hadronic and chirally broken phase to occur. At finite temperature and chemical potential, a deconfined, chirally symmetric phase (SP) is expected to occur, although recent investigations have shown no direct one-on-one correspondence between confinement and chiral symmetry breaking [3].

1.2 Phase diagram of QCD-inspired models

In recent years ab-initio lattice QCD calculations have significantly improved the understanding of strongly-interacting matter at finite temperature (see Ref. [4] for a review). However, at finite chemical potential, lattice QCD simulations are plagued by the sign problem (see e.g. Ref. [5]). Consequently, other approaches are needed which are suitable to investigate the behavior of matter in the finite density region of the phase diagram. One possibility is the employment of QFTs that share relevant properties with QCD while being more accessible to analytical and numerical methods. Such QCD-inspired models are expected to reproduce some of its characteristic properties. Prominent examples are the Nambu-Jona-Lasinio (NJL) model [6] and the Gross-Neveu (GN) model [7]. While these models do not describe confinement, they feature a chiral symmetry, which can be spontaneously broken at low chemical potential and temperature.

Investigations of QCD-inspired models indicate that a fourth state of matter might be realized corresponding to regions of phase diagram of strongly-interacting matter at finite chemical potential. The phase diagram could be extended by a so called inhomogeneous phase (IP) with a spatially dependent chiral condensate in the intermediate density region (see Ref. [8] for a review). The $1+1$-dimensional GN model in the limit of infinite fermion flavors, the so-called large-N_f limit, is an example of a rather simple QCD-inspired quantum field theory that features such an IP. In the model the interaction of fermions is described via a scalar four-fermion self-interaction term. The analytical solution [9] features three phases: A phase with constant chiral condensate, the so-called homogeneous broken phase (HBP), a SP and an IP. In the IP, which is found at large baryon chemical potentials and low temperatures, the chiral condensate is oscillating in the spatial coordinate. Directly at the transition point from the HBP the chiral condensate has a kink-antikink shape, at larger μ it changes to a sine-like function. This phase is interpreted as a baryon crystal, since the baryons seem to be localized at the roots of the chiral condensate. The frequency of the oscillation increases when the chemical potential is increased even more, while the oscillation amplitude decreases.

IPs have been found in other QCD-inspired models in the mean-field approximation, which is the neglection of bosonic quantum fluctuations and corresponds to the large-N_f limit for the GN model. These are the NJL model in $3+1$ [10] and $1+1$ dimensions [11] (also called the chiral GN model) and the $1+1$-dimensional isoNJL with multiple chemical potentials [12, 13]. The Quark-Meson model, which is not formulated solely on fermionic fields, has also shown IPs [14, 15].

1.3 $2+1$-dimensional quantum field theories as models for strongly-interacting matter

Although certain aspects of the mentioned models resemble QCD, it is possible to find arguments against their ability to describe the phenomenology of strongly-interacting fermions. $3+1$-dimensional models with four-fermion interactions, e.g. the NJL model, are, in contrast to QCD, not renormalizable. The occurring IP also shows a dependence on the cutoff that is need to normalize the respective model. Other models do not have the same spacetime dimensions as QCD. Additionally, IPs have, until recently, only been found in the mean-field approximation. This issue has been challenged in Refs. [16, 17], where inhomogeneous correlators, which indicate inhomogeneous chiral condensates, have been found in lattice simulations of the GN model in $1+1$ dimensions with finite number of fermion flavors. This study implies that models in the mean-field approximation might contain more information on the full QFTs[1] than expected.

An important concern about the validity of the GN model as a model for strong interaction is its low dimensionality. This aspect will be explicitly focused on in this thesis. Theoretical considerations provide a reason to study theories with four-fermion interaction terms in three spacetime dimensions. Fermion fields have energy dimension 1, so that the coupling of a four-fermion term has dimension -1. Consequently, these theories are perturbatively non-renormalizable, but in contrast to $3+1$-dimensional theories a large-N_f (or large-N_c) expansion allows a renormalization [18]. As a further motivation for such a study, hydrodynamic properties in heavy-ion collision dynamics, which are the main experimental tool to investigate the region at finite chemical potential, are characterized by longitudinal boost invariance [19–21], i.e. the dependence on the $3+1$-dimensional spacetime coordinates is reduced to three independent (Milne-)coordinates [22]. Experimental attention started to shift to the finite μ region, e.g. with the upcoming FAIR facilities in Darmstadt [23]. In such experiments IPs could be observed. Therefore, it is important to improve theoretical predictions on their possible existence in the phase diagram of strongly-interacting matter. Interestingly, three-dimensional QFTs with four-fermion interaction also naturally arise as effective models from tight binding Hamiltonians in condensed matter physics. For example, GN-type models in three spacetime dimensions are used to describe superconducting electrons in high-temperature superconductors which are confined to planes determined by the lattice structure of the material (e.g. CuO_2 planes) [24–26]. However, this thesis focuses on the application to strongly-interacting matter.

In this work the main focus will be on the $2+1$-dimensional GN model in the large-N_f limit as a compromise between physical significance and renormalizability. Lattice field

---

[1] Full QFTs in this case denotes taking full quantum fluctuations into account.

theory techniques, tested with the $1+1$-dimensionsal GN model, are applied to compute the phase diagram with particular focus on the existence of an IP. Techniques are investigated which are able to compute inhomogeneous chiral condensates without making a specific ansatz for the functional form of the chiral condensate. This is a significant advantage compared to other analyses, where the shape of the condensate is restricted to, e.g., a chiral density wave or where the shape of the condensate cannot be computed. It is important to remark that, given the simplicity of the GN model, one cannot expect quantitative predictions for the experiments. Instead our work should be understood as an exploratory investigation into whether IPs will occur in models that are closer to QCD. As an important byproduct, in future studies, the developed lattice techniques can also be applied to models, that are much closer to QCD. In already published results of our work an IP is obtained at finite lattice spacing [27]. However, a recent lattice investigation, that relies on a certain ansatz for the chiral condensate, indicates the vanishing of this IP in the continuum [28]. Lattice results with the $2+1$-dimensional GN model presented in this thesis will soon be published together with a complementary continuum mean-field analyses [29]. In a further study an additional chemical potential, that couples analogously to an isospin chemical potential, is introduced to explore its influence on an IP for the first time.

2 Outline

In Sec. 3 the GN model in $d = D + 1$ dimensions is introduced as a model for spontaneous chiral symmetry breaking of strongly-interacting matter at finite temperature and chemical potential. Basic concepts are established which are needed to study this model in the large-N_f limit. Symmetries and fermion representations in $1+1$ and $2+1$ dimensions are discussed and a chemical potential, that couples similar to an isospin chemical potential, is added to the GN model. Sec. 4 explains the lattice discretization of the GN model needed to compute the phase diagram.

In Part III the results of investigations of the $1+1$-dimensional, $2+1$-dimensional GN model and its extension with an additional "isospin" chemical potential are presented. The analytical solution of the $1+1$-dimensional GN model and the application of lattice field theory techniques in Secs. 6-8 are explained in Sec. 5. In Secs. 6-8 the phase boundary of the models are computed with different methods and restrictions to the chiral condensate to obtain a complete phase diagram.

A brief summary and conclusion of the results is given in Sec. 9. Additionally, an outlook for future investigations based on th findings is given. Appendices A-C contain additional theoretical proofs and discussions, deemed to be not within the scope of Part II.

Part II

Theory

3 The Gross-Neveu model in the limit $N_f \to \infty$

The Gross-Neveu (GN) model is a relativistic QFT describing N_f fermion flavors with a four-fermion self-interaction term. It is arguably the simplest model in the class of QFTs with a four-fermion interaction term, which are often referred to as four-fermion theories. In the literature a large variety of these models can be found, designed for applications in high energy and condensed matter physics. In this work, the GN model will be investigated as a QCD-inspired theory under extreme conditions of high chemical potential μ and temperature T.

Towards the introduction of thermodynamic state variables, such as μ and T, to a QFT, it is pointed out that the interpretation of a quantum partition function Z in $D+1$-dimensional Euclidean spacetime as a statistical system in equilibrium is possible, when the imaginary time direction is restricted to a finite extent $\beta = 1/T$, where T is the temperature of a statistical system. For a derivation Refs. [30, 31] are referred to. As a consequence, bosonic fields, denoted by ϕ, and fermionic fields, denoted by ψ, are restricted to periodic and anti-periodic boundaries in the time direction. Thus, one can identify the quantum partition function with the canonical partition function. A baryon chemical potential μ is introduced in analogy to statistical mechanics and the action is transformed as

$$S[\bar{\psi}, \psi, \phi] \to S[\bar{\psi}, \psi, \phi] - \int \mathrm{d}x_0 \mu B \,, \tag{3.1}$$

where the baryon number operator $B = \int \mathrm{d}^D x \bar{\psi}\gamma_0\psi$ is introduced and Z is interpreted as a grand canonical partition function.

Now,the GN model [7] is considered in $d = D + 1$-dimensional[2] Euclidean spacetime, where the action and partition function are

$$S[\bar{\psi}, \psi] = \int \mathrm{d}^d x \, \bar{\psi}\Big(\gamma_\nu \partial_\nu + \gamma_0 \mu\Big)\psi - \frac{\lambda}{2N_f}\Big(\bar{\psi}\psi\Big)^2 \quad , \quad Z = \int \mathcal{D}\bar{\psi}\, \mathcal{D}\psi \, \mathrm{e}^{-S[\bar{\psi},\psi]} \,. \tag{3.2}$$

---

[2] Only $D = 1, 2$ will be considered.

Here, $\psi = \left(\psi_1, \dots, \psi_{N_f}\right)^{\mathrm{T}}$ represents N_f massless fermion fields[3], λ is the coupling constant and $x = (x_0, \dots, x_{d-1})^{\mathrm{T}}$ is a spacetime coordinate. Possible choices for the γ matrices are discussed in Sec. 3.2. Here, the chemical potential μ is already introduced according to Eq. (3.1). The time direction is implicitly restricted to a finite extent β and the integration over the fields to the (anti-)periodic boundary conditions. Therefore, if the action $S[\bar{\psi}, \psi]$ is real valued, one can always interpret Z as a grand canonical partition function of a statistical system.

3.1 Bosonization and the effective action

To study the dynamical generation of a chiral condensate an auxiliary scalar field σ is introduced and a Hubbard-Stratonovich transformation [32] is performed

$$S_\sigma[\bar{\psi}, \psi, \sigma] = \int \mathrm{d}^d x \left[\bar{\psi}\, \mathrm{Q}\, \psi + \frac{N_f}{2\lambda}\sigma^2\right], \quad Z = \int \mathcal{D}\bar{\psi}\, \mathcal{D}\psi\, \mathcal{D}\sigma\, \mathrm{e}^{-S_\sigma[\bar{\psi},\psi,\sigma]}, \tag{3.3}$$

where

$$\mathrm{Q}[\sigma] = \gamma_\nu \partial_\nu + \gamma_0 \mu + \sigma(x) \tag{3.4}$$

is the Dirac operator.

A relation is sought to connect the bosonic auxiliary field σ to the fermion fields $\bar{\psi}, \psi$ using a Ward identity. The integral over the field values in Eq. (3.3) must be invariant under the transformation

$$\sigma(x) \to \sigma(x) + \delta\sigma(x), \tag{3.5}$$

where $\delta\sigma(x)$ is an infinitesimal shift of the bosonic field. Applying this transformation to Eq. (3.3) results in[4]

$$\begin{aligned} Z' &= \int \mathcal{D}\bar{\psi}\, \mathcal{D}\psi\, \mathcal{D}\sigma\, \exp\left(-\int \mathrm{d}^d x \left[\bar{\psi}\, \mathrm{Q}[\sigma + \delta\sigma]\psi + \frac{N_f}{2\lambda}\left(\sigma + \delta\sigma\right)^2\right]\right) \\ &= \int \mathcal{D}\bar{\psi}\, \mathcal{D}\psi\, \mathcal{D}\sigma\, \mathrm{e}^{-S_\sigma[\bar{\psi},\psi,\sigma]} \exp\left(-\int \mathrm{d}^d x\, \delta\sigma \left[\bar{\psi}\psi + \frac{N_f}{2\lambda}\left(2\sigma + \delta\sigma\right)\right]\right). \end{aligned} \tag{3.6}$$

By expansion of the exponential, one obtains

$$\begin{aligned} Z' &= \int \mathcal{D}\bar{\psi}\, \mathcal{D}\psi\, \mathcal{D}\sigma\, \mathrm{e}^{-S_\sigma[\bar{\psi},\psi,\sigma]} \left[1 - \int \mathrm{d}^d x\, \delta\sigma \left(\bar{\psi}\psi + \frac{N_f}{\lambda}\sigma\right) + O(\delta\sigma^2)\right] \\ Z' &= Z - \int \mathcal{D}\bar{\psi}\, \mathcal{D}\psi\, \mathcal{D}\sigma\, \mathrm{e}^{-S_\sigma[\bar{\psi},\psi,\sigma]} \left[\int \mathrm{d}^d x\, \delta\sigma \left(\bar{\psi}\psi + \frac{N_f}{\lambda}\sigma\right) + O(\delta\sigma^2)\right]. \end{aligned} \tag{3.7}$$

---

[3] As spontaneous chiral symmetry breaking is of interest, only massless fermion fields are considered. Hence, the chiral symmetry is not explicitly broken by construction.

[4] Note that the integral measure is assumed to be invariant under the transformation.

Using the invariance of the partition function under Eq. (3.5) it is found, neglecting second order corrections,

$$0 = \int \mathcal{D}\bar{\psi}\,\mathcal{D}\psi\,\mathcal{D}\sigma\,\mathrm{e}^{-S_\sigma[\bar{\psi},\psi,\sigma]}\left[\int \mathrm{d}^d x\,\delta\sigma\left(\bar{\psi}\psi + \frac{N_f}{\lambda}\sigma\right)\right]. \tag{3.8}$$

One can restrict the arbitrary shift $\delta\sigma(x) = \delta(x-y)\delta\varsigma$, where $\delta\varsigma$ is an infinitesimal number, and obtains the Ward identity

$$\langle\sigma(y)\rangle = -\frac{\lambda}{N_f}\langle\bar{\psi}(y)\psi(y)\rangle. \tag{3.9}$$

Thus, the expectation value of the bosonic field $\langle\sigma\rangle$ is proportional to the fermion condensate $\langle\bar{\psi}\psi\rangle$ and can be interpreted as an order parameter for chiral symmetry breaking. This will be discussed in more detail in Sec. 3.2.

After integrating over the fermion fields in Eq. (3.3) one obtains an effective action, which depends only on the scalar field σ,

$$S_{\text{eff}}[\sigma] = N_f\left(\frac{1}{2\lambda}\int \mathrm{d}^d x\,\sigma^2 - \ln\det(\mathrm{Q})\right), \quad Z = \int \mathcal{D}\sigma\,\mathrm{e}^{-S_{\text{eff}}[\sigma]}. \tag{3.10}$$

As one can see from Eq. (3.10) the action is proportional to the number of fermion flavors N_f. Since this work is in the limit $N_f \to \infty$, only field configurations σ corresponding to global minima of $S_{\text{eff}}[\sigma]$ contribute to the partition function Z. Thus, instead of integration over the scalar field σ in Eq. (3.10) it is sufficient to find the global minima of $S_{\text{eff}}[\sigma]$. Observables are then evaluated on the minimizing field[5] σ', i.e. $\langle\mathrm{O}[\sigma]\rangle = \mathrm{O}[\sigma']$ for any observable O, in particular $\langle\sigma\rangle = \sigma'$.

In this work the dependence of σ is restricted to the spatial coordinates, i.e. $\sigma = \sigma(\mathbf{x})$, where $\mathbf{x} = (x_1, \ldots, x_{d-1})^{\mathrm{T}}$ is a spatial vector. This is motivated by the analytic solution of the $1+1$-dimensional GN model [9], where the chiral condensate only depends on the spatial coordinate. Also the most investigations of IPs are restricted to ansatzes dependent on spatial coordinates. This restriction will also simplify calculations, as is explained in detail in Sec. 4.2.

Since it is $d = 1+1, 2+1$, that is investigated, in Appendix A it is shown that S_{eff} is real in these cases. In $1+1$ dimensions one can perform this proof for an arbitrary chiral condensate $\sigma = \sigma(x_0, x_1)$, while in $2+1$ dimensions the fact that chiral condensate only depends on spatial coordinates is explicitly used, i.e. $\sigma = \sigma(x_1, x_2)$. From this point on,

---

[5] This holds when S_{eff} has a unique global minimum. It can, however, be generalized to multiple equivalent global minima.

the theory is mainly investigated in $d = 2+1$-dimensional spacetime, although the GN model in $1+1$ dimensions will be referred to in some discussions and as a test for the numerical methods of this work.

3.2 Fermion representation and symmetries

In App. A it is shown that the effective action (Eq. (3.10)) has a discrete symmetry

$$\sigma \to -\sigma\,, \tag{3.11}$$

i.e. $S_{\text{eff}}[\sigma] = S_{\text{eff}}[-\sigma]$ (compare Eq. (A.4) and Eq. (A.15)). A non-vanishing σ indicates spontaneous breaking of this symmetry. Moreover, σ is directly proportional to the condensate $\langle\bar{\psi}\psi\rangle$ (see Eq. (3.9)). Hence, the transformation (3.11) must be connected to a symmetry transformation of the fermion fields.

At first, one needs to choose an appropriate fermion representation (Rep.). Note that a suitable set of γ matrices fulfills the Dirac algebra in Euclidean spacetime

$$\{\gamma_\mu, \gamma_\nu\} = \gamma_\mu\gamma_\nu + \gamma_\nu\gamma_\mu = 2\delta_{\mu\nu}\mathbb{1}, \tag{3.12}$$

where $\mathbb{1}$ is the identity in spinor space. After choosing a Rep. (chiral) symmetries will be discussed for $d = 1+1$, $2+1$, respectively. The maximal symmetry group is motivated for free fermions and the symmetries realized in the GN model and the possibility of spontaneous symmetry breaking are discussed. Additionally, important discrete spacetime symmetries and the connection to transformation (3.11) will be explained.

For a discussion of the Poincaré group in $1+1$ and $2+1$ dimensions and its Rep. on a scalar field and with a single fermion flavor see App. B. In this context it is important to note that a chemical potential of $\mu \neq 0$ and having a finite temperature also, breaks Lorentz[6] invariance explicitly.

3.2.1 The Gross-Neveu model in $d = 1+1$ dimensions

A brief discussion of the fermion Rep. typically used for the GN model in $1+1$ spacetime dimensions is first given. In $1+1$ spacetime dimensions a possible irreducible 2×2 Rep. for the γ matrices is

$$\gamma_0 = \tau_1 \quad , \quad \gamma_1 = \tau_2\,, \tag{3.13}$$

where τ_j denote the 2×2 Pauli matrices which satisfy $\tau_i\tau_j = \delta_{ij}\mathbb{1}_2 + \mathrm{i}\epsilon_{ijk}\tau_k$.

---

[6] Although a Euclidean metric is chosen here, the term Lorentz transformation is still used.

Full symmetry for free fermions

A γ_5 matrix is a self-inverse matrix that fulfills $\{\gamma_5, \gamma_\mu\} = 0$. For rep. (3.13) it is appropriate to define $\gamma_5 = \tau_3$.
The free kinetic fermion action is then invariant under vector transformation

$$\psi \to \mathrm{e}^{\mathrm{i}\alpha^a \mathbb{1}_2 \lambda^a}\psi\,, \quad \bar{\psi} \to \bar{\psi}\mathrm{e}^{-\mathrm{i}\alpha^a \mathbb{1}_2 \lambda^a}\,, \tag{3.14}$$

and a continuous chiral symmetry generated by γ_5,

$$\psi \to \mathrm{e}^{\mathrm{i}\theta^a \gamma_5 \lambda^a}\psi\,, \quad \bar{\psi} \to \bar{\psi}\mathrm{e}^{\mathrm{i}\theta^a \gamma_5 \lambda^a}\,, \tag{3.15}$$

where $\{\lambda^1, \dots, \lambda^{N_f - 1}\}$ are the generalized $N_f \times N_f$ Gell-Mann matrices [33] and $\lambda^{N_f} = \mathbb{1}_{N_f}$. α^a and θ^a are the parameters of the transformation. The structure of the generators as tensor products with λ^a is due to flavor rotations. To obtain transformations, that do not act on flavor space, one can set the parameters to $\alpha^a = \delta^{N_f,a}\alpha$ and $\theta^a = \delta^{N_f,a}\theta$. The symmetry group is, consequently, $\mathrm{U}_{\mathbb{1}_2}(N_f) \times \mathrm{U}_{\gamma_5}(N_f)$, where the chiral symmetry can be broken by a mass term.

The Gross-Neveu interaction

The interaction term of the GN model is not invariant under this transformation for arbitrary parameters. For example for $\psi \to \mathrm{e}^{\mathrm{i}\theta\gamma_5}\psi$

$$\left(\bar{\psi}\psi\right)^2 \to \left(\bar{\psi}\mathrm{e}^{2\mathrm{i}\theta\gamma_5}\psi\right)^2 = \left(\bar{\psi}\left[\cos(2\theta)\mathbb{1}_2 + \mathrm{i}\sin(2\theta)\gamma_5\right]\psi\right)^2\,, \tag{3.16}$$

i.e. $\left(\bar{\psi}\psi\right)^2$ is invariant only for $\theta = n\frac{\pi}{2}$, $n \in \mathbb{Z}$. For odd n only a discrete symmetry transformation remains

$$\psi \to \mathrm{i}^n \gamma_5 \psi\,, \quad \bar{\psi} \to \mathrm{i}^n \bar{\psi}\gamma_5\,, \tag{3.17}$$

which, via transformation (3.14), is equivalent to

$$\psi \to \gamma_5 \psi\,, \quad \bar{\psi} \to -\bar{\psi}\gamma_5\,. \tag{3.18}$$

This discrete chiral $\mathbb{Z}_2$-symmetry is the remnant of the continuous chiral symmetry (3.15). Due to Eq. (3.9) a non-vanishing σ implies a non-vanishing fermion condensate $\langle\bar{\psi}\psi\rangle$. This in turn indicates spontaneous breaking of the discrete chiral symmetry, because

$$\langle\bar{\psi}\psi\rangle \overset{(3.18)}{\to} -\langle\bar{\psi}\psi\rangle\,. \tag{3.19}$$

Accordingly, in $1+1$ dimensions σ is an order parameter for spontaneous breaking of the discrete chiral symmetry (3.18).

3.2.2 The Gross-Neveu model in $d = 2+1$ dimensions

At first glance, one might expect that the symmetries in $2+1$ dimensions are the same as in $1+1$ dimensions. However, the situation gets more complicated, since one cannot define a chiral symmetry transformation in the irreducible Rep. of the Dirac algebra (3.12), i.e. for 2-component spin space.

2-component fermion representation

In $2+1$ dimensions there are two inequivalent irreducible Reps. of the Dirac algebra (3.12), which can be written e.g. as

$$\gamma_0 = +\tau_2\,, \quad \gamma_1 = +\tau_3\,, \quad \gamma_2 = +\tau_1\,, \tag{3.20}$$

$$\tilde{\gamma}_0 = -\tau_2\,, \quad \tilde{\gamma}_1 = -\tau_3\,, \quad \tilde{\gamma}_2 = -\tau_1\,. \tag{3.21}$$

Neither for Rep. (3.20) nor Rep. (3.21) there is an appropriate γ_5 matrix. Consequently, there is also no discrete chiral symmetry (3.18) and a non-vanishing σ cannot be interpreted as an indication for chiral symmetry breaking. Indeed, free fermions only have a $\mathrm{U}(N_f)$ symmetry, generated by transformation (3.14). Instead, there is another discrete symmetry

$$(x_0,\, x_1,\, x_2)^{\mathrm{T}} \to (x_0,\, x_1,\, -x_2)^{\mathrm{T}}\,, \quad \psi \to -\mathrm{i}\gamma_2\psi\,, \quad \bar{\psi} \to -\mathrm{i}\bar{\psi}\gamma_2\,, \tag{3.22}$$

changing the sign of $\langle\bar{\psi}\psi\rangle$, i.e.

$$\langle\bar{\psi}\psi\rangle \overset{(3.22)}{\to} -\langle\bar{\psi}\psi\rangle. \tag{3.23}$$

This symmetry is usually defined as P in $2+1$ dimensions, since the reflection of both spatial coordinates is just a rotation with angle π, which is clearly an element of the Euclidean Lorentz group (see App. B.2). Thus, a non-vanishing σ indicates spontaneous breaking of parity.

4-component fermion representation

Since the GN model is used as a very basic model for chiral symmetry breaking in QCD, it is important to consider reducible fermion Reps. with a corresponding γ_5 matrix. One possibility is to combine the irreducible Rep. (3.20) and Rep. (3.21) resulting in 4×4-matrices

$$\gamma_0 = \tau_3 \otimes \tau_2 = \begin{pmatrix} +\tau_2 & 0 \\ 0 & -\tau_2 \end{pmatrix}, \ \gamma_1 = \tau_3 \otimes \tau_3 = \begin{pmatrix} +\tau_3 & 0 \\ 0 & -\tau_3 \end{pmatrix},$$

$$\gamma_2 = \tau_3 \otimes \tau_1 = \begin{pmatrix} +\tau_1 & 0 \\ 0 & -\tau_1 \end{pmatrix} \tag{3.24}$$

(see e.g. Refs. [34–36]). These three matrices are block-diagonal with the upper block corresponding to Rep. (3.20) and the lower block to Rep. (3.21). The introduction of the tensor products with τ_3 can be interpreted as the introduction of an isospin degree of freedom (compare Ref. [37]). That is to say that the two upper components of a spinor describe an "isospin up" spinor, while the two lower components represent "isospin lower" spinor components. There are two linearly independent matrices that anti-commute with the γ_μ matrices[7]

$$\gamma_4 = \tau_1 \otimes \mathbb{1}_2 = \begin{pmatrix} 0 & +\mathbb{1}_2 \\ +\mathbb{1}_2 & 0 \end{pmatrix}, \quad \gamma_5 = -\tau_2 \otimes \mathbb{1}_2 = \begin{pmatrix} 0 & +\mathrm{i}\mathbb{1}_2 \\ -\mathrm{i}\mathbb{1}_2 & 0 \end{pmatrix}, \tag{3.25}$$

i.e. both fulfill the properties necessary for a γ_5 matrix. Chiral transformations are defined by taking both γ_4 and γ_5 into account. Additionally, one can define

$$\gamma_{45} \equiv \mathrm{i}\gamma_4\gamma_5 = \tau_3 \otimes \mathbb{1}_2 = \begin{pmatrix} +\mathbb{1}_2 & 0 \\ 0 & -\mathbb{1}_2 \end{pmatrix}, \tag{3.26}$$

which commutes with the γ matrices but anti-commutes with γ_4 and γ_5. Free massless fermions in $2+1$ dimensions are invariant under the vector transformations

$$\psi \to \mathrm{e}^{\mathrm{i}\alpha^a \mathbb{1}_4 \lambda^a}\psi\,, \quad \bar\psi \to \bar\psi \mathrm{e}^{-\mathrm{i}\alpha^a \mathbb{1}_4 \lambda^a}\,, \tag{3.27a}$$

$$\psi \to \mathrm{e}^{\mathrm{i}\beta^a \gamma_{45} \lambda^a}\psi\,, \quad \bar\psi \to \bar\psi \mathrm{e}^{-\mathrm{i}\beta^a \gamma_{45} \lambda^a}\,, \tag{3.27b}$$

as well as under the axial transformations

$$\psi \to \mathrm{e}^{\mathrm{i}\phi^a \gamma_4 \lambda^a}\psi\,, \quad \bar\psi \to \bar\psi \mathrm{e}^{\mathrm{i}\phi^a \gamma_4 \lambda^a}\,, \tag{3.28a}$$

$$\psi \to \mathrm{e}^{\mathrm{i}\theta^a \gamma_5 \lambda^a}\psi\,, \quad \bar\psi \to \bar\psi \mathrm{e}^{\mathrm{i}\theta^a \gamma_5 \lambda^a}\,, \tag{3.28b}$$

with real parameters $\alpha^a, \beta^a, \phi^a$, θ^a. These four transformations combine to form the symmetry group $\mathrm{U}(2N_f)$. A mass term leads to the symmetry breaking pattern

$$\mathrm{U}(2N_f) \to \mathrm{U}_{\mathbb{1}_4}(N_f) \times \mathrm{U}_{\gamma_{45}}(N_f)\,, \tag{3.29}$$

as the vector transformations (3.27) remain intact.

In the case of the GN model continuous axial transformations (3.28) are reduced to discrete symmetries by the $\left(\bar\psi\psi\right)^2$ interaction term within the same mechanism explained for $1+1$ dimensions. These $\mathbb{Z}_2$-symmetries are

$$\psi \to \gamma_4\psi\,, \quad \bar\psi \to -\bar\psi\gamma_4\,, \tag{3.30a}$$

$$\psi \to \gamma_5\psi\,, \quad \bar\psi \to -\bar\psi\gamma_5\,, \tag{3.30b}$$

---

[7] We keep the notation used in Ref. [35, 36] for the two anti-commuting matrices.

and they are needed to interpreted σ as the chiral order parameter. Note that Eq. (3.30a) and Eq. (3.30b) are not independent. One obtains Eq. (3.30a) by application of vector transformations (3.27b) for $\beta^a = \delta^{N_f,a}\frac{\pi}{2}$ and Eq. (3.30b). Consequently, one independent discrete chiral symmetry transformation is obtained.

To conclude, the Gross-Neveu model with fermion Rep. (3.24) has the vector symmetries (3.27) and discrete chiral $\mathbb{Z}_2$-symmetry. The symmetry breaking pattern is

$$\mathrm{U}_{\mathbb{1}_4}(N_f) \times \mathrm{U}_{\gamma_{45}}(N_f) \times \mathbb{Z}_2 \ \to \mathrm{U}_{\mathbb{1}_4}(N_f) \times \mathrm{U}_{\gamma_{45}}(N_f)\,. \tag{3.31}$$

Spontaneous breaking of the discrete chiral symmetry is indicated by a breaking of symmetry (3.11), i.e. by non-vanishing chiral order parameter σ.

3.3 Equivalence of 2- and 4-component fermion representations

In the following, a simple relation will be derived between the expectation values $\langle O(\sigma)\rangle$ obtained with either of the two irreducible 2-component fermion Reps. (3.20) and (3.21) and the 4-component fermion Rep. (3.24).

Dirac operators for fermion Reps. (3.20), (3.21) and (3.24) are denoted with $\mathrm{Q}^{(2)}$, $\tilde{\mathrm{Q}}^{(2)}$ and $\mathrm{Q}^{(4)}$, respectively. $Q^{(4)}$ has block-diagonal structure in spinor space,

$$\mathrm{Q}^{(4)}[\sigma] = \begin{pmatrix} \mathrm{Q}^{(2)}[\sigma] & 0 \\ 0 & \tilde{\mathrm{Q}}^{(2)}[\sigma] \end{pmatrix}. \tag{3.32}$$

Thus,

$$\det \mathrm{Q}^{(4)}[\sigma] = \det \mathrm{Q}^{(2)}[\sigma] \det \tilde{\mathrm{Q}}^{(2)}[\sigma]\,. \tag{3.33}$$

Using

$$\det \tilde{\mathrm{Q}}^{(2)}[+\sigma] = \det\Big(-\mathrm{Q}^{(2)}[-\sigma]\Big) = \det \mathrm{Q}^{(2)}[-\sigma] = \det \mathrm{Q}^{(2)}[+\sigma]\,, \tag{3.34}$$

where the last step is shown in App. A.2, Eq. (3.33) simplifies to

$$\det \mathrm{Q}^{(4)}[\sigma] = \Big(\det \mathrm{Q}^{(2)}[\sigma]\Big)^2 = \Big(\det \tilde{\mathrm{Q}}^{(2)}[\sigma]\Big)^2. \tag{3.35}$$

From Eq. (3.10) and Eq. (3.35) one can conclude

$$S^{(4)}_{\text{eff}}[\sigma,\lambda] = 2S^{(2)}_{\text{eff}}[\sigma,2\lambda] = 2\tilde{S}^{(2)}_{\text{eff}}[\sigma,2\lambda]\,, \tag{3.36}$$

where $S^{(2)}_{\text{eff}}[\sigma,\lambda]$, $\tilde{S}^{(2)}_{\text{eff}}[\sigma,\lambda]$ and $S^{(4)}_{\text{eff}}[\sigma,\lambda]$ denote the effective actions for fermion Reps. (3.20), (3.21) and (3.24), respectively, and coupling constant λ. Consequently, expectation values $\langle \mathrm{O}[\sigma]\rangle$ are related according to

$$\langle \mathrm{O}[\sigma]\rangle\Big|^{\lambda}_{4\times4\text{ Rep. (3.24)}} = \langle \mathrm{O}[\sigma]\rangle\Big|^{2\lambda}_{2\times2\text{ Rep. (3.20)}} = \langle \mathrm{O}[\sigma]\rangle\Big|^{2\lambda}_{2\times2\text{ Rep. (3.21)}}. \tag{3.37}$$

Note in particular that the phase diagram with respect to the order parameter σ is the same for all three Reps. . In practice this is useful, because all numerical computations can be performed with the computationally cheaper 2×2 fermion Rep. (3.20) (or (3.21)), while the corresponding results are also valid for the 4×4 fermion Rep. (3.24), where an interpretation in terms of chiral symmetry and its spontaneous breaking is possible.

3.4 Isospin asymmetric Gross-Neveu model

As described in Sec. 3.2.2, a reducible, 4×4 fermion Rep. , e.g. given in Eq. (3.24), can be interpreted as the introduction of an isospin index. The action Eq. (3.2), then becomes diagonal in isospin space. Consequently, one can interpret the upper and lower blocks of $\mathrm{Q}^{(4)}$, given in Eq. (3.32), as Dirac operators for fermion fields with "isospin up" and "isospin down". Any 4-component spinor with the two lower components vanishing are defined as a fermion field with "isospin up" and spinors with the two upper components vanishing as a fermion field with "isospin down".

Although the construction of an isospin degree of freedom[8] differs from the usual one in the Standard Model, it is interesting to study how the introduction of an additional chemical potential μ_I us, which couples to an isospin degree of freedom, affects the phase diagram of a theory and, especially, the existence of IPs. μ_I is introduced with an additional coupling in this space via a γ_{45} matrix.

The resulting action is given by (compare Eq. (3.2))

$$S[\bar{\psi}, \psi] = \int \mathrm{d}^3x \left(\bar{\psi}\Big(\gamma_\nu \partial_\nu + \gamma_0 \mu + \gamma_{45}\gamma_0\mu_I\Big)\psi - \frac{\lambda}{2N_f}\Big(\bar{\psi}\psi\Big)^2 \right), \; Z = \int \mathcal{D}\bar{\psi}\,\mathcal{D}\psi\, \mathrm{e}^{-S[\bar{\psi},\psi]}, \tag{3.38}$$

where Rep. (3.24) is used, in this case, for the Gamma matrices. Then, the GN model with "isospin" chemical potential can be treated in the same way as in Sec. 3.1. In the effective action a Dirac operator with the additional isospin structure is obtained, i.e.

$$S_{\text{eff}}[\sigma] = N_f\left(\frac{1}{2\lambda}\int \mathrm{d}^3x\, \sigma^2 - \ln \mathrm{Det}(\mathrm{Q})\right), \quad Z = \int \mathcal{D}\sigma\, \mathrm{e}^{-S_{\text{eff}}[\sigma]} \tag{3.39}$$

with

$$\mathrm{Q}^{(4)} = \gamma_\nu\partial_\nu + \gamma_0\mu + \gamma_{45}\gamma_0\mu_I + \sigma\,. \tag{3.40}$$

One can show that

$$\det \mathrm{Q}^{(4)}[\mu, \mu_I, +\sigma] = \det \mathrm{Q}^{(4)}[\mu, \mu_I, -\sigma]\,, \tag{3.41}$$

---

[8] For a discussion of this interpretation see Sec. 5 and App. A of Ref. [37]. It should be noted that what is herein defined as isospin differs from in the Standard Model, as the underlying symmetries are only discrete symmetries in the $2+1$-dimensional GN model

as is done for $\mu_I = 0$ in App. A.2. In an analogous way one can calculate

$$\det \mathrm{Q}^{(4)}[-\mu, -\mu_I, \sigma] = \det \mathrm{Q}^{(4)}[+\mu, +\mu_I, \sigma] \,. \tag{3.42}$$

The Dirac operator can be expressed via irreducible blocks in isospin space

$$\mathrm{Q}^{(4)}[\mu, \mu_I, \sigma] = \begin{pmatrix} \mathrm{Q}^{(2)}[\mu + \mu_I, \sigma] & 0 \\ 0 & \tilde{\mathrm{Q}}^{(2)}[\mu - \mu_I, \sigma] \end{pmatrix} , \tag{3.43}$$

where $\mathrm{Q}^2[\mu, \sigma]$ and $\tilde{\mathrm{Q}}^{(2)}[\mu, \sigma]$ are defined as in Sec. 3.3. For $Q^{(2)}$ and $\tilde{\mathrm{Q}}^{(2)}$ the following identities hold

$$\det \mathrm{Q}^{(2)}[\mu, +\sigma] = \det \mathrm{Q}^{(2)}[\mu, -\sigma] \tag{3.44}$$

and

$$\det \mathrm{Q}^{(2)}[+\mu, \sigma] = \det \mathrm{Q}^{(2)}[-\mu, \sigma] \,. \tag{3.45}$$

Consequently, for $\mu_I = 0$, again, the identity from Sec. 3.3,

$$\det \mathrm{Q}^{(4)}[\mu, \sigma] = \Big(\det \mathrm{Q}^{(2)}[\mu, \sigma]\Big)^2 = \Big(\det \tilde{\mathrm{Q}}^{(2)}[\mu, \sigma]\Big)^2 , \tag{3.46}$$

is found. The same holds for $\mu = 0$ with the identification $\mu_I \equiv \mu$, which can be shown using Eq. (3.45). Consequently, the identities (3.36) and (3.37) also hold for μ_I. In the case of $\mu \neq 0$ and $\mu_I \neq 0$ one obtains

$$\det \mathrm{Q}^{(4)}[\mu, \mu_I, \sigma] = \det \mathrm{Q}^{(2)}[\mu + \mu_I, \sigma] \det \tilde{\mathrm{Q}}^{(2)}[\mu - \mu_I, \sigma] \,, \tag{3.47}$$

which cannot be identified with the typical GN model in 2+1 dimensions. For the upper block in Eq. (3.43), i.e. for "isospin up" fields, one has a chemical potential $\mu + \mu_I$ and for "isospin down" fields one has a chemical potential $\mu - \mu_I$. The application of the discrete chiral symmetry transformation (3.30) leads to

$$\begin{aligned} \det \mathrm{Q}^{(4)}[\mu, \mu_I, \sigma] \to \det \mathrm{Q}^{(4)\prime}[\mu, \mu_I, \sigma] &= \det \mathrm{Q}^{(2)}[\mu - \mu_I, -\sigma] \det \tilde{\mathrm{Q}}^{(2)}[\mu + \mu_I, -\sigma] \\ &= \det \mathrm{Q}^{(2)}[\mu - \mu_I, \sigma] \det \tilde{\mathrm{Q}}^{(2)}[\mu + \mu_I, \sigma] \\ &= \det \tilde{Q}^{(2)}[\mu - \mu_I, \sigma] \det \mathrm{Q}^{(2)}[\mu + \mu_I, \sigma] \,, \end{aligned} \tag{3.48}$$

where in the second line Eq. (3.44) is used and in the last step Eq. (3.34) is used. Consequently, the discrete chiral symmetry transformations leads to an exchange of the chemical potentials for "isospin up" and "isospin down" fermions. As obtained in this calculation, the action is still invariant under this exchange of chemical potentials. Through relation Eq. (3.45) one can easily see that the determinant of the Diracoperator $\det \mathrm{Q}^{(4)}$ is invariant under the exchange of the two chemical potentials

$$\mu_I \to \mu \,, \; \mu \to \mu_I \,. \tag{3.49}$$

In the following discussions $\mu_I = 0$ is set, unless denoted otherwise. This preserves generality in dimensionality and spin space in the following chapter. However, the lattice discretization discussed in Sec. 4 can be applied to $\mu_I \neq 0$ analogously.

4 Lattice discretization

We consider a D-dimensional spatial volume V of extent L, i.e. $V = L^D$, with periodic boundary conditions. As in Sec. 3 we later set $D = 1, 2$. The volume is discretized using lattice field theory, where the lattice spacing is denoted by a and the number of lattice sites is N_s^D, i.e. N_s lattice sites in each of the D directions and $L = N_s a$. Formally, we define the lattice in the spatial directions as a set of discrete spacetime points $\mathbf{x} = \mathbf{n}a$ with $\mathbf{n} = (n_1, \ldots, n_D)^{\mathrm{T}}$, where integer numbers $n_j = 0, \ldots, N_s - 1$. Unless explicitly stated otherwise, all spatial coordinates in this chapter are restricted to the lattice sites.

Since we are interested in studying spontaneous chiral symmetry breaking, it is essential to use a chirally symmetric fermion discretization. We decided to use the naive discretization (see e.g. the textbook [38]). Naive fermions imply fermion doubling, i.e. in the case of D spatial dimensions the number of fermion flavors N_f is restricted to multiples of 2^D. This is not a problem, because we focus on the limit $N_f \to \infty$. For a discussion on the implications of the naive lattice discretization of fermion fields in the context of free fermions and the GN model we refer to App. C.

The temporal extent corresponds to the inverse temperature $\beta = 1/T$ and boundary conditions are antiperiodic. In the temporal direction we do not use lattice field theory, but regularize the fermion fields by a superposition of $2N_t$ plane waves, as discussed in detail below and in Refs. [39, 40]. The chemical potential can be introduced as in the continuum by adding $\gamma_0 \mu$ to the Dirac operator, i.e. an exponential coupling as typically used in lattice field theory is not necessary. As a consequence we expect smaller discretization errors (see Ref. [41] for a detailed discussion). Ref. [41] states that in principle one needs to add a corrective term to fermionic observables, when introducing μ as in the continuum. Since we are interested in the chiral condensate, we do not need such a correction. The application of plane waves to the GN model allow straightforward analytical simplifications of the fermion determinant[9], if the chiral condensate does not depend on x_0, i.e. $\sigma = \sigma(\mathbf{x})$ with $\mathbf{x} = (x_1, \ldots, x_D)^{\mathrm{T}}$.

4.1 Free fermions

We define the plane wave expansion of a fermion field representing a single flavor as

$$\psi(x_0, \mathbf{x}) = \sum_{n_0=-N_t+1}^{N_t} \frac{1}{\sqrt{2N_t}} \psi(n_0, \mathbf{x})\, \mathrm{e}^{\mathrm{i}\omega_{n_0} x_0}\,, \tag{4.1}$$

where $2N_t$ denotes the number of modes. The frequencies $\omega_{n_0} = 2\pi(n_0 - 1/2)/\beta$ with $n_0 = -N_t + 1, -N_t + 2, \ldots, N_t - 1, N_t$ imply antiperiodic boundary conditions in tem-

---

[9] This is also the case for the usual lattice discretization of fermions, as e.g. for the naive discretization.

poral direction. We use $1/a \equiv 1$ as density of degrees of freedom[10], i.e. $2N_t/\beta = 1$. Consequently, the inverse temperature and the number of modes are related according to $\beta = 2N_t$. Inserting the plane wave expansion in the free fermion action leads to[11]

$$\begin{aligned} S_{\text{free}}[\bar{\psi}, \psi] &= \int d^3x\, \bar{\psi}(x_0, \mathbf{x}) \Big(\gamma_0(\partial_0 + \mu) + \sum_{\nu=1}^{D} \gamma_\nu \partial_\nu \Big) \psi(x_0, \mathbf{x}) = \\ &= \sum_{n_0=-N_t+1}^{N_t} \int d^2x\, \bar{\psi}(n_0, \mathbf{x}) \Big((\gamma_0(\mathrm{i}\omega_{n_0} + \mu) + \sum_{\nu=1}^{D} \gamma_\nu \partial_\nu \Big) \psi(n_0, \mathbf{x}) \,. \end{aligned} \tag{4.2}$$

For the spatial directions we apply the naive lattice discretization,

$$\begin{aligned} S_{\text{free}}[\bar{\chi}, \chi] = \sum_{n_0=-N_t+1}^{N_t} \sum_{\mathbf{x}} \bar{\chi}(n_0, \mathbf{x}) \Bigg(& \gamma_0(\mathrm{i}\omega_{n_0} + \mu)\chi(n_0, \mathbf{x}) \\ & + \sum_{j=1}^{D} \gamma_j \frac{\chi(n_0, \mathbf{x} + \mathbf{e}_j) - \chi(n_0, \mathbf{x} - \mathbf{e}_j)}{2} \Bigg) \,. \end{aligned} \tag{4.3}$$

Due to fermion doubling χ represents 2^D fermion flavors and, thus, cannot be interpreted as a standard fermion field ψ as e.g. used in Eq. (4.2) or in Sec. 3. The relation between the components of χ and of ψ is non-trivial. In Refs. [16, 17, 42] this is discussed in detail. We give a short summary in App. C.

4.2 The Gross-Neveu model

A possible naive lattice discretization of the effective action (3.3) of the GN model with N_f flavors is

$$\begin{aligned} S_\sigma[\bar{\chi}_f, \chi_f, \sigma] = \sum_{f=1}^{N_f/2^D} \Bigg(& S_{\text{free}}[\bar{\chi}_f, \chi_f] + \sum_{n_0=-N_t+1}^{N_t} \sum_{\mathbf{x},\mathbf{y}} \bar{\chi}_f(n_0, \mathbf{x}) W_D(\mathbf{x} - \mathbf{y}) \sigma(\mathbf{y}) \chi_f(n_0, \mathbf{x}) \Bigg) \\ & + \frac{N_f N_t}{\lambda} \sum_{\mathbf{x}} \sigma^2(\mathbf{x}) \,, \end{aligned} \tag{4.4}$$

where we substitute W_D with

$$W'_D(\mathbf{x} - \mathbf{y}) = \prod_{j=1}^{D} \left(\frac{1}{4} \delta_{x_j - 1, y_j} + \frac{1}{2} \delta_{x_j, y_j} + \frac{1}{4} \delta_{x_j + 1, y_j} \right) \tag{4.5}$$

---

[10] Throughout this section we express all dimensionful quantities in units of the lattice spacing, e.g. $L \equiv L/a$, $\mu \equiv \mu a$ or $\sigma \equiv \sigma a$.

[11] Note that the representation of γ matrices and spinors depends on the spacetime dimensionality $d = D + 1$.

and

$$W''_D(\mathbf{x}-\mathbf{y}) = \prod_{j=1}^{D} \frac{1}{N_s}\left[1 + \sum_{n=1}^{\frac{N_s}{4}-1} 2\cos\left(\frac{2\pi n(x_j - y_j)}{L}\right) + \cos\left(\frac{\pi}{2}(x_j - y_j)\right)\right] . \tag{4.6}$$

Because of fermion doubling $N_f/2^D$ naive fermion fields χ_f, $f = 1, \ldots, N_f/2^D$ are needed to represent N_f fermion flavors. We stress that a specific non-diagonal structure of $W_D(\mathbf{x}-\mathbf{y})$ is mandatory for a valid discretization of the GN model with naive fermions, i.e. a discretization with the correct continuum limit. The straightforward and probably more intuitive choice $W_D(\mathbf{x}-\mathbf{y}) = \delta_{\mathbf{x},\mathbf{y}}$, which we used at an early stage of this work [27] and which was also used in Ref. [28], introduces additional four fermion interactions, which are not part of the GN model. For a detailed discussion in the context of the 1+1-dimensional GN model we refer to App. A of Ref. [16]. We motivate the introduction of a non-diagonal W_D for the naive discretization of fermions and derive W'_D and W''_D for $D = 1$ in App. C. As we explain in detail there, the chosen weight functions are contrary choices in the way to suppress the wrong interaction terms. While W''_D is more costly compared to W'_D as one needs to sum over the whole lattice, it exactly suppresses the wrong interaction terms. W'_D in contrast relatively crudely suppresses the wrong interaction terms for large lattice spacing albeit resulting in the correct continuum theory (compare Fig. C.1 in App. C). Note that the number of lattice sites N_s is restricted to multiples of 4 when using W''_D to ensure correct normalization.

After integrating over the fermion fields in the partition function, as discussed in Sec. 3, one obtains the discretized effective action

$$S_{\text{eff}}[\sigma] = N_f\left(\frac{N_t}{\lambda}\sum_{\mathbf{x}}\sigma^2(\mathbf{x}) - \frac{1}{2^D}\ln\det(\mathrm{Q})\right) . \tag{4.7}$$

The Dirac operator Q is a matrix of size $2N_tN_s^DN_\gamma \times 2N_tN_s^DN_\gamma$ with rows and columns representing spacetime and spin[12],

$$\begin{aligned} \mathrm{Q}(n_0,\mathbf{x};n'_0,\mathbf{x}') =& \delta_{n_0,n'_0}\Bigg(\gamma_0(\mathrm{i}\omega_{n_0}+\mu)\delta_{\mathbf{x},\mathbf{x}'} + \sum_{j=1}^{D}\gamma_\nu\frac{\delta_{\mathbf{x}+\mathbf{e}_j,\mathbf{x}'} - \delta_{\mathbf{x}-\mathbf{e}_j,\mathbf{x}'}}{2} \\ &+ \delta_{\mathbf{x},\mathbf{x}'}\sum_{\mathbf{y}}W_D(\mathbf{x}-\mathbf{y})\sigma(\mathbf{y})\Bigg) . \end{aligned} \tag{4.8}$$

This matrix is block-diagonal with respect to the temporal indices n_0 and n'_0. Thus, one

---

[12] N_γ denotes the dimensionality of spin space. Due to our restriction to $D = 1, 2$ either $N_\gamma = 2$ or $N_\gamma = 4$ in this thesis.

can factorize the fermion determinant in (4.7),

$$\ln\det(\mathrm{Q}) = \sum_{n_0=-N_t+1}^{N_t} \ln\det\Big(\mathrm{Q}(n_0,\mathbf{x};n_0,\mathbf{x}')\Big)\,, \tag{4.9}$$

i.e. the problem is reduced to the computation of the determinants of $2N_t$ smaller matrices of size $N_\gamma N_s^D \times N_\gamma N_s^D$.

4.3 Numerical evaluation of the effective action

We perform computations in $1+1$ dimensions with the 2×2 γ matrices (3.13). In $2+1$ dimensions most calculations are performed for the irreducible, 2×2 Rep. (3.20), but some are also cross-checked for 4×4 γ matrices (3.24) (see the detailed discussion in Sec. 3.3). For $\mu_I \neq 0$ Rep. (3.24) is used. An important part of these computations is the numerical evaluation of the effective action (4.7) for a given field configuration σ. Typically this has to be repeated many times, e.g. when minimizing S_{eff} with respect to σ or when checking the stability of a homogeneous condensate σ with respect to infinitesimal inhomogeneous deformations. Particularly time consuming is the computation of $\ln\det(\mathrm{Q})$. To maximize efficiency, we distinguish the following three cases:

- $\sigma = \sigma(x_1,x_2)$:[13]
  The Dirac operator (4.8) is a block-diagonal matrix with $2N_t$ blocks of size $N_\gamma N_s^2 \times N_\gamma N_s^2$. The determinant of each block is computed via a standard LU-decomposition (we use the publicly available GSL library [43]).

- $\sigma = \sigma(x_1)$:
  Restricting the dependence of σ to only one of the D spatial coordinates, i.e. $\sigma = \sigma(x_1)$, further reduces the numerical costs of computing S_{eff}. As we will explain in Sec. 7, this case will be interesting for $D = 2$. Similar to the plane wave expansion in temporal direction, one can diagonalize the Dirac operator (4.8) with respect to $\vec{x} = (x_2,\ldots,x_D)^{\mathrm{T}}$ by the ansatz

$$\chi(x_0,\mathbf{x}) = \sum_{n_0=-N_t+1}^{N_t} \sum_{n_2,\ldots,n_D=0}^{N_s-1} \frac{1}{\sqrt{2N_tN_s}}\chi(n_0,x_1,\vec{n})\,\mathrm{e}^{\mathrm{i}(\omega_{n_0}x_0+\vec{k}\vec{x})} \tag{4.10}$$

  with $\vec{x}$ still restricted to the sites of the spatial lattice[14]. We define $\vec{k} = (k_{n_2},\ldots,k_{n_D})^{\mathrm{T}} = 2\pi\vec{n}/L$ with $\vec{n} = (n_2,\ldots,n_D)^{\mathrm{T}}$ and integer numbers $n_j = 0,\ldots,N_s-1$. The Dirac

---

[13] Of course, this case is only considered for $D \geq 2$.

[14] In principle the $\vec{x}$ direction could be treated in the continuum, exactly in the same way as the temporal direction discussed in section 4.1. However, since we plan to compare to computations with $\sigma = \sigma(x_1,\ldots,x_D)$, we prefer to use the same regularization in both cases, i.e. use a lattice discretization of the $\vec{x}$ direction also for $\sigma = \sigma(x_1)$.

operator (4.8) then becomes

$$\begin{aligned}
&\mathrm{Q}(n_0,x_1,\vec{n};n_0',x_1',\vec{n}') = \\
&\quad = \delta_{n_0,n_0'}\delta_{\vec{n},\vec{n}'}\Bigg(\gamma_0(\mathrm{i}\omega_{n_0}+\mu)\delta_{x_1,x_1'} + \gamma_1\frac{\delta_{x_1+1,x_1'}-\delta_{x_1-1,x_1'}}{2} \\
&\qquad + \sum_{\nu=2}^{D}\delta_{x_1,x_1'}\gamma_\nu \mathrm{i}\sin(k_{n_\nu}) + \delta_{x_1,x_1'}\sum_{y_1}W_1(x_1-y_1)\sigma(y_1)\Bigg)
\end{aligned} \tag{4.11}$$

where we define W_1 as

$$W_1'(x_1-y_1) = \frac{1}{4}\delta_{x_1-1,y_1} + \frac{1}{2}\delta_{x_1,y_1} + \frac{1}{4}\delta_{x_1+1,y_1} \tag{4.12}$$

or

$$W_1''(x_1-y_1) = \frac{1}{N_s}\left[1+\sum_{n=1}^{\frac{N_s}{4}-1}2\cos\left(\frac{2\pi n(x_1-y_1)}{L}\right)+\cos\left(\frac{\pi}{2}(x_1-y_1)\right)\right]. \tag{4.13}$$

This is a block-diagonal matrix with respect to the temporal indices n_0 and n_0' as well as the spatial indices $\vec{n}$ and $\vec{n}'$. The computation of the fermion determinant in (4.7) is thus reduced to the computation of the determinants of $2N_tN_s^{D-1}$ matrices of size $N_\gamma N_s \times N_\gamma N_s$,

$$\ln\det(\mathrm{Q}) = \sum_{n_0=-N_t+1}^{N_t}\sum_{n_2,\ldots,n_D=0}^{N_s-1}\ln\det\Big(\mathrm{Q}(n_0,x_1,\vec{n};n_0,x_1',\vec{n})\Big). \tag{4.14}$$

Again, the determinant of each block is computed via a standard LU-decomposition.

- $\sigma = \text{const}$:
  The eigenvalues of Q can be calculated analytically in a straightforward way.Due to the restriction on homogeneous σ the result is independent of the choice on the W_D function. We show the result for the $D+1$-dimensional GN model. We only consider $D \in \{1,2\}$ and, thus, are able to use 2×2 γ matrices according to the discussion in Sec. 3.3. $\ln\det(\mathrm{Q})$ is then computed by summing over the eigenvalues[15],

$$\frac{S_{\text{eff}}[\sigma]}{N_f} = \frac{N_tN_s^D}{\lambda}\sigma^2 - \frac{1}{4}\sum_{n_0=1}^{N_t}\sum_{\mathbf{n}}\ln\left(A_D^2(\sigma)+B^2\right), \tag{4.15}$$

---

[15] Note that in contrast to previous equations in this section the sum over n_0 is restricted to positive integers.

where $\mathbf{n} = (n_1, \ldots, n_D)^{\mathrm{T}}$ with $n_j = 0, \ldots, N_s - 1$ and

$$A_D(\sigma) = \sigma^2 - \mu^2 + \omega_{n_0}^2 + \sum_{j=1}^{D} \sin^2(k_{n_j}) \,, \quad B = 2\mu\omega_{n_0} \,, \tag{4.16}$$

$\omega_{n_0} = 2\pi(n_0 - 1/2)/\beta$ and $k_{n_j} = 2\pi n_j / L$. We will also need the second derivative of $S_{\text{eff}}[\sigma]$ at $\sigma = 0$, which can be expressed as

$$\frac{\partial^2}{\partial\sigma^2} \frac{S_{\text{eff}}[\sigma]}{N_f}\bigg|_{\sigma=0} = \frac{2N_t N_s^D}{\lambda} - \sum_{n_0=1}^{N_t} \sum_{\mathbf{n}} \frac{A_D(0)}{A_D^2(0) + B^2} \,. \tag{4.17}$$

and the fourth derivative of $S_{\text{eff}}[\sigma]$ at $\sigma = 0$, i.e.

$$\frac{\partial^4}{\partial\sigma^4} \frac{S_{\text{eff}}[\sigma]}{N_f}\bigg|_{\sigma=0} = \sum_{n_0=1}^{N_t} \sum_{\mathbf{n}} \left(\frac{12 A_D^2(0)}{(A_D^2(0) + B^2)^2} - \frac{6}{A_D^2(0) + B^2} \right) . \tag{4.18}$$

4.4 Scale setting

The scale setting for the $1+1$-dimensional and $2+1$-dimensional GN model works similar. Our method to set the scale is based on results from Ref. [37, 44–46], where it was found that at $\mu = 0$ there is a homogeneously broken phase with $\sigma \neq 0$ for $T < T_c$ and a symmetric phase with $\sigma = 0$ for $T > T_c$ (T_c denotes the critical temperature). Moreover, the corresponding phase transition turned out to be of second order, as it is for the $1+1$-dimensional GN model [9, 44].

In our regularization the number of modes in temporal direction is proportional to the inverse temperature,

$$N_t = \frac{\beta}{2} \equiv \frac{\beta}{2a} \,, \tag{4.19}$$

as discussed in the beginning of Sec. 4. Moreover, the lattice spacing is a function of the coupling constant λ, where $a(\lambda)$ is monotonically increasing. Thus, the temperature can be adjusted by either changing N_t or λ. To set the scale, we fix the number of modes at the critical temperature to $N_{t,c}$, where $N_{t,c}$ is typically a small number, $2 \leq N_{t,c} \leq 10$ (throughout this section $N_s = L$ is chosen sufficiently large, such that finite volume corrections are negligible). This in turn fixes the coupling constant λ, which has to be tuned in such a way that $2N_{t,c}a(\lambda)$ corresponds to β_c (according to (4.19)). An obvious possibility is to determine λ such that $\sigma(\lambda - \epsilon) = 0$ and $\sigma(\lambda + \epsilon) \neq 0$ for infinitesimal ϵ (see Fig. 4.1). Mathematically equivalent (because the phase transition is of second order), but more practical from a numerical point of view is to consider $(\partial^2/\partial\sigma^2) S_{\text{eff}}[\sigma]/N_f|_{\sigma=0}$

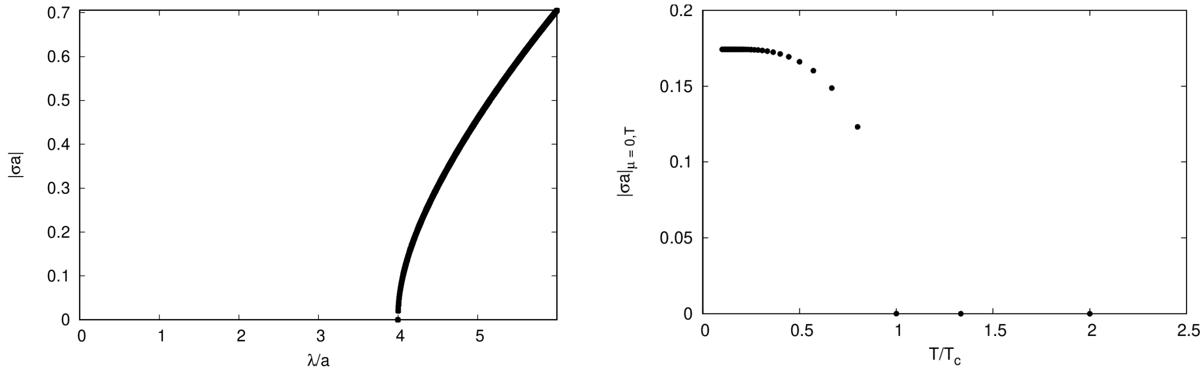

Fig. 4.1: Both plots are from calculations for $D = 2$. For $D = 1$ the results are qualitatively the same. **(left)** $|\sigma|$ as a function of λ for $N_t = 5$ and $N_s = 100$. $N_{t,c} = 5$ corresponds to $\lambda = 3.998$, i.e. that value of λ, where $|\sigma|$ starts to deviate from 0. The plot also confirms that the transition between the homogeneously broken phase and the symmetric phase at $\mu = 0$ is of second order. **(right)** $|\sigma|_{\mu=0,T}$ as a function of T/T_c for $N_{t,c} = 4$ and $N_s = 80$.

(see (4.17)) as a function of λ and to determine its root, which leads to

$$\lambda = 2N_{t,c}N_s^2\left(\sum_{n_0=1}^{N_{t,c}}\sum_{\mathbf{n}}\frac{A_D(0)}{A_D^2(0)+B^2}\right)^{-1}. \tag{4.20}$$

Even though λ is now fixed, the temperature can still be changed in discrete steps by increasing or decreasing the number of modes, $T = 1/2N_t$.

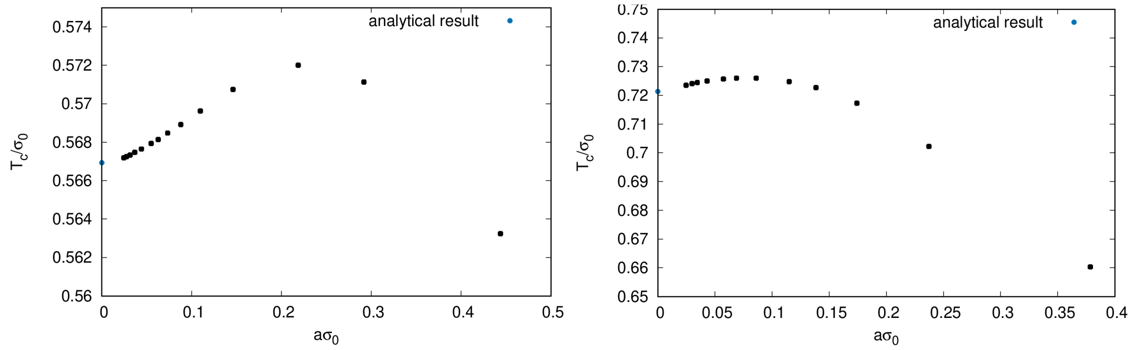

Fig. 4.2: T_c/σ_0 as a function of the lattice spacing a. **(left)** $D = 1$. The data points correspond to $N_{t,c} \in [2, 36]$. For small values of a, T_c/σ_0 approaches the analytical result $e^C/\pi \approx 0.566\ldots$ **(right)** $D = 2$. The data points correspond to $N_{t,c} \in [2, 28]$. For small values of a, T_c/σ_0 approaches the analytical result $1/2\ln(2) \approx 0.721\ldots$

To obtain $|\sigma|_{\mu,T}$, one has to minimize S_{eff} with respect to σ. In μ-T regions, where a homogeneous condensate is expected, e.g. at $\mu = 0$, this is numerically rather simple.

One just has to minimize S_{eff} as given in Eq. (4.15), which is an ordinary function of a single variable, using e.g. a standard golden section search. $|\sigma|_{\mu=0,T}$ quickly approaches a plateau, when decreasing T, i.e. $|\sigma|_{\mu=0,T}$ is almost constant for $T \lesssim T_c/4$ (see Fig. 4.1, right plot). This allows to determine $\sigma_0 = |\sigma|_{\mu=0,T=0} \approx |\sigma|_{\mu=0,T \lesssim T_c/4}$ and to express all dimensionful quantities in units of σ_0, which is common throughout the literature.

For the critical temperature T_c/σ_0 we obtain values rather close to the analytically known result in the continuum, i.e. $1/2\ln(2)$ in the $2+1$-dimensional GN model[45] and e^C/π in the $1+1$-dimensional GN model[9], where C is the Euler-Mascheroni constant. When increasing $N_{t,c}$ (and, thus, decreasing λ), which amounts to approaching the continuum limit, our results for T_c/σ_0 approach $1/2\ln(2) \approx 0.721$ and $e^C/\pi \approx 0.566$, as can be seen in Fig. 4.2.

Part III

Results

5 Preliminary remarks on the results

This section describes the lattice setups used and the structure applied in the following Secs. 6, 7 and 8. In each of these sections the methods employed to detect phase boundaries will be discussed first. It is important to remark that not all the methods used allow one to determine a complete phase diagram, they rather focus on some of its aspects. Nevertheless, the term "phase diagram" is still used and it will accordingly have a different interpretation, depending on the respective section. To validate the numerical methods of this thesis, they are tested on the analytical results of the $d = 1 + 1$-dimensional GN model in the large-N_f limit at the beginning of each section. Thereby, the analytical results are discussed in the following. Then, expectations for $2 + 1$-dimensional models are briefly formulated based on previous studies. Finally, the lattice data are collected in Tab. 1.

5.1 Analytical solution of the $1 + 1$-dimensional Gross-Neveu model in the large-N_f limit

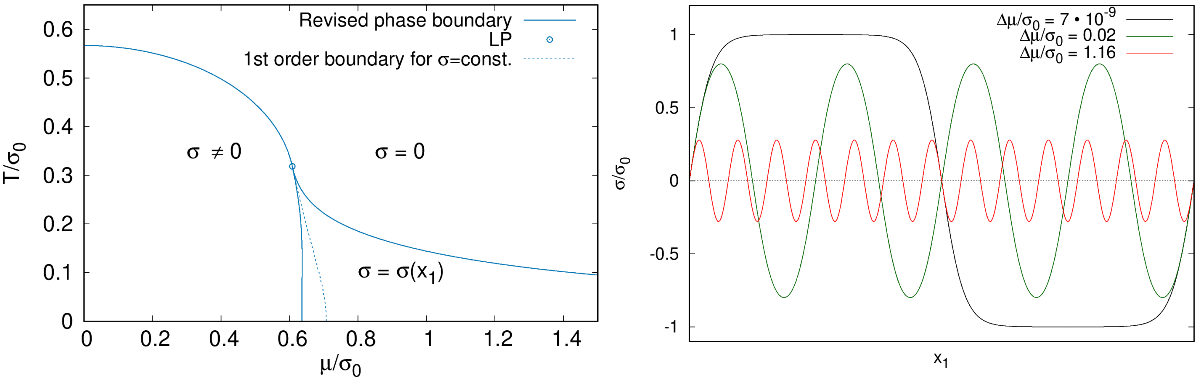

Fig. 5.1: (left) The revised phase diagram of the $1 + 1$-dimensional GN model in the large-N_f limit [9]. The dashed blue line represents the first order phase transition from the SP and the HBP for homogeneous chiral condensate σ = const. from Ref. [47]. All other boundaries are of second order. **(right)** The chiral condensate σ' in the IP for various $\mu/\sigma_0 = (\mu_c + \Delta\mu)/\sigma_0$, at $T = 0$, where μ_c is the chemical potential, at which the phase transition from the IP to the HBP occurs.

In this subsection the analytical solution for the $d = 1 + 1$-dimensional GN model is presented. Analytical results are shown for both the homogeneous chiral condensate [47] and the revised phase diagram [9] with inhomogeneous solutions in the left panel of Fig. 5.1. The analytical solution in Ref. [9] features three phases characterized by different behaviors of $\sigma = \sigma'$:[16]

- A symmetric phase (SP) with $\sigma = 0$ at large μ and/or large T.
- A homogeneous broken phase (HBP) with $\sigma =$ const. and $\sigma \neq 0$ at small μ and small T.
- An inhomogeneous phase (IP), where $\sigma(\mathbf{x})$ is a varying function of the spatial coordinates (compare to the right panel of Fig. 5.1), at intermediate μ and small T. Exactly at the phase transition one obtains a kink-antikink shape. With increasing μ the chiral condensate changes to a cos-like shape. The frequency of the oscillation increases with a further increase of the chemical potential, while the amplitude decreases. This functional behavior of the chiral condensate is analytically described by a product of Jacobi elliptic functions.

For a homogeneous condensate $\sigma =$ const. one obtains a first order transition from $T/\sigma_0 = 0.0$, $\mu/\sigma_0 = 1/\sqrt{2} \approx 0.707$ to the Tricritical point (TCP) at $T/\sigma_0 = 0.318$, $\mu/\sigma_0 = 0608$, where the homogeneous phase transition changes from first to second order. The Tricritical point (TCP) is located at the Lifshitz point (LP), which occurs for an inhomogeneous $\sigma = \sigma(x_1)$ and describes the point, where both phase boundaries from the IP meet the phase transition between the homogeneous phases. Above the LP the second order boundary between the HBP and the SP does not change compared to the homogeneous case. Below the LP both second order phase transitions towards the IP split up and the IP completely covers the first order line from the homogeneous phase diagram. The boundary between the HBP and the IP extends to $T/\sigma_0 = 0.0$, $\mu/\sigma_0 = 2/\pi \approx 0.637$.

5.2 Classification of phase boundaries and previous results

Strictly, one would have to classify phase transitions after Ehrenfest, i.e. via the investigation of discontinuities in derivatives of the grand canonical potential. For the purposes of this work only the behavior of the order parameter σ at the transition will be investigated. A first order transition is characterized by the non-differentiability of the chiral condensate as a function of the chemical potential at fixed T, while in a second order transition the chiral condensate changes continuously and is differentiable with respect to the chemical potential.

---

[16] In Sec. 3.1 σ' was defined as the chiral condensate, i.e. as the global minimum of the effective action (3.10). To simplify the notation σ is defined as the global minimum from now on.

The numerical methods discussed in the different sections of the Part III will be applied to the $2+1$-dimensional GN model and to its isospin asymmetric variant as defined in Sec. 3.4. The three phases from the test case $d = 1+1$ are expected to also exist for the $d = 2+1$-dimensional models from Refs. [27, 28, 37, 45, 46]. In the $2+1$-dimensional GN model the IP might only be present at a finite lattice spacing a, as indicated by recent results reported in Ref. [28]. For the $2+1$-dimensional GN model with "isospin" chemical potential the author is not aware of existing works. Note, however, that the chiral condensate in a possibly existing IP does not necessarily have a similar functional form as in $1+1$ dimensions, e.g. two-dimensional modulations could be preferred by the action. Thus, the approaches in this thesis to detect such an IP should, in principle, not rely on a specific ansatz for the chiral condensate.

5.3 Lattice data

		$N_{t,c}$	$a\sigma_0$	N_s	$L\sigma_0$
Sec. 6	$d = 1+1$	16	0.055	480	26.4
	$d = 2+1$	2	0.379	40	15.2
		3	0.237	60	14.2
		8	0.086	160	13.8
		8	0.086	300	25.8
	$d = 2+1$, $\mu_I \neq 0$	2	0.379	40	15.2
		3	0.237	60	14.2
		6	0.115	100	11.5
		6	0.115	120	13.8
Sec. 7	$d = 1+1$	2	0.444	50	22.2
		4	0.219	100	21.9
		8	0.109	200	21.8
	$d = 2+1$	2	0.379	40	15.2
		3	0.237	60	14.2
		4	0.174	80	13.9
		8	0.086	160	13.8
	$d = 2+1$, $\mu_I \neq 0$	2	0.379	40	15.2
Sec. 8	$d = 1+1$	2	0.444	50	22.2
	$d = 2+1$	2	0.379	40	15.2
		3	0.237	60	14.2
		4	0.174	80	13.9

Tab. 1: Lattice setups presented in the following sections. The data is ordered by the thesis section, i.e. by the respective method to determine a phase diagram, and, additionally, sorted by the respective models.

In Tab. 1 the lattice setups discussed in the respective section, i.e. for each of the different methods to determine a phase diagram, are presented. In general, often more investigations than recorded in Tab. 1 have been performed. For clarity only data sets that are mentioned in the respective section are listed. It is important to note that investigations of the continuum limit were performed for fixed ratio $N_{t,c}/N_s$, i.e. the ratio of temporal extent β_c at the critical temperature with the number of lattice sites in the spatial direction(s). As a consequence, the spatial lattice extent $L\sigma_0$ is not constant, since the determination of σ_0 depends on $N_{t,c}$ through its dependence on the tuned coupling λ as explained in Sec. 4.4. The results for the $2+1$-dimensional GN model are obtained with the irreducible, 2×2 fermion Rep. (3.20). These were cross-checked with reducible, 4×4 γ-matrices (Rep. (3.24)) for some $a\sigma_0$ and, as expected, gave the same results within the precision of the respective method. For the isospin asymmetric GN model reducible γ-matrices have to be used, since they are required in the introduction of the additional chemical potential.

6 The homogeneous phase diagram

In this section only spatially constant condensates, i.e. $\sigma(\mathbf{x}) = \sigma = \text{const}$, are allowed. The effective action on the lattice can then be evaluated in a very efficient way by using (4.15). It is also independent of the choice on the weight function W_D in the interaction term. First, the determination of the phase diagram and the distinction between the first and second order transitions are carried out.

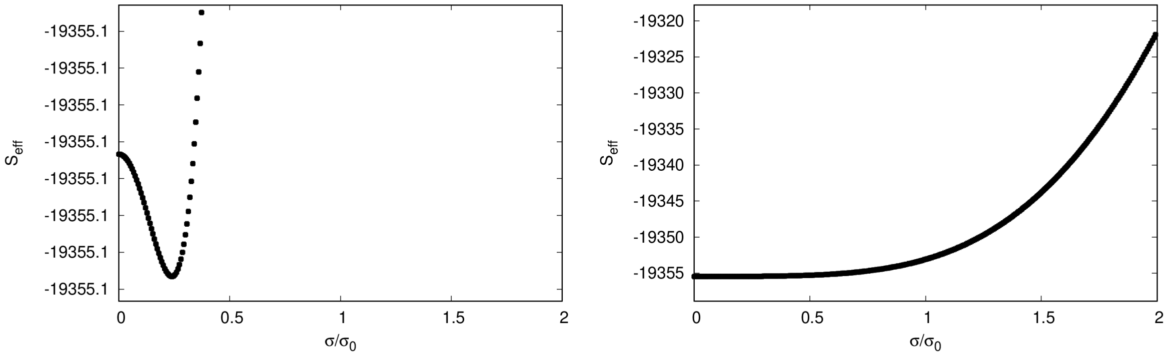

Fig. 6.1: S_{eff} for $d = 1 + 1$ as a function of σ for homogeneous σ and $T/\sigma_0 = 0.395$ (where the second order phase transition is at $\mu'/\sigma_0 = 0.564$). **(left)** $\mu/\sigma_0 = (\mu' - \Delta\mu)/\sigma_0$, inside the HBP, **(right)** $(\mu' + \Delta\mu)/\sigma_0$ with $\Delta\mu/\sigma_0 = 0.01$, inside the SP.

As a first step, $\partial^2 S_{\text{eff}}/\partial\sigma^2|_{\sigma=0}$ at fixed T as a function of μ is considered and its root μ' is determined by a standard bisection algorithm. If the phase transition is of second order, it is located at μ'. This is illustrated in Fig. 6.1, where S_{eff} for $T/\sigma_0 = 0.395$ is plotted as a function of σ for $\mu/\sigma_0 = (\mu' - \Delta\mu)/\sigma_0\,,\ (\mu' + \Delta\mu)/\sigma_0$ with $\Delta\mu/\sigma_0 = 0.01$. It is then checked, if there is a region $\mu \in [\mu', \mu'']$, where the global minimum of S_{eff} with respect to σ is smaller than $S_{\text{eff}}[\sigma = 0]|_{(\mu',T)}$, i.e. where the minimum point is at $\sigma \neq 0$ (for the minimizations a golden section search method is used). If this is the case, the phase transition is of first order and located at μ'', which is again determined by bisection. This is illustrated in Fig. 6.2, where S_{eff} for $T/\sigma_0 = 0.101$ is plotted as a function of σ for $\mu/\sigma_0 = 0.6\,,\ \mu''/\sigma_0\,,\ 0.8$. To determine the TCP, i.e. the change of the order of the phase transition, the fourth derivative $\partial^4 S_{\text{eff}}/\partial\sigma^4|_{\sigma=0}$ (4.18) as a function of T with μ fixed at $\mu = \mu'$ is considered and its sign change is determined[17]. At fixed λ T can only be varied in discrete steps, i.e. $T_{N_t} = 1/2N_t a$ by varying N_t. Consequently, one can determine a sign change only between $T_{N_t'-1}$ and $T_{N_t'}$. Then, the TCP is located

---

[17] Note that, in principle, the sign change in higher order derivatives of the effective action could lead to a first order transition. In practice, the chosen method in this thesis is often successful. This is cross-checked by the above algorithm to determine first and second order boundaries.

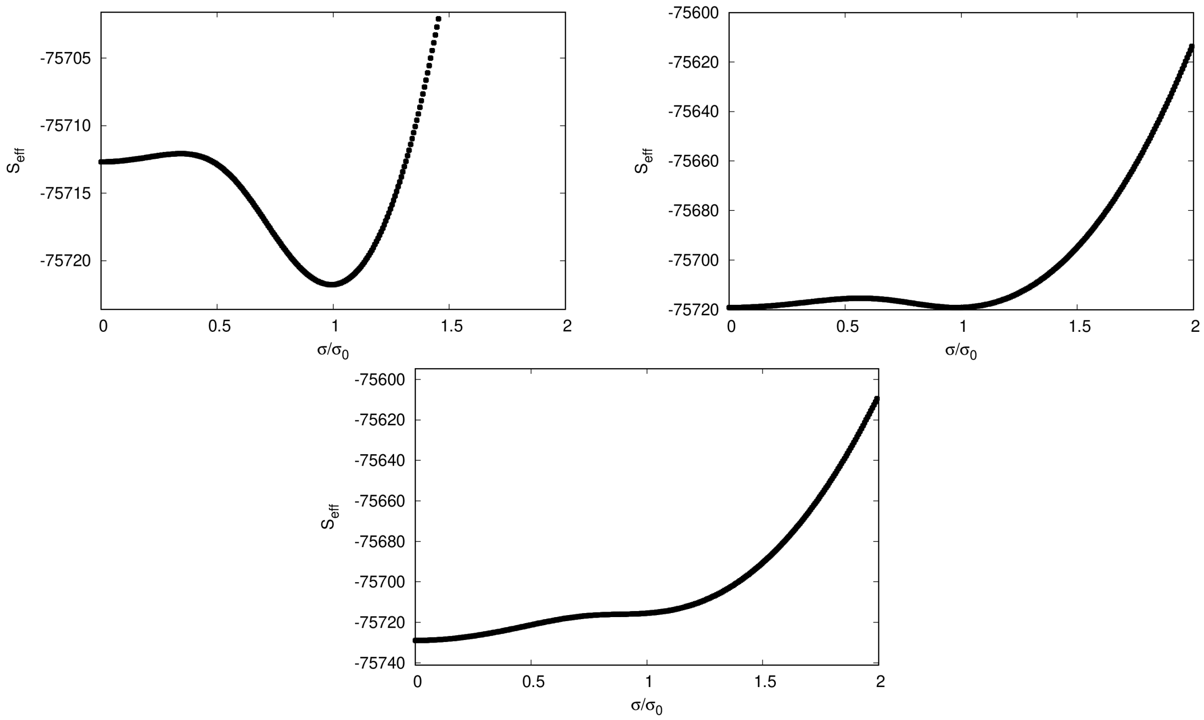

Fig. 6.2: S_{eff} for $d = 1+1$ as a function of σ for homogeneous σ and $T/\sigma_0 = 0.101$ (where the first order phase transition is at $\mu''/\sigma_0 = 0.687$). **(top left)**$\mu/\sigma_0 = 0.6$, inside the HBP, **(top right)** $\mu/\sigma_0 = \mu''/\sigma_0$, at the phase transition **(bottom)** $\mu/\sigma_0 = 0.8$, inside the SP.

between $T_{N'_t-1}$ and $T_{N'_t}$ at $\mu = \mu'$. We do not plot the TCP, as it can be visualized by the change in the order of the phase transition.

6.1 The $1+1$-dimensional Gross-Neveu model

The resulting phase diagram of the 1+1-dimensional GN model for a homogeneous chiral condensate is shown in Fig. 6.3 and is in good agreement with the analytical result in Ref. [47]. A second order boundary from the homogeneous broken phase to the symmetric phase at $T/\sigma_0 > 0.33$ with $a\sigma_0 = 0.055$ is obtained. Here, the cutoff effects are neglectable in comparison to [47]. At fixed lattice spacing, the phase boundary is relatively stable for a finite volume $L\sigma_0 > 9$. Close to the continuum limit, i.e. at $a\sigma_0 = 0.055$, a deviation of the phase transition towards a slightly larger chemical potential ($\sim 0.001\sigma_0$) at a fixed temperature is observed compared to that in the continuum theory. This rather small deviation is caused by the finite cutoff. Such an effect can also be observed in the lattice investigation [28]. The deviation gets smaller when further decreasing the lattice spacing. Besides this small effect the phase boundary is in agreement with the analytical result represented by the blue lines. In between $T/\sigma_0 = 0.324, \mu/\sigma_0 = 0.607$

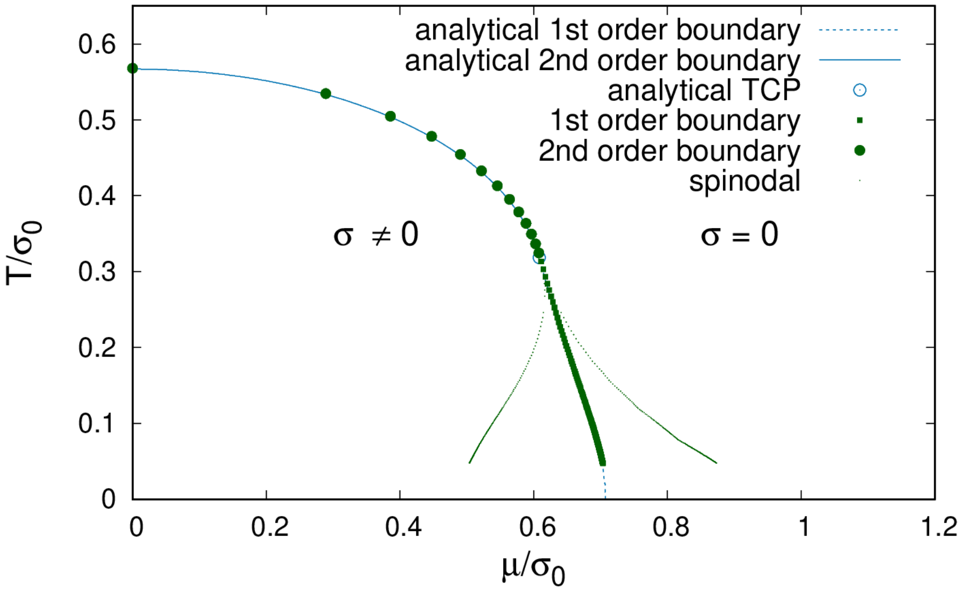

Fig. 6.3: Phase diagram of the $1+1$-dimensional GN model in the μ-T plane for $\sigma = \text{const}$. The blue lines represent the analytical solution from Ref. [47]. The green points are obtained with $a\sigma_0 = 0.055$.

and $T/\sigma_0 = 0.313, \mu/\sigma_0 = 0.611$ a TCP is found, where the second-order phase transition turns into a first-order one. This result agrees with the analytical result, where the TCP is located at $T/\sigma_0 = 0.318, \mu/\sigma_0 = 0.608$. In addition to the phase boundaries the left and right spinodal are presented. The left spinodal, i.e. the root of $\partial^2 S_{\text{eff}}/\partial\sigma^2|_{\sigma=0}$ as a function of the chemical potential while no phase transition at this root is observed, turns towards smaller chemical potentials $\mu/\sigma_0 \gtrsim 0.5$, while the right spinodal, i.e. the chemical potential at fixed T where a local minimum at $\sigma \neq 0$ in the SP occurs, bends towards larger chemical potentials $\mu/\sigma_0 \lesssim 0.9$. The author is not aware of published results for the two spinodals and, hence, cannot compare them to the literature.

6.2 The $2+1$-dimensional Gross-Neveu model

In Fig. 6.4 the phase diagram of the $2+1$-dimensional GN is presented for homogeneous chiral condensates and compared to the analytical second order transition from Ref. [45]. Two different lattice spacings at fixed ratio $N_{t,c}/N_s$ are plotted in the upper panel to visualize cutoff effects. At a relatively large lattice spacing $a\sigma_0 = 0.379$ and large volume $L\sigma_0 = 15.2$, plotted with red points, a strong deviation towards smaller chemical potentials for larger T in comparison with the analytical solution is observed. The TCP is located between $T/\sigma_0 = 0.189$, $\mu/\sigma_0 = 0.974$ and $T/\sigma_0 = 0.165$, $\mu/\sigma_0 = 0.978$, while in the analytical phase diagram no first order transition is found for finite T. With decreasing T the transition, albeit of first order, bends towards $\mu/\sigma_0 \lesssim 1.0$, i.e. it comes

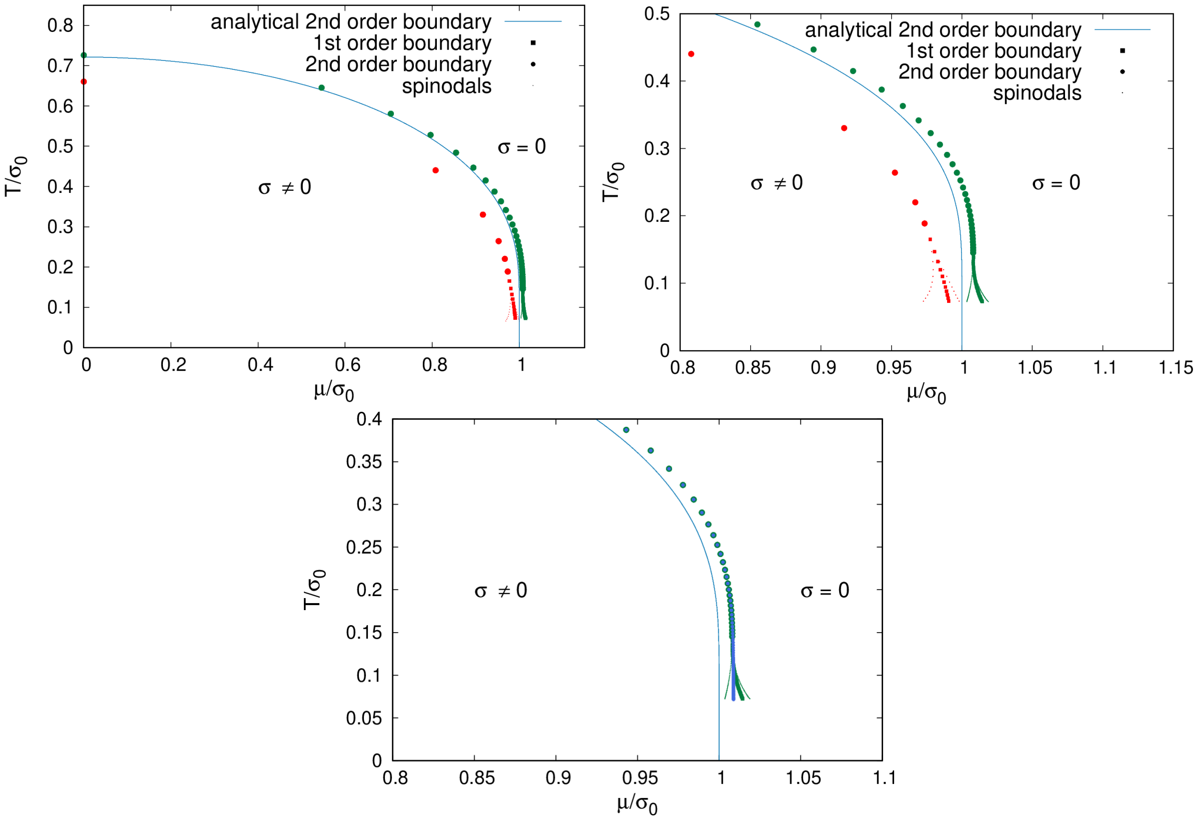

Fig. 6.4: Phase diagram of the $2+1$-dimensional GN model in the μ-T plane for $\sigma = \text{const}$. The blue lines represent the analytical second order phase boundary from Ref. [45]. **(top)** The phase diagram obtained with two different lattice spacings at a fixed ratio $N_{t,c}/N_s = 2/40 = 8/160$ to illustrate cutoff effects. The red dots are obtained with $a\sigma_0 = 0.379$ and $L\sigma_0 = 15.2$, the green dots with $a\sigma_0 = 0.086$ and $L\sigma_0 = 13.8$. The right-sided plot is a zoomed in version of the left-sided one. **(bottom)** The phase diagram obtained for $a\sigma_0 = 0.086$ for two different spatial extents, i.e. $L\sigma_0 = 13.8$ (green points)) and $L\sigma_0 = 25.8$(blue points), to illustrate finite volume effects. The keys of the above two plots also apply in the bottom panel.

closer to the result of Ref. [45]. However, for some lattice spacings the first order phase transition exceeds even $\mu/\sigma_0 > 1.0$. The left spinodal bends towards a smaller chemical potential $\mu/\sigma_0 \gtrsim 0.95$, while the right spinodal bends towards slightly larger chemical potential compared to the first order transition. With decreasing chemical potential the TCP moves towards lower temperatures and the differences of the spinodals to the first order boundary get smaller. With $a\sigma_0 = 0.086$ and $L\sigma_0 = 13.8$ a line of second order phase transitions is observed at $T/\sigma \geq 0.145$. Below this temperature a first order transition is obtained. The phase boundary is already in relatively good agreement with the analytical result for $T > 0.145$. One observes a deviation of the transition towards a slightly larger chemical potential ($\sim 0.02\sigma_0$). This temperature independent deviation is mainly a cutoff effect, as it gets slightly smaller when decreasing $a\sigma_0$ further. The effect is also visible in Ref. [28]. As can be seen in the lower panel of Fig. 6.4, the finite volume still causes a growing deviation towards larger chemical potentials of the first order transition at small temperatures below $0.15\sigma_0$. This deviation can also be observed in [28], but, as therein, they always minimize the effective action, they do not differentiate between first and second order transitions. At $a\sigma_0 = 0.086$ and $L\sigma_0 = 25.8$ a second order phase boundary is obtained for temperatures above $T/\sigma_0 = 0.072$, which is the lowest temperature investigated. A TCP is, due to the larger volume, not observed. Besides the remaining, cutoff-caused small deviation towards slightly larger chemical potentials this line of second order boundaries seems to be quite close to the infinite-volume, continuum result. The temperature, at which the TCP is located, and the size of the region enclosed by the two spinodals is, however, influenced not only by the finite volume but also by the cutoff, as can be seen from the data in the upper right plot of Fig. 6.4. Here, the temperature, where the order of the phase transition changes, shrinks to $T/\sigma_0 = 0.141$ when decreasing the lattice spacing to $a\sigma_0 = 0.086$. The occurrence of a first order transition is a combined effect of a finite cutoff and volume, but at lower temperatures it seems to be dominated by the finite volume.

For the interested reader, a few additional remarks about the combined effects of finite volume and finite lattice spacing are now given. For $4.0 < L\sigma_0 < 8.0$ a strong deviation towards larger chemical potentials for temperatures $T/\sigma_0 < 0.4$ is obtained and the TCP is located at relatively high temperatures. This has been observed for $a\sigma_0 = 0.379$ and $a\sigma_0 = 0.237$. For even smaller $L\sigma_0 < 4.0$ the HBP thins out extremely, as the finite volume and its boundary conditions have strong effects on the phase boundary. For large enough L, the phase transition at larger temperatures is relatively stable against variations in the lattice spacing for $a\sigma_0 < 0.15$. For lower temperatures $T/\sigma_0 < 0.2$, however, the finite volume has effects on the order of the phase boundary, as described above. This is probably caused by large temporal extents at low temperatures.

6.3 The isospin asymmetric 2+1-dimensional Gross-Neveu model

For the $2+1$-dimensional GN model with isospin chemical potential the same algorithms as for the previous models are used. However, due to the additional parameter μ_I, either μ_I or μ must be fixed, to perform bisections of the remaining parameter. In practice, the calculation is performed with one of the two chemical potentials fixed, while the other is varied in discrete steps of $\Delta\mu_I = \Delta\mu = 0.01$. Since a first impression of the phase diagram is of interest, one does not differentiate between second and first order boundaries, nor does one compute a line of TCPs and spinodals. The phase transition is, thus, determined via minimization of the effective action. In Fig. 6.5 the resulting phase diagram for $a\sigma_0 = 0.115$ is plotted. The black points represent a phase transition, while the blue crosses are leftovers from the bisection and visualize that the system is already in the SP. As one might imagine, it is numerically difficult to determine the

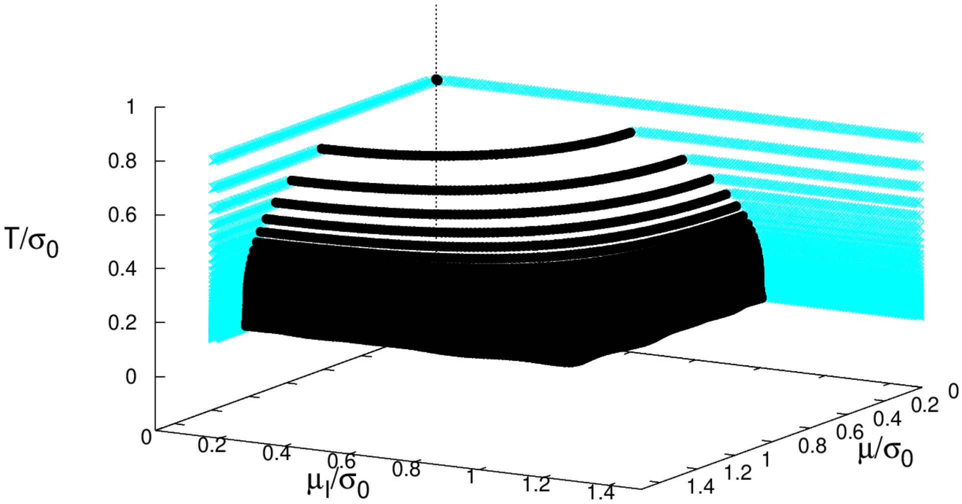

Fig. 6.5: Phase diagram of the isospin asymmetric $2+1$-dimensional GN model for $\sigma = \text{const}$ for three parameters μ, μ_I and T. The black dots are obtained through minimization of the effective action with $a\sigma_0 = 0.115$. The blue crosses represent no phase transition, as the system is already in the SP.

phase boundary around $\mu_I/\sigma_0 = 1.0$ via bisection in μ and, vice versa, for the phase boundary around $\mu/\sigma_0 = 1.0$ via bisection in μ_I. Consequently, the data points in Fig. 6.5 result from two independent calculations, in which a different one of the two chemical potentials was fixed. To avoid the described numerical difficulties at larger phase boundaries, the data points at $\mu_I < \mu$ are determined via bisection in μ, while at $\mu_I \geq \mu$ a bisection in μ_I is used.

Note that in case of $\mu/\sigma_0 = 0.0$ (with the redefinition $\mu_I \equiv \mu$) or $\mu_I/\sigma_0 = 0.0$ the phase boundary is similar to the ordinary $2+1$-dimensional GN model. This is expected, as discussed in Sec. 3.4. For $T/\sigma_0 > 0.3$ a rotational symmetry is observed in the μ-μ_I plane, i.e. the location of phase transition (μ'', μ_I'') for fixed T seems to be given by $\sqrt{(\mu_I'')^2 + (\mu'')^2} = \mu'$, where μ' is the phase transition to the SP for $\mu_I = 0.0$, suggesting an internal symmetry of the theory which was theoretically unobserved. However, for lower temperatures this is clearly not the case. The behavior of the phase transition is investigated in the μ-T plane for different μ_I in Fig. 6.6. As observed here, the phase transition for $T \leq 0.1$ is relatively unaffected by the isospin chemical potential, e.g. for $\mu_I/\sigma_0 = 0.96$ and $T/\sigma_0 \approx 0.07$ a phase transition is still observed at the relatively large chemical potential $\mu/\sigma_0 \approx 0.99$. An idea, that could explain this behavior, might be the decoupling of the two species of fermions with different chemical potentials, $\mu + \mu_I$ for "isospin-up" fermions and $\mu - \mu_I$ for "isospin-down" fermions, respectively. For μ and μ_I around σ_0 one type of fermion is always in the HBP while the other is already in the SP. As a consequence, the whole system should be in the HBP. It is, however, unclear, why this is not the case for higher temperatures. As shown in Sec. 3.4 Eq. (3.49), Fig.

6.6 would look similar if μ and μ_I were exchanged. In principle, only calculations for $\mu \leq \mu_I$ (or vice versa) are necessary when taking account of this property. It is a good cross-check for the numerical result that this is indeed fulfilled.

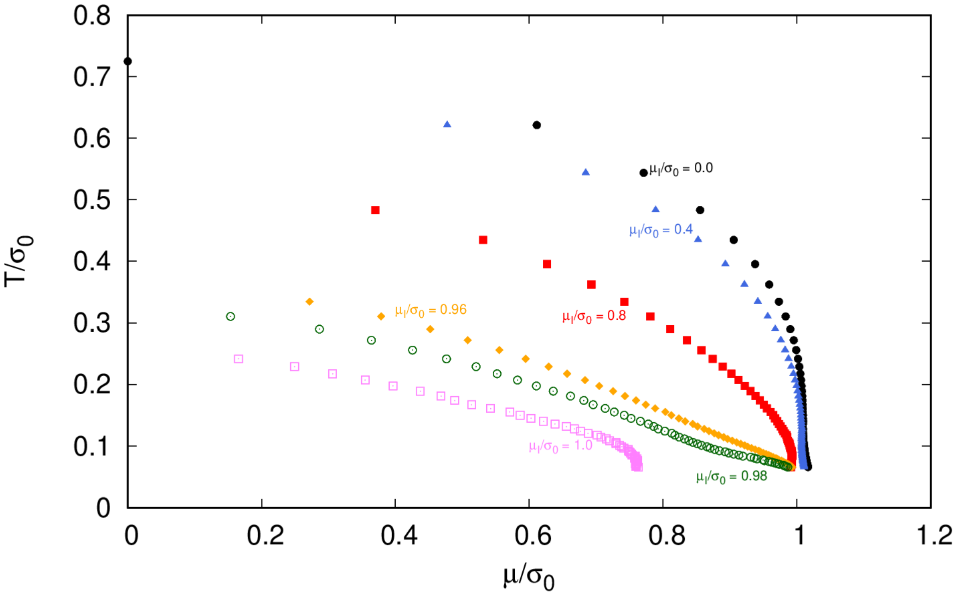

Fig. 6.6: Phase diagram of the isospin asymmetric $2+1$-dimensional GN model for $\sigma = \text{const}$ in the μ-T plane for several μ_I. The phase transitions are obtained through minimization of the effective action for $a\sigma_0 = 0.115$.

Similarly to the ordinary $2+1$-dimensional GN model the phase transition is already relatively close to the infinite volume and continuum limit in the setup presented ($a\sigma_0 = 0.115$, $L\sigma_0 = 13.8$). For $\mu_I = 0.0$, there is a slight deviation towards larger chemical potentials, which is explained in Sec. 6.2. However, the phase boundary for finite μ_I is not expected to be drastically affected by finite lattice spacing and volume for this setup. The phase diagram seems to respond to finite volume and the lattice discretization quite similarly to the model with $\mu_I = 0.0$, which has been described in detail in Sec. 6.2. This has been checked for three different a at fixed ratio $N_{t,c}/N_s$ and two different V for fixed a. The lattice setups are listed in Tab. 1.

7 Stability analysis for spatially varying chiral condensate

To obtain the phase diagram of the GN model, allowing for inhomogeneous chiral condensates $\sigma(\mathbf{x})$, one must minimize the effective action as a functional of $\sigma(\mathbf{x})$. In principle, this is possible using lattice field theory. Here, the problem reduces to the minimization of (4.7) in N_s^D variables σ_j, which represent $\sigma(\mathbf{x})$ on the lattice sites. Finding the global minimum of a function of many variables is a very challenging task. Therefore, the modulation of σ is restricted to one spatial direction, i.e. $\sigma(\mathbf{x}) = \sigma(x_1)$. Motivated by the analytical result in $1+1$ dimensions [9], where one finds a second order transition from the SP to the IP, one begins a study of IP by performing stability analyses with respect to $\sigma = 0$. On the lattice this amounts to finding the eigenvalues and eigenfunctions of the Hessian matrix

$$H_{jk} = \frac{\partial^2}{\partial\sigma_j\partial\sigma_k} S_{\text{eff}}\left(\sigma_0 = \sigma_1 = \ldots = \sigma_{N_s-1} = 0\right) , \tag{7.1}$$

where negative eigenvalues indicate directions in the multidimensional σ_i space, in which S_{eff} decreases. The smallest eigenvalue η of the Hessian matrix is considered as a function of μ at fixed T and its root μ' is determined by a bisection algorithm. By comparison with the boundary obtained via full minimization for $\sigma = \text{const.}$ (compare Sec. 6) one can identify regions, where at fixed (μ, T) a spatially varying condensate $\sigma(x_1)$ leads to a decrease in the effective action compared to $S_{\text{eff}}|_{\sigma=0}$. Note that the root found at chemical potential μ' does not necessarily correspond to a phase transition. It only separates a region, where the SP is stable (i.e. no negative eigenvalues of H), from another region, where $\sigma = 0$ is not preferred (i.e. at least one negative eigenvalue of H).

In the continuum the Hessian matrix becomes an infinite operator which, in principle, can be analytically diagonalized to yield the eigenvalues. The smallest eigenvalue must now be found by a one-dimensional minimization of this function, which is done in our upcoming publication [29]. It is important to note that the restriction $\sigma(\mathbf{x}) = \sigma(x_1)$, that is applied in the $2+1$-dimensional models in Sec. 7.2 does not change the line of instability in the continuum limit, as proven in a momentum space analysis in Ref. [29], where the line of instability only depends on the 2-norm $\|\mathbf{p}\|$, where $\mathbf{p} = (p_1, p_2)$ is the momentum of the chiral condensate.

7.1 The $1+1$-dimensional Gross-Neveu model

Results for the two different lattice discretizations, discussed in Sec. 4 and App. C, are presented in Fig. 7.1. In the left panel $W_1 = W_1'$, as defined in Eq. (4.12), is used for the interaction term in Eq. (4.11) following Ref. [16], while in the right panel W_1'' (4.13)

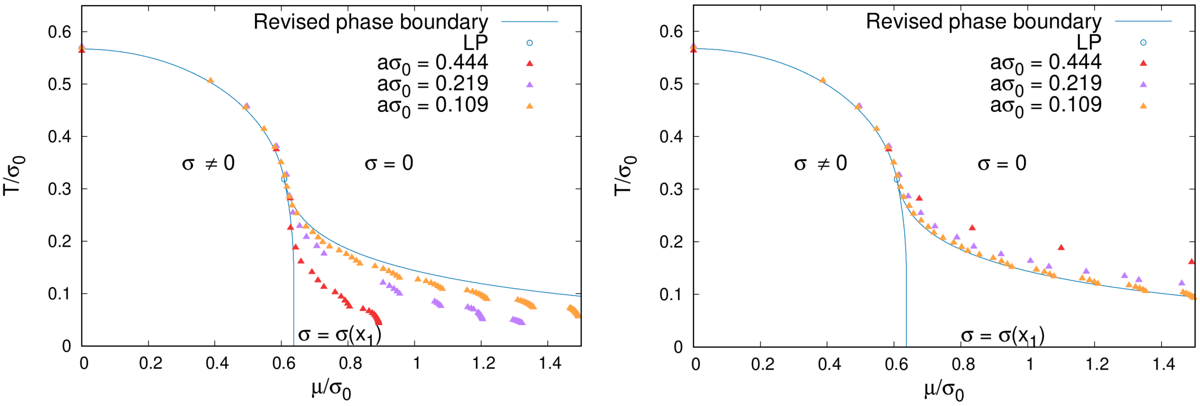

Fig. 7.1: The "phase diagram" via stability analysis for three different lattice spacings. The triangular data points are obtained by stability analysis with respect to $\sigma = 0$ (compare Eq. (7.1)). The analytical phase diagram in the continuum is from Ref. [9]. **(left)** $W_1\,(x_1 - y_1) = W_1'(x_1 - y_1)$. **(right)** $W_1\,(x_1 - y_1) = W_1''\,(x_1 - y_1)$.

is used. The line of instability obtained via the Hessian matrix (7.1) is represented with triangles. Three different lattice spacings at fixed ratio $N_{t,c}/N_s$ are studied to test the convergence of both discretizations to the solution [9] in the continuum limit.

For $W_1 = W_1'$ the inhomogeneous region is relatively small for the larger lattice spacing, i.e. for the red triangle data with $a\sigma_0 = 0.444$. However, by increasing the lattice spacing, the line of instability comes relatively close to the continuum results, i.e. to larger chemical potentials. In contrast, a deviation to larger chemical potentials compared to the continuum theory for $W_1 = W_1''$ at the largest lattice spacing is observed. When decreasing a, the line of instability nevertheless converges to smaller chemical potentials and to the correct phase transition. In a comparison of both given lattice data the discretization of the interaction term with W_1'' seems to approach the continuum limit faster. Besides the cutoff effects, both curves suffer from finite volume effects. They do not describe a smooth line. As explained in Sec. 5 the frequency of the chiral condensate in the inhomogeneous phase increases with the chemical potential. Due to the finite volume, the system can only adapt wavelengths that are natural dividers of the finite volume. This finite volume effect results in oscillations and deviations towards smaller chemical potentials in the phase boundary on a finite sized lattice, as observed in Ref. [48]. This effect will be discussed in more detail for the $2 + 1$-dimensional GN model. The oscillations in the boundary can be removed via a method discussed in Refs. [39, 48]. For a more detailed discussion the reader is referred to these references and Sec. 7.2.3, where the infinite volume result is obtained for the $2+1$-dimensional GN model.

To summarize, besides the under-control finite volume effects the numerical stability analysis on the lattice converges to the analytical result in the continuum limit, which is expected as the transition from the SP to the two other phases is of second order. Due to the nature of the method only phase transitions from the SP are obtained. As already explained in the beginning of this section, one cannot calculate transitions between the HBP and the IP by this method. In the application of the $2+1$-dimensional models, one might be able to identify regions, where an inhomogeneous chiral condensate might lower the effective actions, when comparing the line of instability to the homogeneous calculations from Sec. 6.

7.2 The $2+1$-dimensional Gross-Neveu model for $\sigma(\mathbf{x}) = \sigma(x_1)$

Again, results for the two different lattice discretizations presented in Sec. 4 and App. C are presented in Fig. 7.2 at a finite lattice spacing $a\sigma_0 = 0.379$. The red triangles represent the line of instability obtained through the Hessian matrix (7.1). Again, it is noted that the red triangles do not necessarily correspond to a phase boundary, even though they could coincide with a phase boundary, as was observed in Sec. 7.1 for the $1+1$-dimensional GN model. The other boundaries are obtained via minimization of the effective action for $\sigma = \text{const.}$ from Fig. 6.4. For a detailed discussion the reader is referred to Sec. 6.

In the left panel of Fig. 7.2, W_1' is used for the discretized interaction term in Eq. (4.11) following Ref. [16]. Here, the stability analyses via the Hessian matrix (7.1) leads to the same μ' as the homogeneous calculations of the second order boundary and the left spinodal, as indicated by the red dots. Consequently, one cannot identify an IP even for very large a through a second order transition from the chirally symmetric phase. Nevertheless, there might be an IP that is connected by a first order transition to the homogeneous phases. This possibility will be investigated by performing multiple full multi-dimensional minimizations of S_{eff} using a conjugate gradient algorithm in Sec. 8.

In the right panel of Fig. 7.2, where W_1'' is used as weighting function for the interaction term in Eq. (4.11), significantly different results are observed. This discretization is similar to Ref. [28], but the ansatz is more general, since in Ref. [28] the chiral condensate is restricted to a specific harmonic mode $\tilde{\mathbf{k}}$ while using the naive discretization without a modification of the interaction term. This corresponds to a weight function in Fourier space $\tilde{W}_2'''(\mathbf{k}) = \delta_{\mathbf{k},\tilde{\mathbf{k}}}$. Consequently, this ansatz is included in our discretization W_2'' and the resulting inhomogeneous phase must have at least the same size in a true minimization. However, as we restrict our chiral condensate to depend only on one dimension, results from Ref. [28] can only be compared for $\tilde{\mathbf{k}} = (\tilde{k}_1, 0)$.

A triangular region is observed, where an inhomogeneous chiral condensate $\sigma = \sigma(x_1)$ leads to a decrease in the effective action compared to $S_{\text{eff}}\big|_{\sigma=0}$, between the red dots and

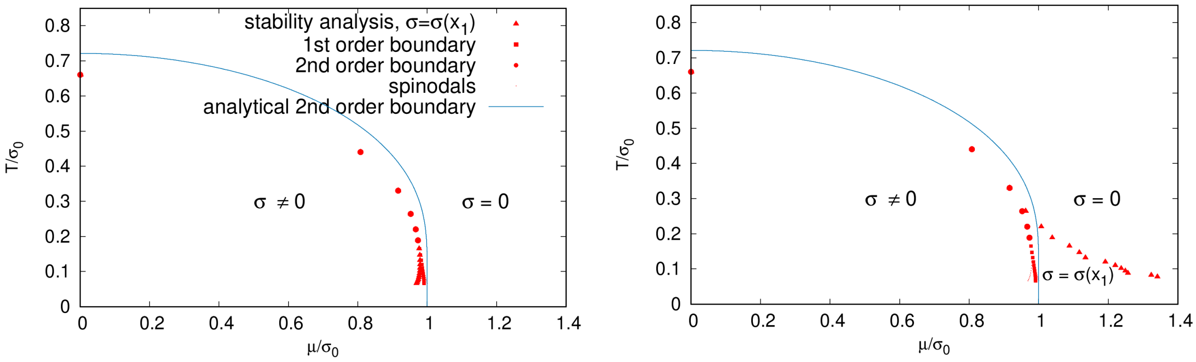

Fig. 7.2: The "phase diagram" via stability analysis. The phase boundary for σ = const. is the same as in Fig. 6.4. The triangular dots are obtained by stability analysis with respect to $\sigma = 0$ (compare (7.1)). The lattice spacing is $a\sigma_0 = 0.379$ for a fixed volume ($L\sigma_0 = 15.2, N_{t,c} = 2, N_s = 40$). The legend in the left panel holds for both phase diagrams. **(left)** $W_1\,(x_1 - y_1) = W_1'(x_1 - y_1)$. The line of instability via the Hessian matrix (7.1) corresponds to the homogeneous calculation of the second order boundary and the left spinodal. **(right)** $W_1\,(x_1 - y_1) = W_1''\,(x_1 - y_1)$. The triangular region enclosed by the red dots is part of an IP.

the homogeneous calculation from Fig. 6.3. This region is located at $\mu/\sigma_0 \geq 0.96$ and $T/\sigma_0 \leq 0.26$ and unambiguously signals the existence of an IP, which covers the triangular region. The LP, which is defined here as the point where instability begins to be caused by inhomogeneous chiral condensates, is located at $T/\sigma_0 = 0.264, T/\sigma_0 \approx 0.963$. The inhomogeneous region might, however, have a larger extension. Note that the red dots do not seem to correspond to a smooth curve. This is a finite-volume effect, similar to that observed in the lattice field theory study of the $1+1$-dimensional GN model and in Refs. [39, 48].

In Fig. 7.3 two examples of eigenvectors of the Hessian matrix (7.3) are shown corresponding to negative eigenvalues for $W_1 = W_1''$ in the observed inhomogeneous region. Although these eigenvectors do not correspond to the global minimum of S_{eff}, they indicate the shape of the spatial modulations of the chiral condensate $\sigma(x_1)$, which lower the effective action locally around and with respect to $\sigma = 0$, i.e. $S_{\text{eff}}[\alpha v(x_1)] < S_{\text{eff}}[0]$, where $v(x_1)$ is the normalized eigenvector and α is a relatively small amplitude. Exactly at the line of instability towards the SP, they describe the preferred shape of the chiral condensate very well, although they do not give the correct amplitude of the inhomogeneity. Within the triangular region, where an inhomogeneous chiral condensate is preferred over a homogeneous σ, the obtained eigenvectors corresponding to negative eigenvalues have a sin-like shape. At fixed temperature the wave number increases for increasing chemical potential, a behavior also observed for the $1+1$-dimensional GN model [9, 44]. In a finite volume, the corresponding frequencies can only increase in discrete steps, since only wavelengths which fit in the finite spatial extent with periodic

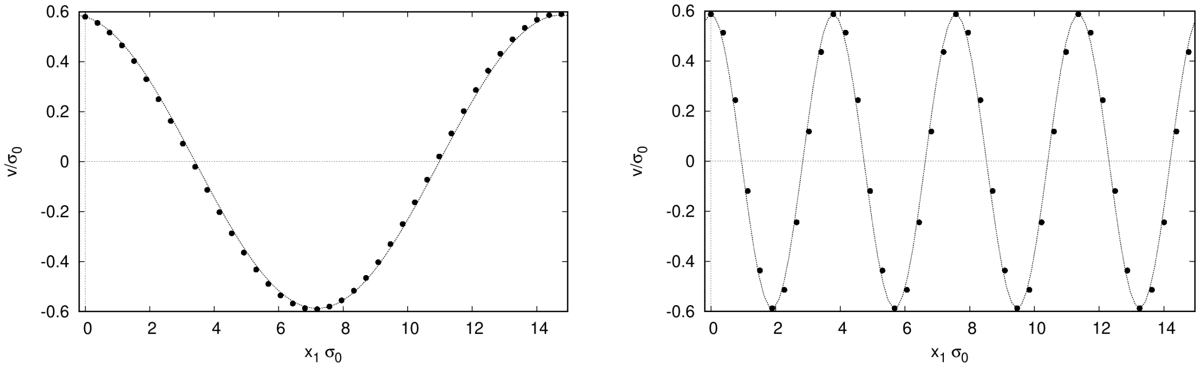

Fig. 7.3: Eigenvector $v(x_1)$ of the Hessian matrix (7.1) corresponding to the smallest, negative eigenvalue for $a\sigma_0 = 0.379$. These normalized eigenvectors are functions that for an infinitesimal amplitude lead to lower effective actions than $S_{\text{eff}}[0]$ and, hence, indicate the possible shape of the chiral condensate. The dashed lines are cos-functions with the same frequency as the eigenvectors. **(left)** $\mu/\sigma_0 = 0.984$, $T/\sigma_0 = 0.165$. **(right)** $\mu/\sigma_0 = 1.085$, $T/\sigma_0 = 0.165$.

boundary conditions can be adapted. This explains the oscillatory behavior of the line of instability observed in the right panel of Fig. 7.2. This will be explained in more detail in Sec. 7.2.3. The behavior of the chiral condensate, i.e. the global minimum of the effective action, is studied in Sec. 8.2.

7.2.1 Continuum limit

At finite a, one obtains an IP for $W_1 = W_1''$, while for $W_1 = W_1'$ an IP is not found. Based on this result, a detailed investigation of the continuum limit is necessary, since both discretizations should lead to the same phase diagram in the continuum. In Fig. 7.4, the continuum limit is performed by increasing $N_{t,c}$, i.e. decreasing a, at fixed ratio $N_{t,c}/N_s$ for three different lattice spacings. In the right panel for $W_1 = W_1''$ the inhomogeneous region shrinks for $a \to 0$. As discussed before, the line of instability, that is obtained via the stability analysis, suffers from finite volume effects, which can, in principle, be removed. However, for $a\sigma_0 = 0.379$ the phase is present up to $\mu/\sigma_0 \leq 1.38$. The phase diagram looks qualitatively similar to that of the $1+1$-dimensional GN model. The LP is located at $T/\sigma_0 \approx 0.26$. For $a\sigma_0 = 0.174$ the SP is favored for $\mu/\sigma_0 \geq 1.06$, i.e. the line of instability is located at much smaller chemical potentials. The LP is also obtained at lower temperatures $T/\sigma_0 \approx 0.20$. This clearly supports a vanishing of the triangular region, which proves the existence of an IP. The line of instability converges towards the analytical solution from Ref. [45] without any indication of an IP.

In the phase diagram in the left panel the calculated line of instability does not differ from the homogeneous calculations. Thus, an inhomogeneous region is not observed

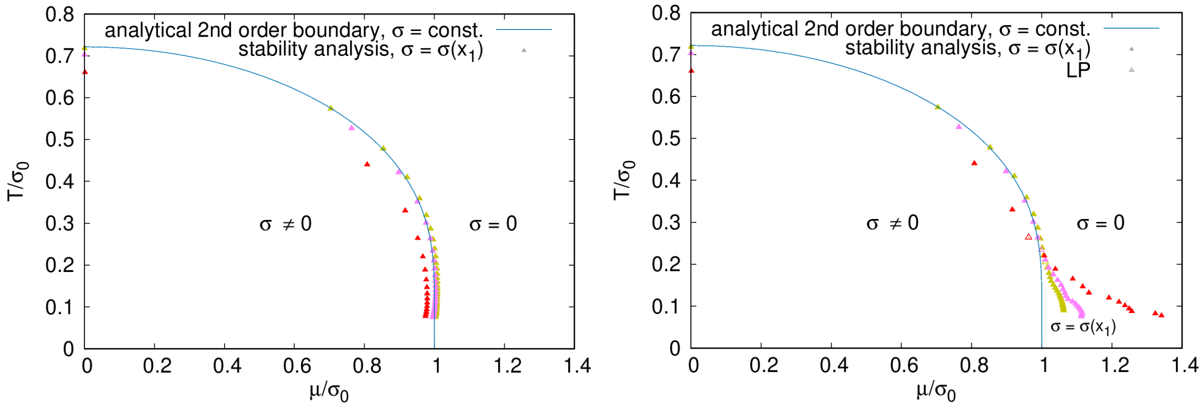

Fig. 7.4: The "phase diagram" via stability analysis for three different cutoffs. The blue line is the result from the continuum stability analysis for $\Lambda/\sigma_0 = \infty$. Results are presented from stability analyses on the lattice with $\sigma = \sigma_{x_1}$ for three different lattice spacings. The red triangles correspond to $a\sigma_0 = 0.379$, the pink triangles correspond to $a\sigma_0 = 0.237$ and the yellow triangles correspond to $a\sigma_0 = 0.174$. The respective empty triangles show a pseudo LP where instabilities change from homogeneous modulations to inhomogeneities. **(left)** $W_1\,(x_1 - y_1) = W_1'(x_1 - y_1)$. **(right)** $W_1\,(x_1 - y_1) = W_1''\,(x_1 - y_1)$. Both discretizations approach the homogeneous second order boundary from Ref. [45] for $a \to 0$.

with this method. For decreasing lattice spacing the stability analysis approaches the result for $\sigma =$ const. from Sec. 6.2 similar to the homogeneous phase diagram, i.e coming from smaller chemical potentials. For the lowest, studied lattice spacing $a\sigma_0 = 0.174$ one might observe a deviation towards larger chemical potentials at temperatures above $0.15\sigma_0$, and a backbending of the line of instability below this temperature compared to the homogeneous solution [45]. The latter is mainly a finite volume effect, as for a homogeneous condensate a first order boundary occurs, which cannot be detected by the stability analysis. The line of instability then corresponds to the left spinodal. The deviation towards larger chemical potentials is a cutoff effect. These effects are explained in detail in Sec. 6.2.

Taking the cutoff and finite volume effects into account and comparing with the homogeneous phase diagram, both discretizations converge to the second order line from Ref. [45]. Due to these results a vanishing of the inhomogeneous region for $a \to 0$ is anticipated supporting the lattice investigation in Ref. [28]. Similarities and differences of this investigation to our methods are now briefly discussed. In this work, only one-dimensional modulations without a specific ansatz are allowed, while in [28] the chiral condensate is investigated with the ansatz $\sigma = \alpha_{\mathbf{q}} \cos(2\pi \mathbf{q}\mathbf{x}/L)$. Indeed, the approach of this section allows the chiral condensate to take any functional form. Nevertheless, only one-dimensional chiral condensates are allowed for, so one can only compare to results with $\mathbf{q} = (q_1, 0)^{\mathrm{T}}$. However, the numerically costly stability analysis for $\sigma = \sigma(x_1, x_2)$ should not lead to a different line of instability for the GN model in the continuum limit, as proven through continuum stability analysis in momentum space in [29]. It is shown there that the line of instability only depends on $\|\mathbf{q}\|$. However, allowing $\sigma = \sigma(x_1, x_2)$ instead of $\sigma(x_1)$ in full minimizations of the effective action might, however, lead to a significant change in the phase structure, e.g. via a first order transition towards inhomogeneous chiral condensates.

Summarizing these findings, an IP is not found in the continuum limit via the stability analysis. The line of instability found via computation of Eq. (7.1) approaches the second order boundary between the HBP and the SP as found in Ref. [45] for both discretizations used. In the following section, the continuum limit of the effective action in the IP will be investigated to further support this result.

7.2.2 The effective action in the inhomogeneous phase for $a \to 0$

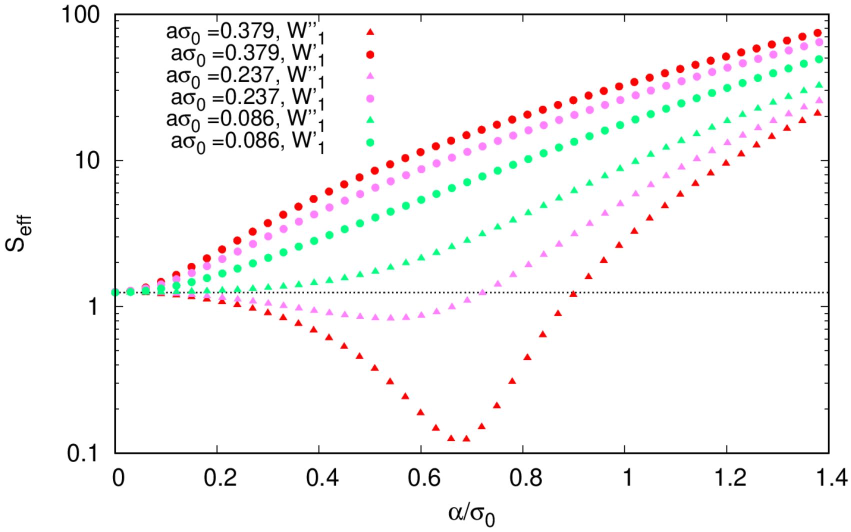

Fig. 7.5: $S_{\text{eff}}(\alpha)$ with $\sigma(x_1) = \alpha\cos(6\pi x_1/L)$, i.e. a wave with period $L/3$, for three different lattice spacings a at $\mu/\sigma_0 = 1.035$, $T/\sigma_0 \approx 0.11$. The action for both $W_1(x_1 - y_1) = W_1'(x_1 - y_1)$ and $W_1(x_1 - y_1) = W_1''(x_1 - y_1)$ is plotted. $S_{\text{eff}}(0)$ is set to 1.25. One can see that both actions approach each other for $a \to 0$. The data can be qualitatively compared to Fig. 8 of Ref. [28] for $\mathbf{q} = (3, 0)$.

The continuum limit can be applied in a straightforward way on the level of the effective action S_{eff} at[18] $\mu/\sigma_0 = 1.035$, $T/\sigma_0 \approx 0.11$ for a specific ansatz $\sigma(x_1) = \alpha\cos(6\pi x_1/L)$, i.e. a wave with wavenumber 3 in the finite periodic lattice. This ansatz is motivated by an eigenvector, that corresponds to a negative eigenvalue for $a\sigma_0 = 0.379$ and

---

[18] It is noted that due to the discretization of the temporal direction the observed values of T fluctuate around $0.001\sigma_0$ between the three lattice spacings. The influence of these fluctuations on the effective action should, however, be neglectable.

$a\sigma_0 = 0.237$, and is similar to the investigation in Ref. [28] with $\mathbf{q} = (3,0)^{\mathrm{T}}$. In Fig. 7.5 the effective action, which is now a function of the amplitude α, i.e. $S_{\text{eff}}[\sigma] = S_{\text{eff}}(\alpha)$, is plotted. To visualize the functional behavior of the effective action in a logarithmic plot, a constant with no physical meaning is added to S_{eff} such that $S_{\text{eff}}(0) = 1.25$. This plot agrees the phase diagram plotted in Fig. 7.4. For $W_1 = W_1'$, a global minimum $\alpha' = 0$ is obtained for all three lattice spacings $a\sigma_0$. For $W_1 = W_1''$, however, a minimum $\alpha' \neq 0$ is obtained for $a\sigma_0 = 0.379$ and $a\sigma_0 = 0.237$. The difference $\epsilon = \left|S_{\text{eff}}(\alpha') - S_{\text{eff}}(0)\right|$ gets smaller for decreasing lattice spacing. While for $a\sigma_0 = 0.379$ $\epsilon = 1.10$ with $\alpha'/\sigma_0 = 0.72$, one obtains $\epsilon = 0.0$ with $\alpha'/\sigma_0 = 0.0$ for $a\sigma_0 = 0.086$.. This behavior can be explained in the context of the top right phase diagram in Fig. 7.4. With larger lattice spacings the point $\mu/\sigma_0 = 1.035$, $T/\sigma_0 = 0.110$ is in the middle of the triangular region which can be identified as part of an IP. For smaller $a\sigma_0$ these values get closer to the transition to the SP and, finally, the chiral symmetry is restored at this point in the phase diagram. Consequently, the amplitude α' of the inhomogeneous condensate is decreasing and an inhomogeneous $\sigma(x_1)$ gets less favored compared to $\sigma = 0$. This qualitatively supports the result in Ref. [28]. Therein, the author makes a comparable ansatz for the chiral condensate $\sigma = \alpha_{\mathbf{q}} \cos(2\pi \mathbf{q}\mathbf{x}/L)$ with amplitudes $\alpha_{\mathbf{q}}$ for several pairs of wavenumbers $\mathbf{q} = (q_1, q_2)$. The found result for W_1'' qualitatively agrees with Figure 9 of Ref. [28], where the effective action is plotted, for $\mathbf{q} = (3,0)$. Since the lattice spacing $a\sigma_0$ used in this work do not match to Ref. [28], one cannot compare ϵ and α' directly.

In Fig. 7.5 the effective actions for $W_1 = W_1'$ and $W_1 = W_1''$ approach each other in the limit $a \to 0$. In the continuum, both actions describe the $2+1$-dimensional GN model, where the IP is not favored compared to the SP. Depending on the choice of W_1, one can obtain an IP at finite a, which vanishes in the continuum limit. It is worthwhile to note that the wavenumbers $1, 2, 4$ and 5 were also investigated at the same point in the phase diagram. Higher frequencies were never preferred over the shape investigated in Fig. 7.5. However, for $q_1 = 2$ a non-vanishing α' at $a\sigma_0 = 0.237$ was obtained. This could be caused by a shrinking of the inhomogeneous region, while the homogeneous phase transitions gets closer to $\mu/\sigma_0 = 1.0$. Hence, $\mu/\sigma_0 = 1.035$, $T/\sigma_0 \approx 0.11$ is located closer to this boundary, which could cause a lower wavelength to also be preferred compared to $\sigma = 0$ similarly to in the $1+1$-dimensional GN model. When further decreasing the lattice spacing this inhomogeneous modulation is also not favored, but rather a vanishing σ is.

For $W_1(x_1 - y_1) = \delta_{x_1,y_1}$, as was used at an earlier stage in the work of this author's group [27], results qualitatively similar to Figs. 7.4 and 7.5 with $W_1 = W_1''$ were surprisingly obtained, although this discretization does not describe the $2+1$-dimensional GN model but rather a theory with coupling between different flavors and a matrix different than the identity between the fermion bilinear, e.g. $\sim \bar{\psi}\gamma_0\psi\sigma$ (for details see App. A of Ref. [16]

and Ref. [42]). In contrast to the finite N_f investigation of the $1+1$-dimensional GN model in Ref. [16], where the results for this incorrect discretization are qualitatively different from the GN model, a continuum limit similar to Fig. 7.4 is observed. This might be explained by the high bosonic momenta which generate the wrong interaction terms. Since the bosonic field σ only transports high momenta at the phase transition from the IP to the SP at finite a, they might only contribute near the phase transition. The error caused might be comparatively small compared to the finite volume and cutoff effects. The surprising behavior of this wrong discretization is subject of current investigations.

7.2.3 Infinite volume extrapolation for $W_1 = W_1''$

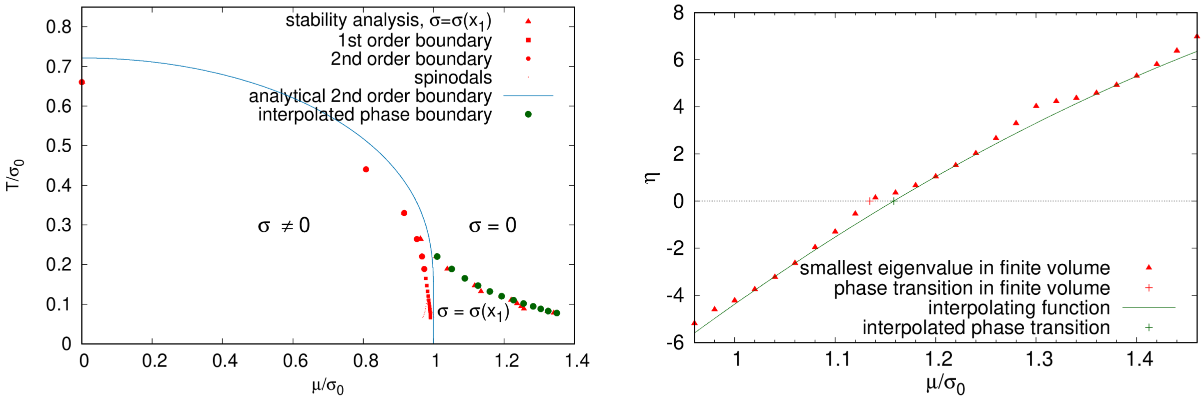

Fig. 7.6: **(left)** The "phase diagram" via stability analysis. The blue line is the result for the homogeneous phase diagram from Ref. [45]. The boundary from stability analyses, denoted with red triangles, on the lattice are the same as from the right panel of Fig. 7.2, i.e. $a\sigma_0 = 0.379$ and $W_1(x_1-y_1) = W_1''(x_1-y_1)$ were used. The green points are obtained through interpolation (from below) of the smallest eigenvalue η of the Hessian matrix as a function of the chemical potential. **(right)** The smallest eigenvalue η of the Hessian matrix as a function of the chemical potential μ for $T/\sigma_0 = 0.132$. The red triangles denote values obtained from lattice data with $a\sigma_0 = 0.379$ in a finite volume $L\sigma_0 = 15.2$. The green line represents a function that interpolates the "valleys" of the lattice data from below to extract the behavior of the phase transition in an infinite volume. The related red and green crosses mark the obtained phase transition with both methods.

In the case of $W_1 = W_1''$ a shrinking of the triangular inhomogeneous region is observed for decreasing lattice spacing and, hence, a vanishing of the IPs in the limit $a \to 0$ is expected. However, it might be of interest that the inhomogeneous phase at finite a is stable when the finite volume is increased. In this section a method to remove finite volume effects on the phase boundary of the $1+1$- and $2+1$-dimensional GN model is discussed. The method will be applied to the $2+1$-dimensional GN model at $a\sigma_0 = 0.379$ and $W_1 = W_1''$ to demonstrate the stability of the IP in an infinite volume investigation.

As obtained in Fig. 7.2 and Fig. 7.1, the line of instability does not correspond to a smooth curve, but rather, it has an oscillatory behavior. This is a finite volume effect, as first observed in a lattice investigation of the $1+1$-dimensional GN model [48]. The finite volume only allows a discrete subset of frequencies to be adopted by the chiral condensate. The frequencies must correspond to a wavelength, which is a natural divider of the lattice extent in the x_1-direction. In the $1+1$-dimensional GN model, the frequency increases continuously in an infinite volume when the chemical potential is increased for fixed temperature. Consequently, in the finite extent of the lattice there are certain values of μ and T, where a frequency which would be preferred in an infinite volume cannot be adopted. This leads to oscillations in the smallest eigenvalue η of the Hessian matrix, as shown in the right panel of Fig. 7.6 for $T = 0.132$ and $d = 2+1$. This assumption, which is shown to be correct in $1+1$ dimensions by [39, 48], is that the finite volume gives peaks in the oscillations of $\eta(\mu)$. At the valleys of the oscillation, in contrast, the preferred wavelength in an infinite volume can be adapted by the chiral condensate in the finite periodic lattice. Therefore, one can fit these valleys in the neighborhood of the root of η from below with a parabola to extract the infinite volume behavior of the smallest eigenvalue. Hence, the original root of η can only be corrected to a larger chemical potential. The resulting line of this procedure is depicted in the right panel of Fig. 7.6. It separates the region where an inhomogeneous chiral condensate lowers the effective action compared to $\sigma = 0$ without finite volume effects on the frequency of the chiral condensate.

Of course, this method can lead to different results depending on the interpolated μ interval and on the interpolating function. With different fit functions and intervals one might get slightly different results, i.e. with the choice in this thesis another error, which is hard to estimate, is introduced. Interpolation with a parabola in a close interval around the root of η, such that three valleys can be identified, has given the best results. This method is, in principle, possible for all lattice spacings plotted in Fig. 7.4. In the case of the $1+1$-dimensional GN model the obtained smooth phase transition in Refs. [39, 48], which is in agreement with the analytical solution [9], proves the applicability of this interpolation. For $d = 2+1$, however, this method gets less precise for small lattice spacings, as the inhomogeneous region gets smaller and the valleys get harder to identify and to interpolate.

7.3 The isospin asymmetric 2+1-dimensional Gross-Neveu model for $\sigma(\mathbf{x}) = \sigma(x_1)$

In this subsection the influence of the "isospin" chemical potential, as introduced in Sec. 3.4, on the existence of an IP is studied. Since in the ordinary GN model an inhomogeneous region is only observed for $W_1 = W_1''$ at finite lattice spacing, the lattice with

$a\sigma_0 = 0.379$ is investigated (compare Fig. 7.2 for results with $\mu_I = 0.0$) with this choice of the weight function. In Fig. 7.7 the resulting phase boundary is shown for a homogeneous chiral condensate, represented by crosses and dashed lines, and the corresponding line of instability, represented by triangles in the μ-T plane for five different μ_I. The phase boundary for a homogeneous chiral condensate is obtained by minimization of the effective action, as explained in Sec. 6.3. These data points are obtained from a bisection algorithm in μ for fixed μ_I. Then, μ_I is varied in discrete steps of $\Delta\mu_I = 0.1$.

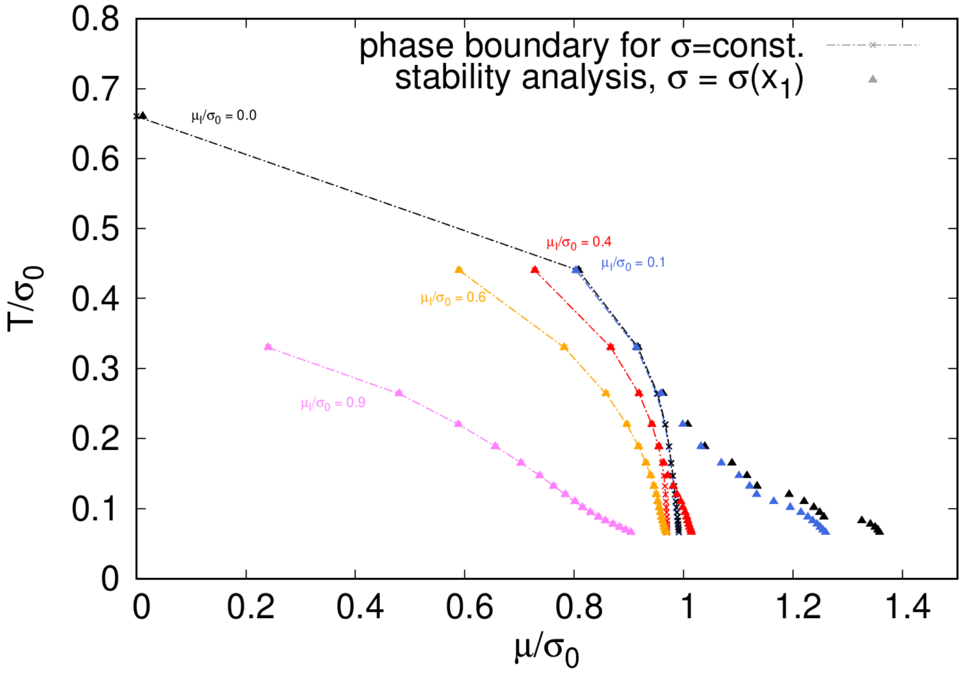

Fig. 7.7: The "phase diagram" of the isospin asymmetric $2+1$-dimensional GN model via stability analysis in the μ-T plane for several different μ_I and for $a\sigma_0 = 0.379$. The crosses, which are connected with a dashed line, represent the phase boundary via minimization of the effective action for $\sigma = \text{const.}$ The triangles represent the line of instability obtained via stability analysis for $\sigma(x_1)$.

For $\mu_I = 0.0$ the result from Sec. 7.2 is reproduced. Note that the obtained phase transition for $\sigma = \text{const.}$ is still relatively far away from the analytical solution [45]. However, this should not prevent a study at finite μ_I, as these cutoff effects are, in principle, under control. In any case, the inhomogeneous region obtained in Sec. 7.2 vanished in the continuum limit. Consequently, whether finite μ_I strongly favors inhomogeneities will be studied. If this is not the case, any IP will likely also be disfavored in the continuum limit. As visualized in Fig. 7.7, for small μ_I one still observe a triangular region, where an inhomogeneous chiral condensate leads to instabilities of the chirally symmetric solution. However, by comparison with the line of instabilities for $\mu_I = 0.1/\sigma_0$ (in blue) with $\mu_I/\sigma_0 = 0.4$ (in red) this region covers a much smaller area in the μ-T plane when increasing the additional chemical potential. More precisely, the LP, where the stability analysis starts to differ from the inhomogeneous calculation, seems to move to lower temperatures. Also the largest value of μ, where an instability is obtained, moves towards lower chemical potentials. For $\mu_I/\sigma_0 = 0.4$ the difference $\delta\mu$ of the line of instability from the homogeneous boundary at the lowest investigated temperature $T/\sigma_0 = 0.066$ is already smaller than $0.04\sigma_0$. At $\mu_I/\sigma_0 = 0.5$, which is not shown since too many points would have overlapped with neighboring data, the line of instability aligns perfectly with the phase boundary for a homogeneous chiral condensate. This can also be observed for $\mu_I/\sigma_0 = 0.6$ and $\mu_I/\sigma_0 = 0.9$, i.e. both lines of instability are - within the errors - in agreement with the homogeneous phase diagram in Sec. 6.3. From this data set it is concluded that the introduction of μ_I disfavors the existence of an IP in the $2+1$-dimensional GN model. Comparing different lattice spacings to get information about the continuum limit does not seem very promising in this study, as a vanishing of the IP is observed for $\mu_I = 0.0$ in the limit $a \to 0$. Since increasing μ_I also disfavors inhomogeneous chiral condensates, a similar result is expected in the continuum limit for finite μ_I. With the investigated volume $L\sigma_0 = 15.2$, the results are already relatively close to the infinite volume results, which is estimated from the $\mu_I = 0.0$ case.

8 Minimization of the effective action

To calculate the phase diagram of the QCD-inspired models in the mean-field approach, one needs to find the global minima of their effective actions for $\sigma = \sigma(\mathbf{x})$. On the lattice this amounts to a multi-dimensional minimization in the variables σ_j, $j = 0, \ldots, N_s^D - 1$. In order to search for these minima for given μ and T, a Fletcher-Reeves conjugate gradient algorithm is used, as found in the GNU Scientific Library [43]. Via this algorithm one can determine local minima. To find a global minimum of the effective action one can provide several starting points for the local minimization algorithm and then compare the resulting minima. Obviously, this procedure does not guarantee to obtain the true global minimum.

In the Fletcher-Reeves conjugate gradient algorithm an initial search direction $p^{(0)}$ is chosen as the gradient $g^{(0)}$ of the effective action at the starting point $\sigma^{(0)}(\mathbf{x}) = \left(\sigma_0^{(0)}, \ldots, \sigma_{N_s^D-1}^{(0)}\right)^{\mathrm{T}}$ in the multi-dimensional space of variables σ_j. The gradient at iteration a is computed via a symmetric finite difference derivative

$$g_j^{(a)} = \frac{1}{\delta}\left(S_{\text{eff}}[\sigma_0^{(a)}, \ldots, \sigma_j^{(a)} + 0.5\delta, \ldots, \sigma_{N_s^D-1}^{(a)}] - S_{\text{eff}}[\sigma_0^{(a)}, \ldots, \sigma_j^{(a)} - 0.5\delta, \ldots, \sigma_{N_s^D-1}^{(a)}]\right) , \tag{8.1}$$

where $\delta = 10^{-5}$. Line minimization is carried out in the search direction $p^{(a)}$ until the functions gradient and the search direction are approximately orthogonal, i.e. line minimization terminates when[19]

$$p^{(a)} g^{(a)} < \chi \left\| p^{(a)} \right\| \left\| g^{(a)} \right\| , \tag{8.2}$$

where $\|.\|$ is the 2-norm on the N_s^D-dimensional vector space. One typically chooses $\chi = 0.1$, as line minimization only needs to be carried out approximately. However, one can also use $\chi = 0.01$ and $\chi = 0.2$ and obtain similar results with different computational cost for the same lattice setup. If condition (8.2) is fulfilled, the search direction is updated using the Fletcher-Reeves formula

$$p^{(a+1)} = g^{(a+1)} + \frac{\left\| g^{(a+1)} \right\|^2}{\left\| g^{(a)} \right\|^2} g^{(a)} , \tag{8.3}$$

where $g^{(b)}$ is the gradient calculated in iteration b. The local minimization algorithm terminates when

$$\left\| g^{(a)} \right\| < \epsilon \tag{8.4}$$

with $\epsilon = 0.01$. It should be noted that with this algorithm one can only identify local minima of the effective action $S_{\text{eff}}[\sigma(\mathbf{x})]$.

---

[19] Here, one does not sum over a.

To find a global minimum for a given chemical potential and temperature, one can rely on several local minimizations with different starting values $\sigma^{(0)}$. Some of these starting points are inspired by eigenvectors corresponding to negative eigenvalues from the stability analysis (compare Sec. 7), but also randomized starting values are used. By comparison with all computed local minima one tries to find the global minimum (global minima) of the effective action.

8.1 The $1+1$-dimensional Gross-Neveu model

The $1+1$-dimensional GN model serves as a test case for the algorithm. Since the aim is to compute the functional shape of the chiral condensates for several fixed conditions of μ and T, the focus of this test is simply to reproduce the characteristic shape of the chiral condensate in the IP. In this sense the test was successful, the identified global minima look similar to the analytical solution [9] as plotted in the right panel of Fig. 5.1 and described in Sec. 5.1. Directly at the phase transition from the HBP to the IP the chiral condensate has a kink-antikink shape, while at larger μ it can be very well parameterized by a cos function. When increasing the chemical potential the frequency of the chiral condensate also increases while its amplitude decreases. This results in a smooth second order transition to the SP. As already discussed in Sec. 7, only a discrete subset of frequencies is allowed in a finite periodic lattice and, consequently, only these wavelengths are observed in the minimization. An important result from this test is that one do not obtain a large amount of inhomogeneous minima but rather only a few different minima for fixed μ and T. Often, these local minima correspond to global minima at slightly larger or smaller chemical potentials. This is a promising observation as it increases the probability of finding global minima.

8.2 The $2+1$-dimensional Gross-Neveu model for $\sigma(\mathbf{x})=\sigma(x_1)$

In the $1+1$-dimensional GN model only a few local minima are observed, which is an indication that one can find a global minimum via multiple local minimization with different starting points. With a restriction to one-dimensional modulations of the chiral condensate $\sigma(\mathbf{x})=\sigma(x_1)$ one can more efficiently compute the effective action (compare Eq. (4.14)). Further, this reduces the space, in which the effective action needs to be minimized, to N_s instead of N_s^2 independent variables σ_j. The number of local minima in this space is probably also reduced. For the $2+1$-dimensional GN model a variety of starting points $\sigma^{(0)}$ for given chemical potential and temperature are used.

With this approach first order transition to inhomogeneous configurations and a larger extension of the inhomogeneous region found via stability analysis or even a second IP, has been extensively sought. Despite the efforts of this thesis work, a different picture of the phase diagram than from stability analysis (see Fig. 7.4) was not obtained. Extensively, the lattice setup with rather larger lattice spacing $a\sigma_0 = 0.379$ was investigated, because the largest inhomogeneous region was obtained here (compare Sec. 7.2) and the numerical cost is rather small. Here, a similar phase diagram as in Fig. 7.2 for both discretizations of the interaction term, i.e. $W_1 = W_1'$ and $W_1 = W_1''$, is obtained. For some μ and T the results are cross-checked for finer lattices with $a\sigma_s 0 = 0.174$ and $a\sigma_0 = 0.237$, but here also additional inhomogeneous regions of the chiral condensate compared to the stability analysis are not obtained. Therefore, another phase diagram is not presented, rather interesting effects that can be only obtained in a minimization are described.

8.2.1 Local inhomogeneous minima within the homogeneous broken phase

Within the HBP, as depicted for $a\sigma_0 = 0.379$ via the red dots in Fig. 6.4, several inhomogeneous local minima of $S_{\text{eff}}[\sigma(x_1)]$ are obtained. Deep within the HBP[20] those minima show a similar functional form as the analytical solution of the 1+1-dimensional GN model (compare Fig. 5.1). In Fig. 8.1 one local minimum $\Sigma(x_1)$ of the effective action at $\mu/\sigma_0 = 0.6$ and $T/\sigma_0 = 0.176$ is presented, which is obtained at $a\sigma_0 = 0.237$. For the given chemical potential and temperature the relative difference of the action evaluated at $\Sigma(x_1)$ to the action at the homogeneous, global minimum σ is around[21] 10^{-5}. For $a\sigma_0 = 0.379$ the line of instability together with the homogeneous calculations in Fig. 7.2 seem to represent the phase diagram of the lattice theory. For $W_1 = W_1''$ this means that the observed triangular inhomogeneous region is an IP, which is connected by phase transitions to the HBP and the IP. The line of instability, represented by triangles, is equivalent to a true second order transition to the SP. Within the errors, which are introduced in the Fletcher-Reeves algorithm (e.g. in Eq. (8.4)) and due to the number of investigated points in the μ-T plane, the red squares in Fig. 7.2 correspond to a transition from the HBP to the IP. In the discretization $W_1 = W_1''$ a shrinking of this relative difference is observed when increasing the chemical potential towards the phase transitions at μ', which is obtained for homogeneous σ, as described in Sec. 6.2. This has been shown via several local minimizations at μ' and slightly lower and larger values than μ'. Around μ' two (within the errors discussed above) degenerate global minima of the effective action are obtained. One is an inhomogeneous shape with two kinks, similar to the left panel of Fig. 8.2, the other is a homogeneous minimum. In contrast, for $W_1 = W_1''$ only inhomogeneous modulations deep within the HBP are observed, e.g. for $T = 0.176$ one requires $\mu/\sigma_0 < 0.8$ to obtain inhomogeneous local minima.

---

[20] This should suggest that the given chemical potential and temperature is relatively far away from the homogeneous phase boundary. For larger μ and T results depend on the chosen weight function for the interaction term.

[21] The value of the relative difference depends on the choice of $W_1(x_1 - y_1)$. However, for the chosen μ and T, the calculated relative difference is of the same order for both presented choices. In general this is not the case.

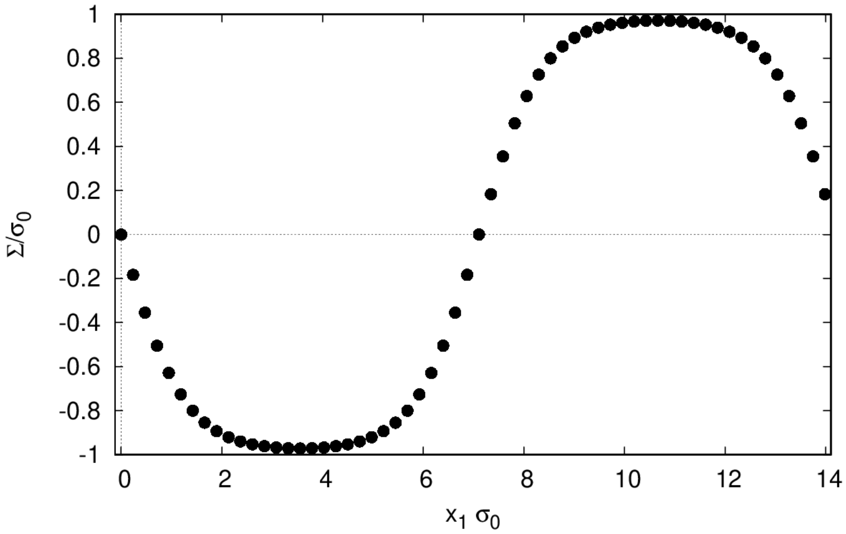

Fig. 8.1: Local minimum Σ of the effective action $S_{\text{eff}}[\sigma(x_1)]$ at $\mu/\sigma_0 = 0.6$, $T/\sigma_0 = 0.176$, i.e. within the HBP. The minimum is obtained via local minimization on the lattice for $a\sigma_0 = 0.237$. Similar functional forms of the chiral condensate are obtained for both weight functions $W(x_1-y_1) = W_1'(x_1-y_1)$ and $W(x_1 - y_1) = W_1''(x_1 - y_1)$. One finds $|(S_{\text{eff}}[\Sigma(x_1)] - S_{\text{eff}}[\sigma])/S_{\text{eff}}[\sigma]| \approx 10^{-5}$, where $\sigma = \text{const.} \neq 0$ is the global minimum for the given μ and T.

Several minimizations indicate that a decrease of the temperature at fixed μ reduces the relative difference of the effective action for inhomogeneous modulations, such as $\Sigma(x_1)$, compared to the global minimum. This supports an analysis from Ref. [37], where the analytical solution from the $1+1$-dimensional GN model [9] has been used as a one-dimensional ansatz for the chiral condensate at $T = 0$ and with finite baryon densities. In this work, two parameters in this ansatz with Jacobi elliptic functions are minimized for a given baryon density. The author finds a degenerate phase, where such an inhomogeneous modulation has the same minimizing energy density as the homogeneous minimum of the effective action. Obviously, $T = 0$ cannot be investigated in this study due to the infinite extent of the temporal direction. However, an investigation of the limit $T \to 0$ is possible. When lowering the temperature at fixed chemical potential, a shrinking of the relative difference $\theta = |(S_{\text{eff}}[\varsigma(x_1)] - S_{\text{eff}}[\sigma])/S_{\text{eff}}[\sigma]|$ is observed, where $\sigma = \text{const.} \neq 0$ is the global minimum and $\varsigma(x_1)$ is an inhomogeneous local minimum corresponding to the second smallest value of the effective action. For the lattice $a\sigma_0 = 0.237$ with $W_1 = W_1'$ as weight function for the interaction term this behavior will explicitly be studied. At $\mu/\sigma_0 = 0.6$ and $T/\sigma_0 = 0.263$ an inhomogeneous kink-antikink minimum with $\theta \approx 5.7 \cdot 10^{-4}$ is found. By fixing the chemical potential and decreasing the temperature to $T/\sigma_0 = 0.176$ the modulation $\Sigma(x_1)$, as plotted in Fig. 8.1, $\theta \approx 3.8 \cdot 10^{-4}$ is obtained. By further decreasing the temperature to $T/\sigma_0 \approx 0.117$ one finds $\theta \approx 3.0 \cdot 10^{-4}$. However, a clear functional behavior $\theta(T)$ cannot be found. Nevertheless, a decrease in $\theta(T)$ for $T \to 0$

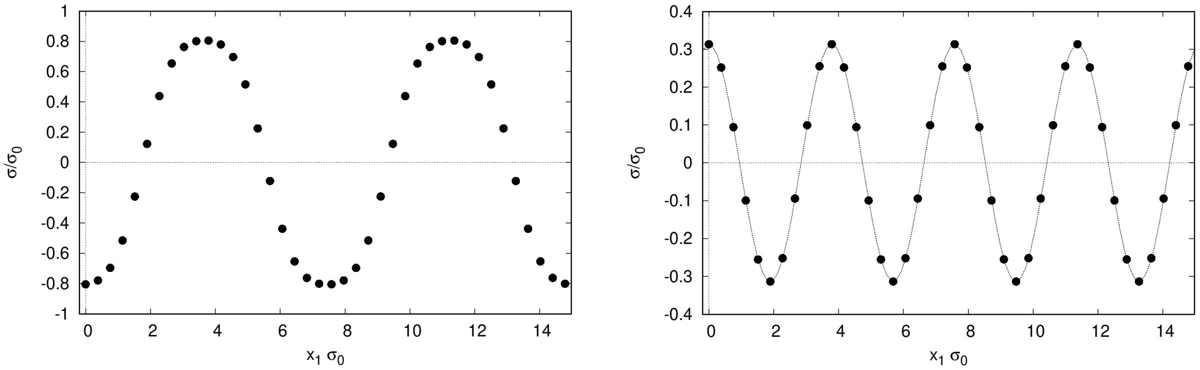

Fig. 8.2: Global minima of the effective action obtained by performing multiple local minimizations on the lattice with $a\sigma_0 = 0.379$ and $W_1(x_1 - y_1) = W_1''(x_1 - y_1)$ for $T/\sigma_0 = 0.132$. **(left)** $\mu/\sigma_0 = 0.97$. **(right)** $\mu/\sigma_0 = 1.11$. The dashed line is a cos-function with the same frequency as the minimum.

is observed for several different chemical potentials. Together with the analytical study [37] one can conclude that for $T = 0$ there exists an degenerate ground state with an homogeneous and an inhomogeneous minimum. One cannot clearly observe whether such an degenerate phase exists also for finite, but rather small $T/\sigma_0 < 0.1$, since the relative difference θ gets so small that the errors of the minimization, e.g. caused by the terminating condition Eq. (8.4), are of the order of θ. Consequently, for low temperatures the need for more and more precise minimizations and the increasing temporal extent prevent a more sophisticated study within lattice field theory. Nevertheless, a study of the whole phase diagram with the ansatz from the $1+1$-dimensional GN model in one spatial direction might lead to an IP degenerate to the HBP also at finite temperature.

8.2.2 Global minima within the inhomogeneous phase at finite a for $W_1 = W_1''$

For $W_1 = W_1''$ an IP is observed via stability analysis at finite lattice spacing (see Sec. 7.2), which vanishes when applying the continuum limit. Via minimization one does not obtain an extension of this IP nor a second phase with inhomogeneous chiral condensates, which could possibly survive the continuum limit. However, the energetically preferred functional form of the chiral condensate in the IP. Therefore, one should prefer to minimize the effective action at rather large $a\sigma_0 = 0.379$, where the IP still covers a quite large region in the μ-T plane. Surprisingly, the chiral condensate seems to behave as in $1+1$ dimensions. The two resulting global minima are plotted in Fig. 8.2. At the phase transition from the HBP an inhomogeneous chiral condensate with two kinks, as plotted in the left panel of Fig. 8.2 for $T/\sigma_0 = 0.132$ and $\mu/\sigma_0 = 0.97$, is observed. The chiral condensate still has plateaus around its maxima and minima, albeit they are already rather small. The amplitude of approximately $0.8\sigma_0$ is still quite large. When slightly increasing the chemical potential, the chiral condensate continuously changes towards a cos-like behavior. The chiral condensate at larger μ responds as in the $1+1$-dimensional

GN model. The frequency of the cos-waves increases in discrete steps due to the finite spatial extent, while the amplitude of σ decreases until it vanishes in a smooth second order transition to the SP. The right panel of Fig. 8.2 shows the chiral condensate at $\mu/\sigma_0 = 1.11$, i.e. slightly before the phase transition at $\mu'/\sigma_0 = 1.134$. The wavelength of the condensate is now $L/4$, while the amplitude is around $0.31\sigma_0$.

8.3 The isospin asymmetric 2+1-dimensional Gross-Neveu model

In principle, a minimization for non-vanishing μ_I might lead to different results than the stability analysis in Sec. 7.3. However, similar results as for the $2+1$-dimensional GN model are expected. Since increasing the isospin-like chemical potential disfavors the existence of inhomogeneous chiral condensates in the stability analysis and a minimization of the effective action in the previous subsection does not exhibit a larger IP, a dedicated investigation of the phase diagram for various μ_I is not very promising. An interesting topic, which will be investigated in the future, is whether a degenerate, inhomogeneous ground state remains at finite μ_I for $T \to 0$.

9 Conclusion

In this thesis the possible existence of IPs in the $2+1$-dimensional GN model was investigated in the large-N_f limit. Moreover, an additional isospin-like chemical potential μ_I was introduced and, in a novel study, IPs for different μ_I were investigated. Therefore, two different possibilities were proposed to naively discretize the GN model and the numerical methods of this thesis were tested on the $1+1$-dimensional GN model. A stability analysis and a local minimization algorithm on the lattice for $\sigma(\mathbf{x}) = \sigma(x_1)$ was applied to study the phase diagram of these models.

In the $2+1$-dimensional GN model an IP is found via stability analysis at finite lattice spacing in only one of the two applied naive discretizations of the interaction term (W_1' or W_1''). The IP strongly depends on the cutoff and vanishes in the continuum limit confirming the lattice study in Ref. [28]. A similar effect is observed in a complementary continuum mean-field study [29], where at finite cutoff an IP occurs, that vanishes when the cutoff is removed. Through minimization of the effective action, additional inhomogeneous regions in the μ-T plane were not obtained compared to the stability analysis. However, indications for a degenerate ground state at $T=0$, where an inhomogeneous together with a translationally invariant chiral condensate are global minima of the effective action, supporting the analysis in [37] are found. The influence of the introduced isospin-like chemical potential disfavors the existence of IPs. This has been studied via a stability analysis at relatively large lattice spacing in the discretization, which favored the IP at finite lattice spacing for vanishing μ_I. Although, at relatively low $\mu_I/\sigma_0 < 0.5$ the IP persists but shrinks, and vanishes completely for larger μ_I. However, all of these results are obtained for one-dimensional modulation of the chiral condensate $\sigma(\mathbf{x}) = \sigma(x_1)$. Due to Ref. [29] the stability analysis should not give different results in the continuum limit for higher-dimensional modulations, the phase diagram of both models could change for a full minimization of the effective action. A full minimization of the effective action for $\sigma = \sigma(\mathbf{x})$, possibly also with other minimization algorithms, is an interesting prospect for future investigations.

Recently, the existence of oscillating chiral condensates has been confirmed in the $1+1$-dimensional GN model at finite N_f, i.e. including quantum fluctuations. Hence, the large-N_f limit, or equivalently the mean-field approximation, seems to retain important information about the full QFT, which motivates further studies in the mean-field approach. In $1+1$-dimensions the phase diagram of the isoNJL model for multiple chemical potentials has been studied [12, 13], where several complex functional forms of scalar and pseudo-scalar modes are obtained. These results further motivate the need for global minimization of effective actions without a specific ansatz for the chiral condensate, as it is possible within lattice field theory. The findings in this thesis raise open questions about the role of a cutoff relating to the existence of IPs, which this author will continue to study in $2+1$ dimensions. Since certain QCD-inspired models in $3+1$ dimensions require a cutoff, while QCD is renormalizable, such an investigation could clarify concerns regarding the validity of their results as models for strongly-interacting matter. A straightforward candidate for such a study could be the $2+1$-dimensional NJL model, which features a continuous chiral symmetry.

A long-term aim is a very efficient reimplementation of the developed lattice techniques to investigate a variety of QCD-inspired models in a flexible numerical framework. This would allow the study of higher-dimensional modulations of the chiral condensate in efficient minimizations of the corresponding actions. Two $3+1$-dimensional models, that are much closer to QCD, are the NJL and the Quark-Meson model. IPs have so far been mostly investigated via certain ansatzes for the chiral condensate [14, 15], e.g. with a chiral density wave. A minimization of the effective action would, therefore, provide the energetically preferred functional form of the condensate without an ansatz and, possibly, an extension of the found IP or even the appearance of a disconnected, second IP. These investigations can then straightforwardly be extended to explore the parameter space, e.g the dependence of IPs on an isospin chemical potential or the inclusion of strange quarks (as in Ref. [49]).

Appendix

A Properties of S_{eff}

In order to perform lattice calculations of the GN model it is important to ensure that the effection action (3.10) is real. As we introduced the bosonic field σ as a real field, we only need to show that the determinant of the Dirac operator Q is real valued. In $1+1$ dimension the proof is rather straight forward. In $2+1$ dimensions, however, we need to restrict the chiral condensate to spatial coordinates to obtain a real action in the irreducible representations. In the respective sections, we will not denote the dimensionality of spinor space. To keep notation simple, Q denotes the Dirac operator in context of the respective Euclidean spacetime dimensions and fermion representation.

A.1 $1+1$ dimensions

The calculation in this section is valid for an irreducible fermion representation. The bosonic field σ can depend on both coordinates, i.e. $\sigma(x_0, x_1)$.

Proof of $\det \mathrm{Q}[-\sigma] = \det \mathrm{Q}[+\sigma]$

We start with the eigenvalue equation of the Dirac operator Q in irreducible fermion representation

$$\mathrm{Q}[+\sigma] f_j = (+\gamma_\nu \partial_\nu + \gamma_0 \mu + \sigma)\, f_j(x_0, x_1, x_2) = \alpha_j f_j(x_0, x_1, x_2)\,. \tag{A.1}$$

In $1+1$ dimension we can always define the hermitian chirality operator γ_5[22]. Applying $-\gamma_5$ from the left and inserting $\gamma_5^2 = \mathbb{1}_2$ leads to

$$\underbrace{(\gamma_\nu \partial_\nu + \gamma_0 \mu - \sigma)}_{=\mathrm{Q}[-\sigma]} \gamma_5 f_j(x_0, x_1, x_2) = -\alpha_j \gamma_5 f_j(x_0, x_1, x_2)\,. \tag{A.2}$$

Thus, if α_j is an eigenvalue of $\mathrm{Q}^T[+\sigma]$, $-\alpha_j$ is an eigenvalue of $\mathrm{Q}[-\sigma]$. Consequently,

$$\det \mathrm{Q}[-\sigma] = \prod_j (-\alpha_j) = \prod_j \alpha_j = \det \mathrm{Q}[+\sigma]\,, \tag{A.3}$$

where we have used that the number of eigenvalues is even. Note that Eq. (A.3) implies

$$S_{\text{eff}}[-\sigma] = S_{\text{eff}}[+\sigma]\,. \tag{A.4}$$

Proof of $\det \mathrm{Q} \in \mathbb{R}$

---

[22] This is possible, because the γ matrices can always be chosen to be proportional to the Pauli matrices.

Complex conjugation of Eq. (A.1) leads to

$$\left(+\gamma_0^* \left(\partial_0 + \mu\right) + \gamma_1^* \partial_1 + \sigma\right) f_j^*(x_0, x_1, x_2) = \alpha_j^* f_j^*(x_0, x_1, x_2) \,. \tag{A.5}$$

In $1+1$ dimension there exist two charge conjugation matrices $C_\pm$ that fulfill (compare e.g. Ref. [50])

$$C_- \gamma_\mu C_-^{-1} = -\gamma_\mu^T \,, \tag{A.6}$$
$$C_+ \gamma_\mu C_+^{-1} = +\gamma_\mu^T \,. \tag{A.7}$$

Applying C_+ from the left and inserting $\mathbb{1}_2 = C_+^{-1} C_+$ results in

$$\left(+\gamma_0^\dagger \left(\partial_0 + \mu\right) + \gamma_1^\dagger \partial_1 + \sigma\right) C_+ f_j^*(x_0, x_1, x_2) = \alpha_j^* C_+ f_j^*(x_0, x_1, x_2) \,. \tag{A.8}$$

In general, the Euclidean γ_μ in $1+1$ dimensions are hermitian. Thus, we identify

$$\underbrace{\left(+\gamma_0 \left(\partial_0 + \mu\right) + \gamma_1 \partial_1 + \sigma\right)}_{=\mathrm{Q}[+\sigma]} C_+ f_j^*(x_0, x_1, x_2) = \alpha_j^* C_+ f_j^*(x_0, x_1, x_2) \,. \tag{A.9}$$

Consequently, if α_j is an eigenvalue of Q, also α_j^* is an eigenvalue of Q. We conclude

$$\det \mathrm{Q} = \prod_k \alpha_k^* \alpha_k = \prod_k |\alpha_k| \,, \tag{A.10}$$

i.e. we can express the determinant $\det \mathrm{Q}$ as a product over absolute values of the complex α_j. It follows that

$$\det \mathrm{Q} \in \mathbb{R} \,. \tag{A.11}$$

A.2 $2+1$ dimension

The calculations in this appendix are valid for the 2×2 fermion representations (3.20) and (3.21) and for the 4×4 fermion representation (3.24). Note that we restrict the dependence of σ to the spatial coordinates, i.e. $\sigma = \sigma(x_1, x_2)$.

Proof of $\det \mathrm{Q}[-\sigma] = \det \mathrm{Q}[+\sigma]$

We start with the eigenvalue equation for Q^T,

$$\mathrm{Q}^T[+\sigma] f_j = \Big(+ \gamma_0 \partial_0 - \gamma_0 \mu - \gamma_1 \partial_1 - \gamma_2 \partial_2 + \sigma(x_1, x_2)\Big) f_j(x_0, x_1, x_2) = \alpha_j f_j(x_0, x_1, x_2) \,, \tag{A.12}$$

where we have used $\partial_\mu^T = -\partial_\mu$. The coordinate transformation $u = -x_0$ leads to

$$\underbrace{\Big(\gamma_0\partial_0 + \gamma_0\mu + \gamma_1\partial_1 + \gamma_2\partial_2 - \sigma(x_1, x_2)\Big)}_{=\mathrm{Q}[-\sigma]} f_j(-u, x_1, x_2) = -\alpha_j f_j(-u, x_1, x_2)\,. \tag{A.13}$$

Thus, if α_j is an eigenvalue of $\mathrm{Q}^T[+\sigma]$, $-\alpha_j$ is an eigenvalue of $\mathrm{Q}[-\sigma]$. Consequently,

$$\det \mathrm{Q}[-\sigma] = \prod_j(-\alpha_j) = \prod_j \alpha_j = \det \mathrm{Q}^T[+\sigma] = \det \mathrm{Q}[+\sigma]\,, \tag{A.14}$$

where we have used that the number of eigenvalues is even. Note that Eq. (A.14) implies

$$S_{\text{eff}}[-\sigma] = S_{\text{eff}}[+\sigma]\,. \tag{A.15}$$

Proof of $\det \mathrm{Q} \in \mathbb{R}$

We start with the eigenvalue equation for Q,

$$\mathrm{Q}[+\sigma] f_j = \Big(+\gamma_0\partial_0 + \gamma_0\mu + \gamma_1\partial_1 + \gamma_2\partial_2 + \sigma(x_1, x_2)\Big) f_j(x_0, x_1, x_2) = \alpha_j f_j(x_0, x_1, x_2)\,. \tag{A.16}$$

Complex conjugation leads to

$$\Big(-\gamma_0\partial_0 - \gamma_0\mu + \gamma_1\partial_1 + \gamma_2\partial_2 + \sigma(x_1, x_2)\Big) f_j^*(x_0, x_1, x_2) = \alpha_j^* f_j^*(x_0, x_1, x_2) \tag{A.17}$$

and multiplication of this equation with $-\gamma_0$ to

$$\underbrace{\Big(+\gamma_0\partial_0 + \gamma_0\mu + \gamma_1\partial_1 + \gamma_2\partial_2 - \sigma(x_1, x_2)\Big)}_{=Q[-\sigma]} \gamma_0 f_j^*(x_0, x_1, x_2) = -\alpha_j^*\gamma_0 f_j^*(x_0, x_1, x_2)\,. \tag{A.18}$$

Thus, if α_j is an eigenvalue of $\mathrm{Q}[+\sigma]$, $-\alpha_j^*$ is an eigenvalue of $\mathrm{Q}[-\sigma]$. Consequently,

$$\Big(\det \mathrm{Q}[-\sigma]\Big)^* = \Big(\prod_j(-\alpha_j^*)\Big)^* = \prod_j \alpha_j = \det \mathrm{Q}[+\sigma]\,, \tag{A.19}$$

where we have again used that the number of eigenvalues is even. Combining Eq. (A.14) and Eq. (A.19) leads to

$$\Big(\det \mathrm{Q}[+\sigma]\Big)^* = \det \mathrm{Q}[+\sigma]\,, \tag{A.20}$$

i.e. $\det \mathrm{Q} \in \mathbb{R}$.

B Poincaré symmetry

In this appendix we will present the Poincaré group in $1+1$- and $2+1$-dimensions and its Rep. for bosonic (spin 0) and fermionic (spin $\frac{1}{2}$) field. Therefore, we neglect flavor rotations and only concentrate on the Poincaré symmetry of one single flavor ψ. Poincaré transformations are a combination of Lorentz transformations and spacetime translations. We only consider proper Lorentz transformations and discuss discrete spacetime symmetries separately[23]. At first, we discuss general properties of Poincaré transformations in d dimensions.

In general, we define a Poincaré transformation by its application on spacetime vectors, i.e.

$$x' = T(\Lambda, a)x = \Lambda x + a\,. \tag{B.1}$$

for spacetime vector $a = (a_0, \dots, a_{d-1})^{\mathrm{T}}$. The Lorentz transformation Λ is element of $\mathrm{SO}(d)$. An infinitesimal Lorentz transformation is given by

$$\Lambda_{\mu\nu} = \delta_{\mu\nu} + \epsilon_{\mu\nu} \tag{B.2}$$

with arbitrary small parameters $\epsilon_{\mu\nu} = -\epsilon_{\nu\mu}$.

Now we consider Reps. $U(\Lambda, a)$ of the Poincaré group on other vector spaces. They inherit the group structure from the $T(\Lambda, a)$. The elements $U(\Lambda, a)$ can be written as

$$U(\Lambda, a) = \mathrm{e}^{-\frac{\mathrm{i}}{2}\epsilon_{\mu\nu}M_{\mu\nu}}\mathrm{e}^{-\mathrm{i}a_\mu P_\mu} = \mathbb{1} - \frac{\mathrm{i}}{2}\epsilon_{\mu\nu}M_{\mu\nu} - \mathrm{i}a_\mu P_\mu + \dots\,, \tag{B.3}$$

where $M_{\mu\nu}$ denote the anti-symmetric generators for Lorentz transformations. These are rotations in Euclidean spacetime. P_μ denote the generators for translations and a_μ is the parameter for the translation. $M_{\mu\nu}$ and P_μ form a Lie algebra, the Poincaré algebra, whose commutation relations are given by

$$[M_{\alpha\beta},\, M_{\gamma\delta}] = \mathrm{i}\,(\delta_{\beta\gamma}M_{\alpha\delta} + \delta_{\alpha\delta}M_{\beta\gamma} - \delta_{\alpha\gamma}M_{\beta\delta} - \delta_{\beta\delta}M_{\alpha\gamma})\,, \tag{B.4a}$$

$$[P_\alpha,\, P_\beta] = 0\,, \tag{B.4b}$$

$$[P_\alpha,\, M_{\beta\gamma}] = \mathrm{i}\,(\delta_{\alpha\beta}P_\gamma - \delta_{\alpha\gamma}P_\beta)\,. \tag{B.4c}$$

The generators are[24]

$$M_{\mu\nu} = \mathrm{i}\,(x_\mu\partial_\nu - x_\nu\partial_\mu) + S_{\mu\nu}\,, \quad P_\mu = -\mathrm{i}\partial_\mu\,, \tag{B.5}$$

---

[23] In Euclidean spacetime it is possibly to define the Lorentz transformations as a product of proper transformations, i.e. with determinant 1, and a discrete $\mathbb{Z}_2$-symmetry. This discrete symmetry can e.g. be chosen as parity or time reversal.

[24] The generators are chosen such that we obtain transformation on scalar and fermionic fields. One can also obtain the spacetime transformation (B.1). Then each of the $M_{\mu\nu}$ has a matrix structure in spacetime.

where $S_{\mu\nu}$ is a spin structure that vanishes for scalar fields (spin 0). In general, it fulfills $S_{\mu\nu} = -S_{\nu\mu}$.

Accordingly, a scalar field ϕ transforms under Lorentz transformations as

$$\phi'(x') = U(\Lambda, 0)\phi(\Lambda x) = \mathrm{e}^{-\frac{\mathrm{i}}{2}\epsilon_{\mu\nu}M_{\mu\nu}}\phi(\Lambda x). \tag{B.6}$$

Considering only infinitesimal transformation, we can expand this expression and neglect $O(\epsilon^2)$ corrections to obtain

$$\begin{aligned}\phi'(x') &= \left(1 - \frac{\mathrm{i}}{2}\epsilon_{\mu\nu}M_{\mu\nu}\right)\left[\phi(x) + \epsilon_{\mu\nu}x_\nu\partial_\mu\phi(x)\right] \\ &= \phi(x) + \frac{1}{2}\epsilon_{\mu\nu}\left(x_\mu\partial_\nu - x_\nu\partial_\mu\right)\phi(x) + \epsilon_{\mu\nu}x_\nu\partial_\mu\phi(x) = \phi(x),\end{aligned} \tag{B.7}$$

where in the last step we use the anti-symmetry of the parameters $\epsilon_{\mu\nu}$ and relabel the summation indices. As we can express general Lorentz transformations via infinitesimal transformations, we obtain the expected invariance of scalar fields[25]. One can perform the same calculation for translations $U(\mathbb{1}, a)$ and obtain

$$\phi'(x') = \phi'(x + a) = \phi(x). \tag{B.8}$$

Fermion fields (spin $\frac{1}{2}$) transform under Poincaré transformations as

$$\psi'(x') = U(\Lambda, 0)\psi(\Lambda x) = \mathrm{e}^{-\frac{\mathrm{i}}{2}\epsilon_{\mu\nu}S_{\mu\nu}}\psi(x) \tag{B.9}$$

with parameters $\omega_{\mu\nu} = -\omega_{\nu\mu}$. Here, in the last step we already used the transformation behavior (B.7). The generators $S_{\mu\nu}$ are constructed with Reps. of the Dirac algebra (3.12)

$$S_{\mu\nu} = \frac{\mathrm{i}}{4}\left[\gamma_\mu, \gamma_\nu\right] . \tag{B.10}$$

In general, the spinor transformations U are constructed such that they fulfill the identity

$$U^{-1}(\Lambda)\gamma_\mu U(\Lambda) = \Lambda_{\mu\nu}\gamma_\nu \, , \tag{B.11}$$

which can be shown by considering infinitesimal transformations.

---

[25] Note that besides the additional spin structure $S_{\mu\nu}$ this transformation behavior also holds for higher spin fields. Since we just showed the invariance under the scalar part of the transformation, we will directly apply this behavior for higher spin fields as a convention. Rather, we focus on the spin structure of the generators.

B.1 $1+1$ dimensions

The Lorentz transformation Λ is an element of SO(2). SO(2) is a lie group and its elements O can be expressed by

$$O = \mathrm{e}^{i\theta\sigma_2} = \cos(\theta)\mathbb{1}_2 + \mathrm{i}\sin(\theta)\tau_2 \,, \tag{B.12}$$

where τ_2 is the second Pauli matrix and θ is a real parameter. Hence, the group elements are connected continuously and can be represented by iterative application of infinitesimal transformations.

In $1+1$ dimensions an irreducible Rep. of the Dirac algebra is given by (3.13). Hence, we only have one independent generator $S_{01} = -\frac{\tau_3}{2}$. The transformation behavior of fermion fields (B.9) can be explicitly written as

$$\psi'(x') = \mathrm{e}^{\frac{\mathrm{i}}{2}\epsilon_{01}\tau_3}\psi(x). \tag{B.13}$$

With parameter $\epsilon = \epsilon_{01}$ the transformation matrix is given by

$$\mathrm{e}^{\frac{\mathrm{i}}{2}\epsilon\tau_3} = \begin{pmatrix} \mathrm{e}^{\frac{\mathrm{i}\epsilon}{2}} & 0 \\ 0 & \mathrm{e}^{-\frac{\mathrm{i}\epsilon}{2}} \end{pmatrix} , \tag{B.14}$$

which is just a rotation of the components of ψ.

Discrete symmetries

For completeness, we additionally mention improper discrete symmetries. The parity inversion P is defined by

$$(x_0, x_1)^{\mathrm{T}} \to (x_0, -x_1)^{\mathrm{T}} \,,\ \psi(x) \to \gamma_0\psi(x) \,,\ \bar{\psi}(x) \to \bar{\psi}(x)\gamma_0 \,. \tag{B.15}$$

From this we can conclude that $\bar{\psi}\psi$ is a scalar, while a term $\bar{\psi}\gamma_5\psi$ is pseudoscalar, i.e. it is multiplied by -1 under P. Time reversal is then equivalent to the application of (B.14) with the angle π and P, which is element of the Lorentz group (see Eq. (B.12)). Explicitly, time reversal is given by

$$(x_0, x_1)^{\mathrm{T}} \to (-x_0, x_1)^{\mathrm{T}} \,,\ \psi(x) \to \gamma_1\psi(x) \,,\ \bar{\psi}(x) \to \bar{\psi}(x)\gamma_1 \,. \tag{B.16}$$

B.2 $2+1$ dimensions

In $2+1$ dimensions the Lorentz transformation Λ is element of SO(3). Elements $R \in$ SO(3) can be expressed by

$$R = \mathrm{e}^{\mathrm{i}\theta_j T_j} \tag{B.17}$$

with three parameters θ_j and generators

$$T_0 = \mathrm{i}\begin{pmatrix} 0 & 0 & 0 \\ 0 & 0 & -1 \\ 0 & +1 & 0 \end{pmatrix}, T_1 = \mathrm{i}\begin{pmatrix} 0 & 0 & 1 \\ 0 & 0 & 0 \\ -1 & 0 & 0 \end{pmatrix}, T_2 = \mathrm{i}\begin{pmatrix} 0 & -1 & 0 \\ +1 & 0 & 0 \\ 0 & 0 & 0 \end{pmatrix}. \tag{B.18}$$

The commutation relation between the generators are

$$[T_i, T_j] = \mathrm{i}\epsilon_{ijk} T_k \tag{B.19}$$

with the three-dimensional Levi-Civita symbol. From this property of the generators one can directly see that elements of SO(3) are rotations on a three-dimensional vector space, since Eq. (B.19) is the commutation relation of orbital angular momentum operators.

One can obtain the same relation by considering general Reps. $U(\Lambda, a)$, as defined in Eq. (B.3). We have now three independent generators for Lorentz transformations $M_{\mu\nu}$ and three generators for spacetime translations P_μ. One can unambiguously map the matrix-valued $M_{\mu\nu}$ to vectors

$$L_\alpha = -\frac{\epsilon_{\alpha\beta\gamma}}{2} M_{\beta\gamma} \quad \leftrightarrow \quad M_{\alpha\beta} = -\epsilon_{\alpha\beta\gamma} L_\gamma \,. \tag{B.20}$$

The Poincaré algebra (B.4) translates to

$$[L_\mu, L_\nu] = \mathrm{i}\epsilon_{\mu\nu\rho} L_\rho \,, \tag{B.21a}$$
$$[P_\mu, L_\nu] = \mathrm{i}\epsilon_{\mu\nu\rho} P_\rho \,, \tag{B.21b}$$
$$[P_\mu, P_\nu] = 0 \,, \tag{B.21c}$$

i.e. the generators of Lorentz transformations L_α fulfill the algebra of angular momentum operators.

Fermion fields transform as

$$\psi'(x') = \mathrm{e}^{-\frac{\mathrm{i}}{2}\epsilon_{\mu\nu} S_{\mu\nu}} \psi(x) \tag{B.22}$$

where we now have three independent generators

$$S_{\mu\nu} = \frac{\mathrm{i}}{4}\left[\gamma_\mu, \gamma_\nu\right] \,. \tag{B.23}$$

As the $S_{\mu\nu}$ depend on the Rep. of the Dirac algebra (3.12), the transformation behavior of spinors will differ between irreducible representations, such as (3.20) and (3.21), and reducible ones, such as (3.24).

2-component fermion representations

In the irreducible, 2×2 Reps. (3.20) and (3.21) the generators $S_{\mu\nu}$ are given by

$$S_{01} = -\frac{\tau_1}{2}\,, \quad S_{02} = \frac{\tau_3}{2}\,, \quad S_{12} = -\frac{\tau_2}{2}\,. \tag{B.24}$$

They fulfill the algebra of SU(2). Note that the algebra of SU(2) and SO(3) are equivalent and given by (B.19). Consequently, the matrices

$$U = \mathrm{e}^{-\frac{\mathrm{i}}{2}\epsilon_{\mu\nu}S_{\mu\nu}} = e^{\frac{\mathrm{i}}{2}\varepsilon\tau} \tag{B.25}$$

are elements of SU(2). We define $\varepsilon = (\epsilon_{01}, \epsilon_{12}, -\epsilon_{02})^{\mathrm{T}}$ and $\tau = (\tau_1, \tau_2, \tau_3)^{\mathrm{T}}$ in the last step to choose a standard basis of SU(2) generators.

As well known (see e.g. Ref. [51]), SU(2) is a double cover of SO(3), which is equivalent to the Lorentz group. This can be demonstrated via comparison of transformations (B.25) and (B.17) for rotations around the x_1 axis ($\theta_0 = 0, \theta_2 = 0$ and $\varepsilon_0 = 0, \varepsilon_2 = 0$). Considering a rotation of 2π in Euclidean spacetime we have for a spacetime vector a and a spinor ψ

$$a'(x') = \mathrm{e}^{\mathrm{i}2\pi T_2} a(x) = \begin{pmatrix} +\cos(2\pi) & 0 & -\sin(2\pi) \\ 0 & 1 & 0 \\ +\sin(2\pi) & 0 & +\cos(2\pi) \end{pmatrix} a(x) = a(x) \tag{B.26a}$$

$$\psi'(x') = \mathrm{e}^{\frac{\mathrm{i}}{2}2\pi\tau_2}\psi(x) = \begin{pmatrix} +\cos(\pi) & +\sin(\pi) \\ -\sin(\pi) & +\cos(\pi) \end{pmatrix} \psi(x) = -\psi(x)\,. \tag{B.26b}$$

Thus, after a full rotation around the x_1-axis the spinor is not mapped to itself. However, as one can easily see from the above calculation, performing a rotation with angle 4π results in $\psi'(x') = \psi(x)$. In general, a spinor rotates through half the angle that the spacetime vectors rotates through. This is responsible for a topological distinction between SU(2) and SO(3). Increasing a rotation angle by 2π leads to $U \to -U$, $R \to R$. Since U and $-U$ both correspond to the rotation R, there is a two to one mapping of elements of SU(2) to elements of SO(3).

This is closely connected to the existence of two independent irreducible Reps. for the Dirac algebra (3.12). Indeed, if one restricts the angles of rotation in (B.25) and (B.17) to $[0, 2\pi)$, we still obtain the complete group of Lorentz transformation on spacetime vectors. To regain the complete group of spinor (SU2) transformations one can use a second basis of generators $\tau' = (-\tau_1, -\tau_2, -\tau_3)^{\mathrm{T}}$ in addition to the set of Pauli matrices defined in Eq. (B.25). Both generator basis are not not equivalent but fulfill both the Dirac algebra (3.12) and the SU(2) algebra (B.19) (modulus a factor 1/2).

4-component fermion representations

In the reducible Rep. (3.24) the generators $S_{\mu\nu}$ are given by

$$S_{01} = \mathbb{1}_2 \otimes -\frac{\tau_1}{2}\,, \quad S_{02} = \mathbb{1}_2 \otimes \frac{\tau_3}{2}\,, \quad S_{12} = \mathbb{1}_2 \otimes -\frac{\tau_2}{2}\,. \tag{B.27}$$

Consequently, the spinor transformation (B.22) takes the form of

$$U = \mathrm{e}^{-\frac{\mathrm{i}}{2}\epsilon_{\mu\nu}S_{\mu\nu}} = \mathrm{e}^{\frac{\mathrm{i}}{2}\mathbb{1}_2\otimes\epsilon\tau}\,. \tag{B.28}$$

with $\varepsilon = (\epsilon_{01}, \epsilon_{12}, -\epsilon_{02})^{\mathrm{T}}$ and $\tau = (\tau_1, \tau_2, \tau_3)^{\mathrm{T}}$. Using the matrix exponential we can rewrite

$$U = \begin{pmatrix} \mathrm{e}^{\frac{\mathrm{i}}{2}\epsilon\tau} & 0 \\ 0 & \mathrm{e}^{\frac{\mathrm{i}}{2}\epsilon\tau} \end{pmatrix}\,, \tag{B.29}$$

where the 2×2 blocks are again elements of SU(2). As for four-component spinors we have axial transformations similar to Eq. (3.28) for N_f flavors, we can apply these to obtain the full SU(2) symmetry, even with a restriction to the parameters $\epsilon \in [0, 2\pi)$.

Discrete symmetries

In Refs. [35, 36] explicit Reps. for discrete spacetime transformation on four-component fermion fields are discussed. Due to the four-component spinor space we have one degree of freedom each in the Rep. of parity inversion P_ξ and time reversal T_η. Parity inversion is defined as

$$(x_0, x_1, x_2)^{\mathrm{T}} \to (x_0, x_1, -x_2)^{\mathrm{T}}\,, \quad \psi(x) \to \frac{1}{2}\left[(1+\xi)\gamma_2\gamma_4 + \mathrm{i}(1-\xi)\gamma_2\gamma_5\right]\psi(x) \tag{B.30}$$

and time reversal is given by

$$(x_0, x_1, x_2)^{\mathrm{T}} \to (-x_0, x_1, x_2)^{\mathrm{T}}\,, \quad \psi(x) \to \frac{1}{2}\left[(1+\eta)\gamma_0\gamma_4 + \mathrm{i}(1-\eta)\gamma_0\gamma_5\right]\psi(x). \tag{B.31}$$

The complex phases ξ, η can be set to 1 for simplicity. The GN model is invariant under these discrete spacetime transformations.

C Naive lattice discretization of fermions in the Gross-Neveu model

In this section we discuss the naive discretization of fermion fields in one spatial dimension, i.e. $D = 1$, and the necessity of a non-diagonal modification term in the GN interaction term (4.4). The generalization to more than one dimension is rather straightforward. A more detailed discussion can be found in Refs. [16, 17, 42]. This chapter is mainly inspired by App. A in Ref. [16].

C.1 Free fermions

We define the Fourier transforms of the fermion fields in the x_1-direction as

$$\chi(n_0, x_1) = \frac{1}{\sqrt{N_s}} \sum_{k_1} \tilde{\chi}(n_0, k_1) \mathrm{e}^{\mathrm{i}k_1 x_1} \,, \quad \bar{\chi}(n_0, x_1) = \frac{1}{\sqrt{N_s}} \sum_{k_1} \tilde{\bar{\chi}}(n_0, k_1) \mathrm{e}^{\mathrm{i}k_1 x_1} \,. \tag{C.1}$$

Similar to the discussion in Sec. 4 the fermion fields are regularized by plane waves in the temporal direction and naively discretized in the spatial direction according to Eq. (4.1) and Eq. (4.3) for $D = 1$. The discrete momenta k_1 are chosen such that the boundary conditions in x_1 direction are periodic. They fulfill $-\pi \leq k_1 a \leq \pi$, i.e. they are in the first Brillouin zone. Inserting the Fourier transformation in the action (4.3) after setting $D = 1$ we obtain

$$S_{\text{free}}[\bar{\chi}, \chi] = \sum_{n_0=-N_t+1}^{N_t} \sum_{k_1} \tilde{\bar{\chi}}(n_0, k_1) \Big(\gamma_0(\mathrm{i}\omega_{n_0} + \mu) + \gamma_1 \mathrm{i} \sin(k_1 a)/a \Big) \tilde{\chi}(n_0, k_1) \ ,$$

where ω_{n_0} are frequencies defined in Eq. (4.1). In the continuum limit the sum over k_1 is restricted to values, where $|\sin(k_1 a) a| \ll 1$. These regions of these contributing momenta, denoted by $\mathcal{R}^{(m)}$ with $m = 0, 1$, are in the neighbor of the roots of $\sin(k_1 a)$, which we define as

$$k_1^{(m)} = \frac{\pi}{a} m \,, \quad m = 0, 1 \,. \tag{C.2}$$

Defining the fermion fields in these regions of contributing momenta as $\chi^{(m)}(n_0, k_1) = \tilde{\chi}(n_0, k_1 + k_1^{(m)})$ for $|k_1 a| \ll 1$ we can approximate the action, neglecting second order corrections in a, by

$$S_{\text{free}}[\tilde{\bar{\chi}}, \tilde{\chi}] = \sum_{n_0=-N_t+1}^{N_t} \sum_{m=0}^{1} \sum_{k_1 \in \mathcal{R}^{(m)}} \tilde{\bar{\chi}}(n_0, k_1) \Big(\gamma_0(\mathrm{i}\omega_{n_0} + \mu) + \gamma_1 \mathrm{i}(-1)^m k_1 \Big) \tilde{\chi}(n_0, k_1) \ . \tag{C.3}$$

This calculation is an example for the fermion doubling problem, as we obtain an additional fermion flavor for the naively discretized spatial direction. Generalized to D

naively discretized spacetime dimensions one would obtain 2^D fermion flavors instead of only one in the continuum theory. Another issue with the fermion doublers is that they do not follow the standard Dirac equation. We have an additional minus sign in front of the γ_1 matrix for $m \neq 0$. For free fermions this is not a problem, as these minus signs can be eliminated by the transformations of the field coordinates, i.e.

$$\tilde{\chi}^{(m)} = (\gamma_0)^m \tilde{\psi}^{(m)} \,, \quad \tilde{\bar{\chi}}^{(m)} = \tilde{\bar{\psi}}^{(m)} (\gamma_0)^m \tag{C.4}$$

with $m = 0, 1$.

C.2 Naive lattice discretization of the Gross-Neveu model

The action of the $1+1$-dimensional GN model for $N_f = 2$ in our hybrid approach is given by

$$S_\sigma[\bar{\chi}, \chi, \sigma] = S_{\text{free}}[\bar{\chi}, \chi] + \sum_{n_0=-N_t+1}^{N_t} \sum_{x_1} \bar{\chi}(n_0, x_1) \sigma(x_1) \chi(n_0, x_1) + \frac{N_f N_t}{\lambda} \sum_{x_1} \sigma^2(x_1) \,, \tag{C.5}$$

where we restricted the bosonic field σ to depend only on the spatial coordinate. In this chapter we will show that this discretization describes a continuum theory different from the GN model. Thus, we again express the action (C.5) in terms of Fourier transforms

$$\begin{aligned} S_\sigma[\tilde{\bar{\chi}}, \tilde{\chi}, \tilde{\sigma}] =& S_{\text{free}}[\tilde{\bar{\chi}}, \tilde{\chi}] + \sum_{n_0=-N_t+1}^{N_t} \sum_{k_1} \sum_{k_1'} \tilde{\bar{\chi}}(n_0, k_1) \tilde{\sigma}(k_1 - k_1') \tilde{\chi}(n_0, k_1') \\ &+ \frac{N_f N_t}{\lambda} \sum_{k_1} |\tilde{\sigma}(k_1)|^2 \,, \end{aligned} \tag{C.6}$$

where we used Eq. (C.1) and the Fourier transform of the bosonic field, defined by

$$\sigma(x_1) = \frac{1}{\sqrt{N_s}} \sum_{k_1} \tilde{\sigma}(k_1) \mathrm{e}^{\mathrm{i} k_1 x_1} \tag{C.7}$$

As in Sec. C.1 only fermionic momenta in the regions $\mathcal{R}^{(m)}$ contribute in the continuum limit. However, there is no such suppression for the σ modes. Consequently, we rewrite the interaction term in Eq. (C.6)

$$\sum_{n_0=-N_t+1}^{N_t} \sum_{k_1, k_1'} \sum_{m, m'} \tilde{\bar{\chi}}^{(m)}(n_0, k_1) \tilde{\sigma}^{(mm')}(k_1 - k_1') \tilde{\chi}^{(m')}(n_0, k_1') \tag{C.8}$$

with the definition

$$\tilde{\sigma}^{(mm')}(k_1) = \tilde{\sigma}(k_1 + k_1^{(m)} - k_1^{(m')}) \,. \tag{C.9}$$

Note that the field coordinates $\tilde{\chi}^{(m)}$ do not obey the standard kinetic term for fermion fields and can be related to the usual fermionic field coordinates by Eq. (C.4). We express the interaction term (C.8) in terms of $\tilde{\psi}^{(m)}$

$$\sum_{n_0=-N_t+1}^{N_t} \sum_{k_1,k_1'} \sum_{m,m'} \bar{\tilde{\psi}}^{(m)}(n_0,k_1)(\gamma_0)^m \tilde{\sigma}^{(mm')}(k_1-k_1')(\gamma_0)^{m'} \tilde{\psi}^{(m')}(n_0,k_1') \,. \tag{C.10}$$

The terms with $m = m'$ describe the interaction of the GN model. However, we obtain two additional terms, i.e.

$$\begin{aligned}\sum_{n_0=-N_t+1}^{N_t} \sum_{k_1,k_1'} \Big[&\bar{\tilde{\chi}}^{(0)}(n_0,k_1)\tilde{\sigma}^{(01)}(k_1-k_1')\gamma_0\tilde{\chi}^{(1)}(n_0,k_1') \\ &+\bar{\tilde{\chi}}^{(1)}(n_0,k_1)\gamma_0\tilde{\sigma}^{(10)}(k_1-k_1')\tilde{\chi}^{(0)}(n_0,k_1')\Big] \,.\end{aligned} \tag{C.11}$$

These terms are non-scalar in spin space and we obtain an interaction between different fermion doublers. Hence, they are not part of the GN model.

To derive a correct naive lattice discretization of the GN model, it is important to note that the correct interaction terms are proportional to $\tilde{\sigma}^{(mm)}$. As only fermion modes in the regions $\mathcal{R}^{(m)}$ contribute and the additional, non-scalar interaction terms are proportional to

$$\tilde{\sigma}^{(10)}(k_1-k_1') = \tilde{\sigma}^{(01)}(k_1-k_1') = \tilde{\sigma}(k_1-k_1'+\pi/a) \,, \tag{C.12}$$

one can eliminate the terms (C.11) by replacing $\tilde{\sigma}(k_1-k_1')$ with $\tilde{W}_1(k_1-k_1')\tilde{\sigma}(k_1-k_1')$ in Eq. (C.6). In principle, one could choose any weight-function $\tilde{W}_1$, which fulfills $\tilde{W}_1(k_1-k_1') \to 1$ for $k_1-k_1' \approx k_1^{(0)} = 0$ and $\tilde{W}_1(k_1-k_1') \to 0$ for $k_1-k_1' \approx k_1^{(1)} = \pi/a$.

In our work we apply two choices for $\tilde{W}_1(k_1-k_1')$, i.e. a soft momentum cutoff

$$\tilde{W}_1'(k_1-k_1') = \left[1+\cos(k_1a-k_1'a)\right]/2 \tag{C.13}$$

and a hard momentum cutoff

$$\tilde{W}_1''(k_1-k_1') = \Theta\left(\frac{\pi}{2a} - |k_1-k_1'|\right) \,, \tag{C.14}$$

where $\Theta(x)$ is the Heaviside function defined as

$$\Theta(x) = \begin{cases} 0 & x<0 \\ 1/2 & x=0 \\ 1 & x>0 \end{cases} \,. \tag{C.15}$$

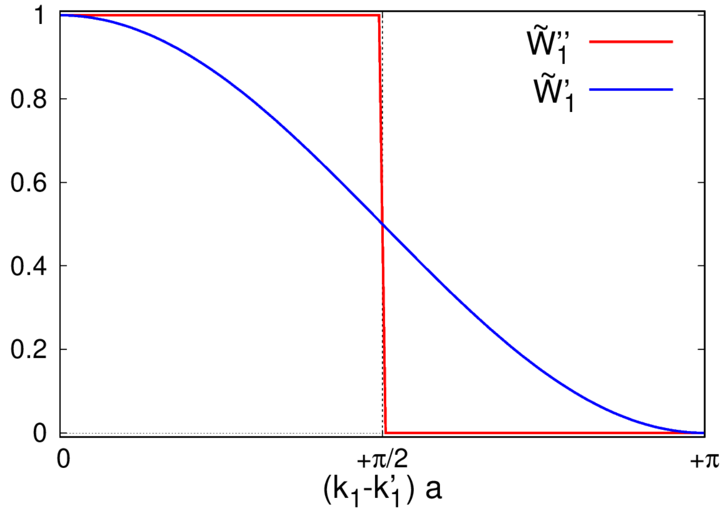

Fig. C.1: The proposed weight functions $\tilde{W}_1'$ and $\tilde{W}_1''$ as functions of the bosonic momentum $k_1 - k_1'$.

Both functions are plotted in Fig. C.1 for $(k_1 - k_1') > 0$, since both functions are symmetric around the origin. Besides one could choose any weight-function, that fulfills the properties describes above, $\tilde{W}_1'$ and $\tilde{W}_1''$ are extreme choices in terms of how to suppress high bosonic momenta. While both yield the correct continuum result, $\tilde{W}_1'(k_1 - k_1')$ suppresses the wrong interactions at $k_1 - k_1' = \pi/a$ relatively crudely at finite a. In contrast, $\tilde{W}_1''(k_1 - k_1')$ vanishes completely near $k_1 - k_1' = \pi/a$.

The modified action in spacetime coordinates is given by

$$
\begin{aligned}
S_\sigma[\bar{\chi}, \chi, \sigma] =& \Bigg(S_{\text{free}}[\bar{\chi}, \chi] + \sum_{n_0=-N_t+1}^{N_t} \sum_{x_1, y_1} \bar{\chi}(n_0, x_1) W_1(x_1 - y_1) \sigma(y_1) \chi(n_0, x_1) \Bigg) \\
&+ \frac{N_f N_t}{\lambda} \sum_{x_1} \sigma^2(x_1) \,,
\end{aligned}
\tag{C.16}
$$

where W_1 is the inverse Fourier transform of $\tilde{W}_1$. For $\tilde{W}_1'$ and $\tilde{W}_1''$ the inverse Fourier transforms are given by Eq. (4.12) and Eq. (4.13), respectively. These calculations can rather straightforward be generalized to D dimensions by consideration of

$$
\tilde{W}_D(\mathbf{k} - \mathbf{k'}) = \prod_{j=1}^{D} \tilde{W}_1(k_j - k_j')
\tag{C.17}
$$

before Fourier transforming the interaction, as has been done in Eq. (4.5) and Eq. (4.6) for W_D' and W_D''. In Ref. [16, 17] a similar procedure has been performed in 1 + 1 dimensions, where also the temporal direction has been treated with a lattice discretization.

As we have explicitly discussed, the choice $W_1(x_1-y_1) = \delta(x_1-y_1)$ does not describe the GN model, but has additional non-scalar interaction terms (e.g. Eq. (C.11)). However, in the limit $N_f \to \infty$ we obtain qualitatively similar results to W_1'' for the $1+1$- and $2+1$-dimensional GN model. In the continuum limit $W_1(x_1-y_1) = \delta(x_1-y_1)$ seems to give the same phase diagram as W_1' and W_1''. This unexpected behavior is subject of current investigation.

Bibliography

[1] D. H. Rischke. "The Quark gluon plasma in equilibrium". In: *Prog. Part. Nucl. Phys.* 52 (2004), pp. 197–296. DOI: `10.1016/j.ppnp.2003.09.002`. arXiv: `nucl-th/0305030`.

[2] M. G. Alford, A. Schmitt, K. Rajagopal, and T. Schäfer. "Color superconductivity in dense quark matter". In: *Rev. Mod. Phys.* 80 (2008), pp. 1455–1515. DOI: `10.1103/RevModPhys.80.1455`. arXiv: `0709.4635 [hep-ph]`.

[3] H. Suganuma, T. M. Doi, K. Redlich, and C. Sasaki. "Relating Quark Confinement and Chiral Symmetry Breaking in QCD". In: *J. Phys. G* 44 (2017), p. 124001. DOI: `10.1088/1361-6471/aa8e2f`. arXiv: `1709.05981 [hep-lat]`.

[4] P. Petreczky. "Lattice QCD at non-zero temperature". In: *J. Phys. G* 39 (2012), p. 093002. DOI: `10.1088/0954-3899/39/9/093002`. arXiv: `1203.5320 [hep-lat]`.

[5] P. de Forcrand. "Simulating QCD at finite density". In: *PoS* LAT2009 (2009). Ed. by C. Liu and Y. Zhu, p. 010. DOI: `10.22323/1.091.0010`. arXiv: `1005.0539 [hep-lat]`.

[6] Y. Nambu and G. Jona-Lasinio. "Dynamical Model of Elementary Particles Based on an Analogy with Superconductivity. 1." In: *Phys. Rev.* 122 (1961). Ed. by T. Eguchi, pp. 345–358. DOI: `10.1103/PhysRev.122.345`.

[7] D. J. Gross and A. Neveu. "Dynamical Symmetry Breaking in Asymptotically Free Field Theories". In: *Phys. Rev. D* 10 (1974), p. 3235. DOI: `10.1103/PhysRevD.10.3235`.

[8] M. Buballa and S. Carignano. "Inhomogeneous chiral condensates". In: *Prog. Part. Nucl. Phys.* 81 (2015), pp. 39–96. DOI: `10.1016/j.ppnp.2014.11.001`. arXiv: `1406.1367 [hep-ph]`.

[9] M. Thies and K. Urlichs. "Revised phase diagram of the Gross-Neveu model". In: *Phys. Rev. D* 67 (2003), p. 125015. DOI: `10.1103/PhysRevD.67.125015`. arXiv: `hep-th/0302092`.

[10] E. Nakano and T. Tatsumi. "Chiral symmetry and density wave in quark matter". In: *Phys. Rev. D* 71 (2005), p. 114006. DOI: `10.1103/PhysRevD.71.114006`. arXiv: `hep-ph/0411350`.

[11] G. Basar, G. V. Dunne, and M. Thies. “Inhomogeneous Condensates in the Thermodynamics of the Chiral NJL(2) model”. In: *Phys. Rev. D* 79 (2009), p. 105012. DOI: `10.1103/PhysRevD.79.105012`. arXiv: `0903.1868 [hep-th]`.

[12] M. Thies. “Phase structure of the (1+1)-dimensional Nambu–Jona-Lasinio model with isospin”. In: *Phys. Rev. D* 101.1 (2020), p. 014010. DOI: `10.1103/PhysRevD.101.014010`. arXiv: `1911.11439 [hep-th]`.

[13] M. Thies. “First-order phase boundaries of the massive (1+1)-dimensional Nambu–Jona-Lasinio model with isospin”. In: *Phys. Rev. D* 101.7 (2020), p. 074013. DOI: `10.1103/PhysRevD.101.074013`. arXiv: `2002.01190 [hep-th]`.

[14] D. Nickel. “Inhomogeneous phases in the Nambu-Jona-Lasino and quark-meson model”. In: *Phys. Rev. D* 80 (2009), p. 074025. DOI: `10.1103/PhysRevD.80.074025`. arXiv: `0906.5295 [hep-ph]`.

[15] S. Carignano, M. Buballa, and B.-J. Schaefer. “Inhomogeneous phases in the quark-meson model with vacuum fluctuations”. In: *Phys. Rev. D* 90.1 (2014), p. 014033. DOI: `10.1103/PhysRevD.90.014033`. arXiv: `1404.0057 [hep-ph]`.

[16] J. Lenz, L. Pannullo, M. Wagner, B. Wellegehausen, and A. Wipf. “Inhomogeneous phases in the Gross-Neveu model in 1+1 dimensions at finite number of flavors”. In: *Phys. Rev. D* 101.9 (2020), p. 094512. DOI: `10.1103/PhysRevD.101.094512`. arXiv: `2004.00295 [hep-lat]`.

[17] L. Pannullo. “Inhomogeneous Phases in the 1+1-Dimensional Gross-Neveu Model at Finite Number of Fermion Flavors”. MA thesis. Goethe University Frankfurt am Main, May 2020.

[18] B. Rosenstein, B. J. Warr, and S. H. Park. “The Four Fermi Theory Is Renormalizable in (2+1)-Dimensions”. In: *Phys. Rev. Lett.* 62 (1989), pp. 1433–1436. DOI: `10.1103/PhysRevLett.62.1433`.

[19] J. Bjorken. “Highly Relativistic Nucleus-Nucleus Collisions: The Central Rapidity Region”. In: *Phys. Rev. D* 27 (1983), pp. 140–151. DOI: `10.1103/PhysRevD.27.140`.

[20] I. Bearden et al. “Pseudorapidity distributions of charged particles from Au+Au collisions at the maximum RHIC energy”. In: *Phys. Rev. Lett.* 88 (2002), p. 202301. DOI: `10.1103/PhysRevLett.88.202301`. arXiv: `nucl-ex/0112001`.

[21] B. Alver et al. “Phobos results on charged particle multiplicity and pseudorapidity distributions in Au+Au, Cu+Cu, d+Au, and p+p collisions at ultra-relativistic energies”. In: *Phys. Rev. C* 83 (2011), p. 024913. DOI: `10.1103/PhysRevC.83.024913`. arXiv: `1011.1940 [nucl-ex]`.

[22] K. Okamoto, Y. Akamatsu, and C. Nonaka. “A new relativistic hydrodynamics code for high-energy heavy-ion collisions”. In: *Eur. Phys. J. C* 76.10 (2016), p. 579. DOI: `10.1140/epjc/s10052-016-4433-x`. arXiv: `1607.03630 [nucl-th]`.

[23] B. Friman et al., eds. *The CBM physics book: Compressed baryonic matter in laboratory experiments*. Vol. 814. 2011. DOI: `10.1007/978-3-642-13293-3`.

[24] T. Ohsaku. “Relativistic model for two-band superconductivity”. In: (June 2003). arXiv: `cond-mat/0306472`.

[25] R. MacKenzie, P. Panigrahi, and S. Sakhi. “Superconductivity in a planar field theory through the Kosterlitz-Thouless mechanism”. In: *Physical review. B, Condensed matter* 48 (Sept. 1993), pp. 3892–3895. DOI: `10.1103/PhysRevB.48.3892`.

[26] A. Kalinkin and V. Skorikov. “Phase transitions in four fermion models”. In: *Inorg. Mater.* 39 (2003), pp. 765–779. DOI: `10.1023/A:1025063207931`.

[27] M. Winstel, J. Stoll, and M. Wagner. “Lattice investigation of an inhomogeneous phase of the 2+1-dimensional Gross-Neveu model in the limit of infinitely many flavors”. In: (Aug. 2019). arXiv: `1909.00064 [hep-lat]`.

[28] R. Narayanan. “Phase diagram of the large N Gross-Neveu model in a finite periodic box”. In: *Phys. Rev. D* 101.9 (2020), p. 096001. DOI: `10.1103/PhysRevD.101.096001`. arXiv: `2001.09200 [hep-th]`.

[29] M. Buballa, L. Kurth, M. Wagner, and M. Winstel. In preparation. 2020.

[30] A. Wipf. *Statistical approach to quantum field theory: An introduction*. Vol. 864. 2013. DOI: `10.1007/978-3-642-33105-3`.

[31] J. Kapusta and C. Gale. *Finite-temperature field theory: Principles and applications*. Cambridge Monographs on Mathematical Physics. Cambridge University Press, 2011. ISBN: 978-0-521-17322-3, 978-0-521-82082-0, 978-0-511-22280-1. DOI: `10.1017/CBO9780511535130`.

[32] J. Hubbard. “Calculation of partition functions”. In: *Phys. Rev. Lett.* 3 (1959), pp. 77–80. DOI: `10.1103/PhysRevLett.3.77`.

[33] C. Rakotonirina. “Expression of a tensor commutation matrix in terms of the generalized Gell-Mann matrices”. In: *Int. J. Math. Math. Sci.* 2007 (2007), p. 20672. arXiv: `math/0511451`.

[34] T. W. Appelquist, M. J. Bowick, D. Karabali, and L. Wijewardhana. “Spontaneous Chiral Symmetry Breaking in Three-Dimensional QED”. In: *Phys. Rev. D* 33 (1986), p. 3704. DOI: `10.1103/PhysRevD.33.3704`.

[35] H. Gies and L. Janssen. “UV fixed-point structure of the three-dimensional Thirring model”. In: *Phys. Rev. D* 82 (2010), p. 085018. DOI: `10.1103/PhysRevD.82.085018`. arXiv: `1006.3747 [hep-th]`.

[36] D. D. Scherer and H. Gies. “Renormalization Group Study of Magnetic Catalysis in the 3d Gross-Neveu Model”. In: *Phys. Rev. B* 85 (2012), p. 195417. DOI: `10.1103/PhysRevB.85.195417`. arXiv: `1201.3746 [cond-mat.str-el]`.

[37] K. Urlichs. “Baryons and baryonic matter in four-fermion interaction models”. PhD thesis. University of Erlangen-Nuernberg, Feb. 2007.

[38] H. Rothe. *Lattice gauge theories: An Introduction.* Vol. 43. 1992.

[39] M. Wagner. “Fermions in the pseudoparticle approach”. In: *Phys. Rev. D* 76 (2007), p. 076002. DOI: `10.1103/PhysRevD.76.076002`. arXiv: `0704.3023 [hep-lat]`.

[40] A. Heinz, F. Giacosa, M. Wagner, and D. H. Rischke. “Inhomogeneous condensation in effective models for QCD using the finite-mode approach”. In: *Phys. Rev. D* 93.1 (2016), p. 014007. DOI: `10.1103/PhysRevD.93.014007`. arXiv: `1508.06057 [hep-ph]`.

[41] J. J. Lenz, L. Pannullo, M. Wagner, B. Wellegehausen, and A. Wipf. “Baryons in the Gross-Neveu model in 1+1 dimensions at finite number of flavors”. In: (July 2020). arXiv: `2007.08382 [hep-lat]`.

[42] Y. Cohen, S. Elitzur, and E. Rabinovici. “A Monte Carlo Study of the Gross-Neveu Model”. In: *Nucl. Phys. B* 220 (1983), pp. 102–118. DOI: `10.1016/0550-3213(83)90136-0`.

[43] M. C. Galassi et al. *GNU Scientific Library.* Network Theory, Ltd., Aug. 2019.

[44] O. Schnetz, M. Thies, and K. Urlichs. “Phase diagram of the Gross-Neveu model: Exact results and condensed matter precursors”. In: *Annals Phys.* 314 (2004), pp. 425–447. DOI: `10.1016/j.aop.2004.06.009`. arXiv: `hep-th/0402014`.

[45] K. Klimenko. “Phase Structure of Generalized Gross-Neveu Models”. In: *Z. Phys. C* 37 (1988), p. 457. DOI: `10.1007/BF01578141`.

[46] B. Rosenstein, B. Warr, and S. Park. “Thermodynamics of (2+1)-dimensional Four Fermi Models”. In: *Phys. Rev. D* 39 (1989), p. 3088. DOI: `10.1103/PhysRevD.39.3088`.

[47] U. Wolff. “The Phase Diagram of the Infinite N Gross-Neveu Model at Finite Temperature and Chemical Potential”. In: *Phys. Lett. B* 157 (1985), pp. 303–308. DOI: `10.1016/0370-2693(85)90671-9`.

[48] P. de Forcrand and U. Wenger. “New baryon matter in the lattice Gross-Neveu model”. In: *PoS* LAT2006 (2006). Ed. by T. Blum et al., p. 152. DOI: `10.22323/1.032.0152`. arXiv: `hep-lat/0610117`.

[49] S. Carignano and M. Buballa. “Inhomogeneous chiral condensates in three-flavor quark matter”. In: *Phys. Rev. D* 101.1 (2020), p. 014026. DOI: `10.1103/PhysRevD.101.014026`. arXiv: `1910.03604 [hep-ph]`.

[50] C. Wetterich. "Spinors in euclidean field theory, complex structures and discrete symmetries". In: *Nucl. Phys. B* 852 (2011), pp. 174–234. DOI: `10.1016/j.nuclphysb.2011.06.013`. arXiv: `1002.3556 [hep-th]`.

[51] L. Ryder. *Quantum Field Theory.* Cambridge University Press, June 1996.

Acknowledgements

In this last chapter I want to express my gratitude to the people that supported me with my thesis and my studies.

First and foremost, I want to thank Marc Wagner for his excellent supervision and innumerable helpful discussions. His dedication to the supervision of young scientists is a role model for many other group leaders and this work would not have been possible without his steady support. Especially, I am grateful for the opportunity to attend the FAIRness conference in Arenzano, Genova.

Next, I want to thank Laurin Pannullo not only for his useful advice on this thesis but also for many fruitful discussions.

My thanks go to my family for their continuous support during my studies and my life. Finally, I would also like to thank Pascal and Lisa for their ability to distract and motivate me whenever I need it.